Partial Joint Penetration Welds in Aluminum Structures

by

Laurent Gérin

A thesis
presented to the University of Waterloo
in fulfillment of the
thesis requirement for the degree of
Master of Applied Science
in
Civil Engineering

Waterloo, Ontario, Canada, 2020

Author's Declaration

I hereby declare that I am the sole author of this thesis. This is a true copy of the thesis, including any required final revisions, as accepted by my examiners.

I understand that my thesis may be made electronically available to the public.

Abstract

Aluminum structures are becoming more and more common in Canada and the world as engineers and decision-makers become more aware of the possibility to lower life cycle costs. Aluminum's corrosion resistance, light weight and high strength make it especially advantageous for use in pedestrian bridges and other truss-type structures. However, Canadian design codes for the use of aluminum in structures lack guidance and impose restrictions on partial joint penetration (PJP) groove welds; these welds can be very useful in the design of tubular truss-type structures. Engineers are finding that this is causing challenges in the design of competitive structures, given that some international design standards have less restrictions and provide more guidance.

This thesis reports on a research project to evaluate the performance of PJP groove welds and to develop models for their use in both strength and fatigue design. These welds have been used commonly in steel structures where the full resistance of a complete joint penetration weld is not required, but essentially no literature exists on their use in aluminum. A comprehensive experimental program of almost 100 samples was undertaken, testing partial joint penetration groove butt welds. The performance of the welds was evaluated both in static (strength) and cyclic (fatigue) loading. The experimental data was also used to calibrate both strength and fatigue models, using advanced measuring technologies such as digital image correlation, which allowed for the observation of highly localized effects in small samples.

Overall, it was found that current code penalties on PJP welds may not be justified. A strengthening mechanism was identified where lateral restraint is provided by the unwelded part of the joint and raises the effective strength. This comes at the expense of some ductility. Design of the welds was found to be relatively straightforward, with the strength depending practically only on the strength of the heat-affected zone. It is significantly weaker than the initial base metal strength for alloys typically used in structural applications. A major issue was however identified in the effective throat provided in the welds. All samples, sourced from three different fabricators, had effective weld throats much smaller than specified, causing a major concern for the safety of these welds. Further research is required to ensure that the minimum dimensional parameters required by the welding codes such as the groove opening angle are adequate. Rigorous testing and qualification procedures may be required to mitigate negative impacts of the less-than-expected effective throat until more research is conducted.

In fatigue loading conditions, the PJP welds had a relatively short life. After a statistical analysis of the test data, it was shown that the PJP welds would likely be considered to be

in the weakest or second-weakest fatigue detail categories in the North American design codes. In Europe, design specifications specifically provide details for PJP welds loaded in fatigue; these specifications were found to correspond well with the test data. A fracture-mechanics based model was developed to predict the performance of the welds for a broad range of dimensional parameters. It was found that over a wide range of PJP weld sizes (20-80% of the weld thickness), the fatigue performance did not vary significantly with the degree of penetration when the stress range was defined over the net cross section of the weld. This greatly simplifies design for engineers, as a single design stress-life curve may be used to conservatively and accurately assess the design life of a component instead of using more complex models. The model also showed that eccentricities from effects such as warping during welding significantly affect fatigue performance by precipitating crack growth to one side of the plate. It was also found that welding defects generally had little influence on the performance of the welds, due to the extreme notching effect from the lack of penetration inherent to a PJP weld.

Lastly, the research program was extended to include flare-bevel groove welds, a specific type of PJP weld, which is most often seen in tubular connections. However, due to the COVID-19 pandemic and related laboratory shutdowns, the testing program was delayed at the time of writing this thesis. Preliminary results indicate similitude in behaviour between PJP butt welds and flare-bevel groove welds.

Acknowledgements

First and foremost, I want to thank my supervisor, Dr. Scott Walbridge. The many great discussions we had, his advice and new perspectives, and his insistence on practicality were an integral part of my graduate studies and will serve me throughout my career. Dr. Walbridge showed me not only new ideas but also new places, with a visit to New Brunswick, conferences in Halifax and Tokyo and a research exchange in Switzerland. I remember a conversation where Dr. Walbridge mentioned he wanted to be the "Cadillac of supervisors" – I believe I got the Rolls Royce!

I also want to thank Dr. Susan Guravich of Skarborn Engineering, the primary industry partner for this research project and coordinator with external fabricators. Her profound knowledge of all things welding was critical in creating an experimental program that was both comprehensive and accessible, as well as in the interpretation of the results.

Financial support from the Natural Sciences and Engineering Research Council of Canada (NSERC) is graciously acknowledged. This project was also made possible by generous material donations from Bourque Industrial, Design Built Mechanical Inc, L&A Metalworks, McSheffery Industries and Skarborn Engineering.

To Dr. Alain Nussbaumer and Dr. Matthew Sjaarda for their warm welcome to the EPFL: *Merci!* My discussions with Dr. Nussbaumer pushed me to discover more about fracture mechanics and gain a deeper understanding of the models behind it. My gratitude extends to the entire group at the RESSLab who generously let me use their facilities and made me feel at home.

I want to thank Dr. Luqman Shah, without whom the preparation for macro-etching and micro-hardness testing of the weld samples would not have been possible. As well, Jonathan Hellinga, who in less than a month, learned to program and implemented the algorithm used in this thesis to find the effective throat of welds.

The experimental program could not have been possible without the University of Waterloo's Structures Laboratory technicians, Doug Hirst, Richard Morrison and Peter Volcic. I especially want to thank Richard, who was always there to help, whether for the Steel Bridge Team or helping turn an old water heater into a sauna stove.

I am also grateful to my colleagues at ClearCalcs for their patience and flexibility as I wrote this thesis and through my studies.

Finally, I want to thank all my friends and my family. All your love, support and encouragement from the start kept me going through this adventure, through the best and the worst. And Elisabeta Cojocaru, whose patience, affection and wonderful piano kept me sane through the entire thesis-writing.

Table of Contents

List of Tables

List of Figures

Chapter 1

Introduction

Aluminum (or outside North America: *Aluminium*), is the most common metal on Earth. It offers high strength, is extremely light weight, provides extraordinary corrosion resistance, and can be shaped in essentially any form. These benefits have led to its widespread adoption in the automotive and particularly in the aerospace industries. However, aluminum has seldom been used in the construction industry, mostly because of higher upfront costs and low familiarity with the material as opposed to traditional building materials. Recently, greater consideration into the total life cycle cost of structures has made aluminum a more attractive choice to decision-makers throughout Canada. Applications of aluminum in bridges and structures in remote locations and industrial environments are becoming increasingly common, as shown in Figure 1.1.

Canadian designers of aluminum structures are however encountering a challenge in the economical design of some structures because of restrictions and lack of guidance in the Canadian design codes on the use of partial joint penetration (PJP) groove welds. These welds, defined at their simplest as *"welds having joint penetration less than complete"*, could have great utility in aluminum truss-type structures. In their most basic form, these welds typically consist of two plates welded together from both sides, but without the weld fully penetrating the thickness of the plates (two leftmost images in Figure 1.2). These are often used in steel structures to connect columns and other structural members, which

Figure 1.1: Various aluminum structures. Clockwise, starting from top left (*Image source in parentheses*): Shanghai Science & Technology Museum *(CallisonRTKL)*, Arvida Bridge in Saguenay, QC *(Répertoire du Patrimoine du Québec)*, Remote trail modular bridge (*Great Northern Docks*), Pedestrian Footbridge in Kativik, QC (*MAADI Group*).

do not require their welds to carry significant loads. The definition also extends to more weld geometries, such as T-joints and flare-bevel groove welds (two rightmost images in Figure 1.2). In particular, flare-bevel groove welds may be useful in truss structures such as industrial walkways, loading ramps, and pedestrian bridges, where the rounded corners of one tube can be used as a groove to weld a connecting tube.

During discussions with industry experts, it was mentioned that uncertainty in the reliability of welds and in their fatigue performance were factors discouraging the use of PJP

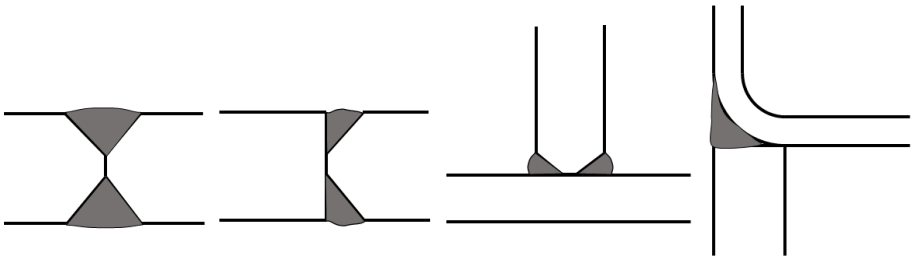

Figure 1.2: Different types of PJP weld connections. From left to right, a double-bevel PJP butt groove weld, a single-bevel PJP butt groove weld, a T-type PJP groove weld, and a flare-bevel groove weld.

welds. A summary review of international design codes revealed that other jurisdictions have less restrictions and offer more guidance to their designers. As a result, Canadian engineers are finding that their designs may be uncompetitive on the international markets. Against this background, a research project was established to evaluate the performance of PJP groove welds and provide further guidance to aluminum designers.

1.1 Objectives

The objective of this research project was to establish a baseline of knowledge on the performance of partial joint penetration welds in aluminum. Specifically:

1. Predicting the strength of PJP welds and the appropriateness of their use in aluminum structures;
2. Establishing a simple design curve for PJP welds in aluminum structures for fatigue loading, making use of experimental test data and a validated fracture mechanics-based model.

1.2 Scope

The scope of the research project was limited to analyzing, small-scale testing, and modeling of plates joined by a PJP groove butt weld. The performance both in static (strength) and cyclic (fatigue) loading was tested. The global behaviour of these welds in a structural system was not considered, nor was their implementation in the framework of weld qualification, inspection and testing.

Flare bevel welds in tubular structures, such as pedestrian footbridges, were originally intended to be included in this thesis as well. However, due to the 2019 COVID-19 pandemic, this segment of the research program was halted at the time of writing. A brief summary of progress to date on these is included in the penultimate chapter of this thesis.

1.3 Thesis Organization

This thesis is separated into eight chapters (including this introduction), which may be briefly summarized as follows:

- Chapter 2: A thorough review of the current literature. The use of aluminum in structures and its properties that differ from typical structural materials is reviewed, with a focus on welding and international design standards. Fatigue in structures and current approaches are then presented as a primer to a significant component of this research project. Finally, the current state of knowledge on PJP welds both in steel and aluminum is presented, touching on design standards and specific considerations for fatigue raised in literature.

- Chapter 3: Overview of the comprehensive experimental program developed for this study. The samples used in the program are specified, along with the nomenclature used throughout this thesis. The advanced methods used to characterize samples and to take measurements during tests, such as micro-hardness mapping and digital image correlation, are explained.

- Chapter 4: Description of a linear-elastic fracture mechanics model used as a basis for fatigue life prediction of PJP welds. The notion of a critical weld size for fracture and fatigue is introduced and its effects on modelling PJP welds is discussed.

- Chapter 5: Explanation of the 2D finite element model used in the prediction of strength and fatigue performance. The analysis parameters are listed and convergence studies on the desired analysis results are presented, both for static and fatigue models.

- Chapter 6: Results of the experimental program are discussed and compared to international design codes and the models generated for this study.

- Chapter 7: A brief discussion of an ongoing extension of this research project to flare-bevel welds, often used to connect tubes with rounded corners. This chapter is comprised of a short review of literature on flare bevel welds, followed by a description of the experimental program undertaken for the study, and is concluded by a discussion of preliminary results.

- Chapter 8: A brief review of the research program, followed by major findings of the study and recommendations for future work to be performed.

Chapter 2

Literature Review

A comprehensive literature review was undertaken on the state of the art for the use of partial joint penetration welds in aluminum structures.

2.1 Aluminum and its Use in Structures

Aluminum is the third most abundant element on Earth, and the most commonly found metal. Despite its abundance, aluminum was only discovered in 1827 with the advent of the Scientific Revolution. It was almost another 60 years before the Hall-Héroult process was designed and allowed industrial production of aluminum [1]. Since then, the metal has seen its most widespread use in the transportation industry, being used in cars, trains, airplanes and ships, but is also extensively used in a variety of applications, from beverage cans to window frames.

Although aluminum in its pure state offers some desirable qualities, most aluminum is alloyed with other elements, usually magnesium, manganese, zinc, copper or silicon. These alloying elements provide significant increases in strength, while affecting other properties such as corrosion resistance, ductility, weldability and more. There are thus many different alloys of aluminum, which combine certain proportions of the previously mentioned

elements to achieve desired material properties. Additionally, some aluminum alloys react positively to heat treatment, sometimes more than doubling in strength after tempering, at the expense of ductility. Other alloys are subject to significant work hardening, which also increases the strength. Both heat-treatable and work-hardenable alloys are very sensitive to high temperatures, which brings special considerations when welding aluminum, as discussed later.

In all cases, all aluminum alloys and tempers generally exhibit these common properties:

- **Density**: Aluminum has a density of $2700\,\mathrm{kg/m^3}$. This is extremely low for a metal. As an example, this is a third the density of steel ($8050\,\mathrm{kg/m^3}$).
- **Strength**: Common structural aluminum alloys used in structures have relatively high strength. The 6061-T6 alloy, perhaps the most common in structures, has a minimum ultimate strength of 290 MPa, and some alloys can reach an ultimate strength upwards of 550 MPa. While structural alloys such as 6061-T6 are weaker than most structural steels, when their strength is considered with its low density, aluminum alloys have a strength-to-weight ratio rivaled only by the strongest steels.
- **Elasticity**: Similarly to density, aluminum has an elasticity of approximately a third of steel, at 70 GPa vs. 200 GPa for steel. This has consequences in the design of aluminum structures, where the lower rigidity means increased deflections and susceptibility to buckling.
- **Corrosion resistance**: In most aluminum alloys, as soon as surfaces are exposed to the air, a thin but extremely strong oxide layer is formed. This layer is stable under most typical environments and prevents corrosion, which means that structures will not "rust out".
- **Extrudability**: Aluminum can be extruded into essentially any shape, allowing optimized usage for unique applications, such as window frames or bridge decks. Examples of extrusions are shown in Figure 2.1.

- **Cost**: At the time of writing, the price of aluminum per tonne was approximately three times the cost of steel. This is somewhat offset by aluminum's low density and higher strength-to-weight ratio, which means that aluminum structures will be roughly half of the weight of steel structures [2]. Other significant cost reductions are found in shipping and handling at construction, and reduced maintenance requirements and scrap value over the life cycle.

- **Sustainability**: Aluminum requires tremendous energy use in its reduction from a mineral form. However, it can be recycled an infinite amount of times with over 90% savings in energy per kilogram. Additional sustainability benefits are found by lower weight in vehicles and reduced maintenance requirements [3].

Figure 2.1: Various customized shapes can be achieved with the use of extrusions. *Image from Lynch Metals*

Aluminum has traditionally not seen much use in structural applications, generally limited by higher costs and sparse design experience. This is compounded by traditional cost assessments separating initial capital investments and further maintenance costs, instead of considering total cost over the entire life cycle of the structure [4]. However, improvements in technology and a shift towards considering total lifespan cost instead of initial

cost have led to growing adoption among specific sectors of the construction industry. Notably, curtain-wall systems almost exclusively make use of aluminum for its extrudability and corrosion resistance, which allows using complex shapes to optimize the performance of the wall, and avoiding issues with rust and staining. In industrial environments where corrosion is a major concern, aluminum's inherent resistance to corrosion often makes it the most economical choice. Another sector where aluminum has seen use is in pedestrian bridges and walkways. The combination of its light weight and corrosion resistance allow rapid construction in hard to access locations and minimal maintenance costs. A study prepared by Deloitte in 2012 [5] found that over a 50 year lifespan, aluminum was consistently more economical than steel in the construction of pedestrian bridges.

2.1.1 Welding Aluminum

Most aluminum alloys can readily be welded, with a few exceptions in exceptionally high strength alloys. There is however a caveat. As previously discussed, aluminum alloys can be rendered significantly stronger by heat treatment processes or by work hardening. However, welding exposes the metal to extremely high temperatures which tend to effectively cancel the benefits of heat treatment near the weld, in what is called the *heat affected zone* (HAZ) [6]. As such, large reductions of the base metal strength (up to 50%, in some cases) in the HAZ must be considered and welded connections are thus often a weak point in aluminum constructions. This differs significantly from welds in structural steel, where welding is assumed not to affect the base material and joints can easily be designed to be stronger than their connected members. Malin [6] found that this weakening occurs because of the temperature gradient during the welding process. The heat gradient causes alloying elements to precipitate or dissolve at certain distances from the weld, which causes some localized weakening of the aluminum.

Recently, some new techniques such as friction stir welding (FSW) have been employed which use considerably less heat and thus mitigate the loss of strength in the HAZ. Friction stir welding is increasingly used in the automotive, shipbuilding and aerospace industries, for instance in rockets developed by SpaceX where strength and weight are of critical

importance [7]. However, the use of FSW and other innovative methods remains relatively limited in structural applications, mostly constrained to bridge decks [8].

2.1.2 International Design Standards

Three principal international design standards were compared, from Canada, the United States and Europe. These design codes are also used in various countries where no local standard is published or specified.

In Canada, the CSA standard *S157 - Strength Design in Aluminum Structures* [9], is the governing design code for aluminum structures as specified by the National Building Code of Canada (NBCC). Aluminum bridges are designed using a different code, the CSA standard *S6 - Canadian Highway Bridge Design Code*, although most of the standard is parallel to the S157 standard. Currently, the NBCC specifies the use of the 2005 edition of the S157 standard, however a new edition was released in 2017, which is used as reference in this thesis.

The *Aluminum Design Manual* (ADM) [10], published by the Aluminum Association, is the governing code for most aluminum structures in the United States. Bridges are designed separately, based on the *AASHTO LRFD Bridge Design Specifications*, which mostly parallels the ADM.

In most European countries, design of aluminum structures is governed by the European Standard EN 1999, *Eurocode 9: Design of aluminium structures* [11]. In all cases, due to limited use and research on aluminum, these standards are mostly based on their equivalent design standard for steel. The largest differences are typically in the consideration of local buckling, to which aluminum structures are much more susceptible due to their low elasticity, and in the calculation of welded connections due to effects in the heat affected zone not seen in steel.

2.2 Fatigue in Structural Engineering

Metal fatigue is defined as the process of a member failing when exposed to cyclic loads that are much lower than the ultimate failure load of the metal. In general, a crack will first initiate as microscopic imperfections or dislocations in the metal which slowly grow with each loading cycle, in a "crack-like" fashion. Eventually, the microscopic cracks grow large enough to be considered as macroscopic cracks and the propagation phase begins. With each cycle, the crack grows by a slight amount. As the crack grows, less material is available to resist loads, and thus stresses increase locally, and the rate of crack propagation increases exponentially. Failure occurs when the net sectional area left is too little to resist the applied loads, resulting in a sudden fracture.

A distinction must be made between low-cycle and high-cycle fatigue. In general, low-cycle fatigue is on the order of less than 10,000 cycles to failure. It is characterized by large non-linear plasticity effects and is often considered in seismic design. High-cycle fatigue, on the other hand, is generally considered over 10,000 cycles but is usually in the order of 1,000,000 and more cycles. In general, material behaviour remains linear-elastic through practically the entire fatigue life, and crack propagation is relatively slow. In this thesis, "fatigue" will refer to high-cycle fatigue.

Some metals exhibit what is called a fatigue limit or endurance limit. This is the maximum stress range under which it is assumed that cracks will not grow, and thus there will be infinite fatigue life. Steel, particularly in details with a large notching effect (such as welds), has a well defined fatigue limit. It is generally agreed that plain aluminum alloys do not exhibit such a limit [12], however some research indicates that in notched samples, there is a clear fatigue limit [13].

In most civil engineering structures, the initiation phase of fatigue is usually neglected. This is because manufacturing processes and tolerances, welding, bolted holes, etc. will typically introduce cracks or crack-like details [14]. As such, cracks are considered "initiated" from the start of their service life, and only the propagation phase is considered. This is conservative and simplifies fatigue life calculations.

Since, by definition, high-cycle fatigue occurs when exposed to a large amount of cyclic

loads, most civil engineering structures are not very vulnerable to fatigue failure. Some structures however must directly consider fatigue. The most common example is in bridges, where vehicle traffic can easily bring the total number of cyclic loads into tens of millions over the life span. Other cases include crane rails, structures supporting vibrating machines such as large industrial equipment, or spires at the top of skyscrapers which are subject to high cyclic stresses from wind. Because of the slow crack growth and lack of large plasticity-induced deformations, this type of failure may occur very suddenly and catastrophically.

2.2.1 Defining Fatigue Loads

As with any other design verification, to determine that a component has adequate resistance against failure, the loads must first be defined. In general, the amplitude of cyclic loads experienced by a structure will have a random distribution based on its use and on its environment. In practice however, it is convenient to perform component testing and design using deterministic values for the loading. This is known as constant amplitude (CA) loading.

It should be noted that some studies directly consider the variability of the load by using variable amplitude (VA) loading, intended to replicate more specific loading conditions. An example would be to test components using the typical loading response from a truck driving on a bridge [15] or perhaps with the known response of a specific machine such as a pump running at 100 RPM. This thesis only considered CA loading as it was deemed more appropriate for the wide breadth of applications of aluminum structures.

Constant amplitude fatigue loading is normally defined as a function of two parameters. First, the stress range:

$$\Delta\sigma = \sigma_{\max} - \sigma_{\min} \tag{2.1}$$

and secondly, the stress ratio:

$$R = \frac{\sigma_{\min}}{\sigma_{\max}} \tag{2.2}$$

The values of $\sigma_{\min}$ and $\sigma_{\max}$ correspond to the minimum and maximum stress applied to the component and are taken as positive in tension. The stress is normally calculated using convenient and generalized dimensions for the component: for instance, σ would be calculated using the weld area when verifying for failure through a fillet weld, or the gross plate area for failure through a weld toe. Since only constant amplitude loading is considered in this case, both $\Delta\sigma$ and R are assumed to remain constant throughout the life of the component. Since the signs are positive in tension, the stress ratio R can range between 1 and $-\infty$, where $R = 0$ would correspond to full unloading every cycle and $R = -1$ corresponds to a full stress reversal every cycle.

It may also be convenient in some cases to define the fatigue loading profile in terms of mean stress and stress amplitude. The mean stress is defined as:

$$\sigma_m = \frac{\sigma_{\max} + \sigma_{\min}}{2} \tag{2.3}$$

and the alternating stress is defined as:

$$\sigma_a = \frac{\sigma_{\max} - \sigma_{\min}}{2} \tag{2.4}$$

These can be interpreted as representing, respectively, the stresses from the dead or permanent load and from the cyclic, repeating live load. These parameters are defined graphically in Figure 2.2.

The mean stress and amplitude can also be related to the stress range and ratio by the following equations:

$$\sigma_m = \frac{\Delta\sigma}{2}\left(\frac{1+R}{1-R}\right) \tag{2.5}$$

and the alternating stress:

$$\sigma_a = \frac{\Delta\sigma}{2} \tag{2.6}$$

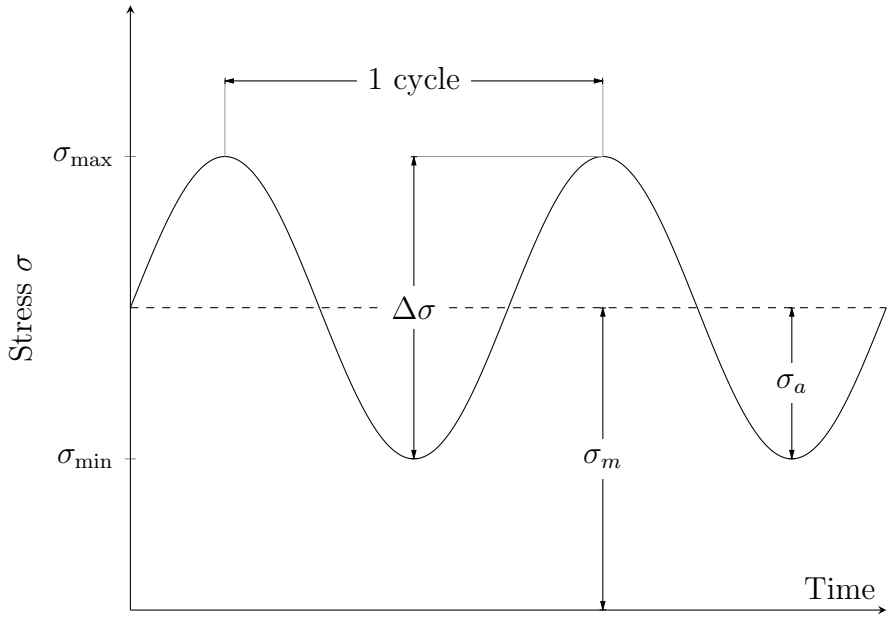

Figure 2.2: Typical constant amplitude fatigue loading sequence and parameters.

Since the stress ratio is only present in equation 2.5 for σ_m, it is clear that changing R only has an effect on the mean stress. As previously explained, the applied mean stress would normally result from a dead load such as self-weight or attachments. In welded connections however, the most significant source of mean stress is from residual stresses of welding, which often reach up to the yield strength of the metal. As such, the effect of any externally applied mean stress is practically negligible in welded connections, and normally only the stress range $\Delta\sigma$ is considered in their design for structures [14, 16]. This simplification does not always apply: in applications without welds or where welds are post-treated to change the residual stress distributions, there may be significant effects on fatigue life [17] from the mean stress.

2.2.2 Design Approaches to Fatigue

Fatigue may govern the design of some structural components and ignoring its effects when cyclic loads are present may be catastrophic. To facilitate design, many approaches to fatigue have been developed and are used in various conditions. Two common methods were studied in this thesis.

Stress-life curves and detail matching

Perhaps the most common approach to fatigue in structures is the use of standardized stress-life (S-N) curves. These curves are derived from results of large-scale laboratory tests on specific structural details (most often, connections). These details are exposed to various stress ranges ($\Delta\sigma$) and the number of cycles until failure is counted for each sample until a large data set is acquired. Statistical analysis is then performed to fit a design curve typically corresponding to the 95th percentile of survival for the specific detail [18]. This design curve normal takes an exponential form, also known as a Whöler curve:

$$\Delta\sigma = \left(\frac{C}{N_f}\right)^{\frac{1}{m}} \tag{2.7}$$

where $\Delta\sigma$ is as defined in Section 2.2.1, N_f is the number of load cycles expected over the entire life of the structure, and C and m are the two parameters characterizing the S-N curve. The S-N curves also often include a constant amplitude fatigue limit (CAFL), where components exposed to a constant stress range under the CAFL are considered to have an infinite life.

Typically, design standards will bundle details with similar values of C and m to form standardized S-N curves. Figure 2.3 shows the standard S-N curves used in the CSA S157 design standard [9]. A designer would typically consider the total amount of cycles a component or detail will see over its lifetime (N_f), and refer to the corresponding S-N curve to find the allowable stress range for the value of N_f. In typical structures, the most critical components for fatigue will be welded connections. As previously discussed,

welded connections typically have high residual stresses, which practically nullify the effects of mean stress. Most standards thus do not consider effects from the mean stress or stress ratio. As noted previously, there remains some controversy about the existence of a CAFL in aluminum. The CSA S157 standard and the Aluminum Design Manual, which essentially use the same standard S-N curves, consider the CAFL to occur at 5,000,000 cycles. The Eurocode 9 standard, however, only reduces the slope of the S-N curve at 5,000,000 cycles, and only considers a fatigue limit at 100,000,000 cycles.

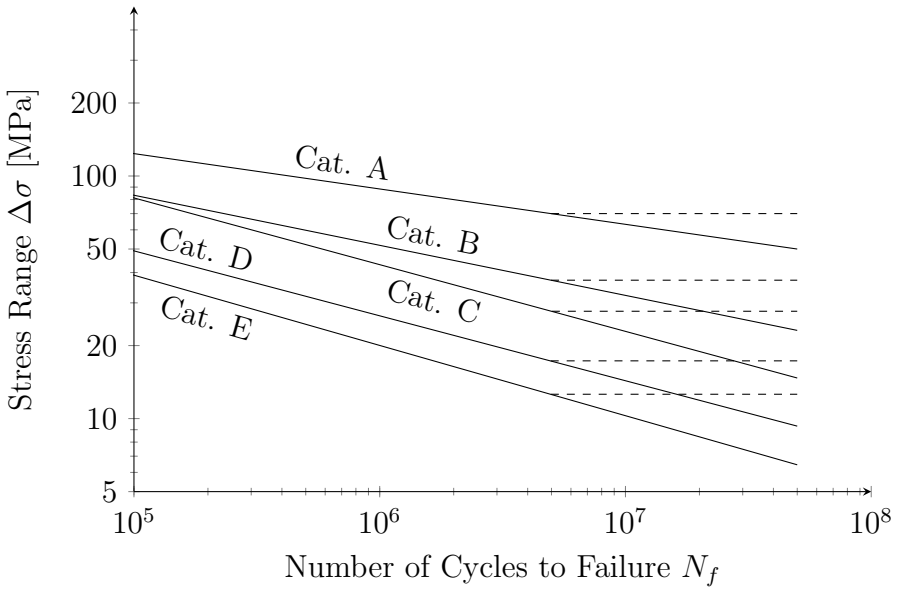

Figure 2.3: Design S-N curve categories used in CSA S157-17 and the Aluminum Design Manual. The categories correspond to different detail types, e.g. a built-up member would typically be in category B. The dashed lines represent the fatigue limit, under which no fatigue damage is assumed.

Fracture mechanics

Perhaps one of the most powerful tools in the prediction of fatigue performance is fracture mechanics. The theory of fracture mechanics was first developed as a solution to the effect of flaws on failure stress in glass. It has since expanded to be used in a variety of

design applications and materials. When dealing with fatigue design, fracture mechanics provides a convenient parameter to use, known as the *stress intensity factor* (SIF), which was derived by considering the stress field at the crack tip in an infinite plate with a crack as shown in Figure 2.4.

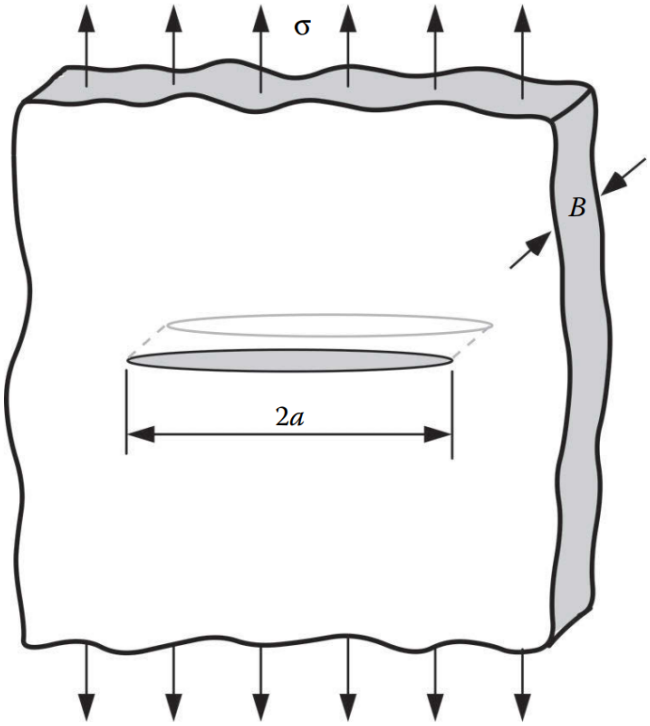

Figure 2.4: A cracked plate, infinitely wide and long, used as a basis for the derivation of the stress intensity factor K [19].

Mathematically, the stress at the crack tip can be shown to tend to infinity, following the approximate equation:

$$\sigma_{yy} = \frac{\sigma_\infty \sqrt{\pi a}}{\sqrt{2\pi r}} \tag{2.8}$$

where σ_{yy} and σ_∞ are the local and the gross stresses perpendicular to the crack, a is half the crack length and r is the distance from the crack tip, parallel to the crack. As

the $1/\sqrt{r}$ term goes to infinity, direct comparison of the stresses at the crack tip is not possible. However, the numerator $\sigma_\infty\sqrt{\pi a}$ does not tend to infinity, but still represents the intensity of the stress at the crack tip. Thus, the definition of the stress intensity factor arises naturally. In practice, it is normally defined as such:

$$K = Y\sigma\sqrt{\pi a} \tag{2.9}$$

where K is the SIF, Y a correction factor accounting for geometry and loading conditions, σ the gross applied stress (σ_∞ in Eq. 2.8), and a corresponds to half the crack length.

Equation 2.9 was originally derived by considering the stress field at the crack tip in an infinitely large plate with a crack as shown in Figure 2.4, where $Y = 1$. In general, finding the value of Y is not trivial. Some standard solutions are published for common geometries and loading cases, but more complex cases may require sophisticated approaches such as finite element analysis and energy balance methods to find Y.

Although the stress at a crack tip is shown to rise to infinity, in practice, yielding will occur which will redistribute stresses. This yielding will occur in the *plastic zone*, defined by a radius r_p [19]:

$$r_p = \frac{1}{\pi}\left(\frac{K}{\sigma_y}\right)^2 \tag{2.10}$$

where σ_y is the yield stress of the material. While the occurrence of yielding invalidates the linear-elastic assumption of LEFM, in practice, it has been found that when the plastic zone is small (*ie*, $r_p \ll a$), LEFM remains an accurate theory. In the case of thick samples, where the dimension B in Figure 2.4 is much larger than a, a plane strain condition occurs, where contraction from Poisson effects is restricted by the large thickness. This has the effect of increasing the "effective" yield strength and thus reducing the size of the plastic zone to a third of that predicted by Equation 2.10:

$$r_p = \frac{1}{3\pi}\left(\frac{K}{\sigma_y}\right)^2 \tag{2.11}$$

One should note that there are three different modes for cracks to be loaded, with mode I tending to open the crack, and modes II and III shearing the crack in different directions (Figure 2.5). Most literature focuses on mode I loading, by far the most common mode in typical structural applications. It is also the governing mode for the PJP welds studied in this project.

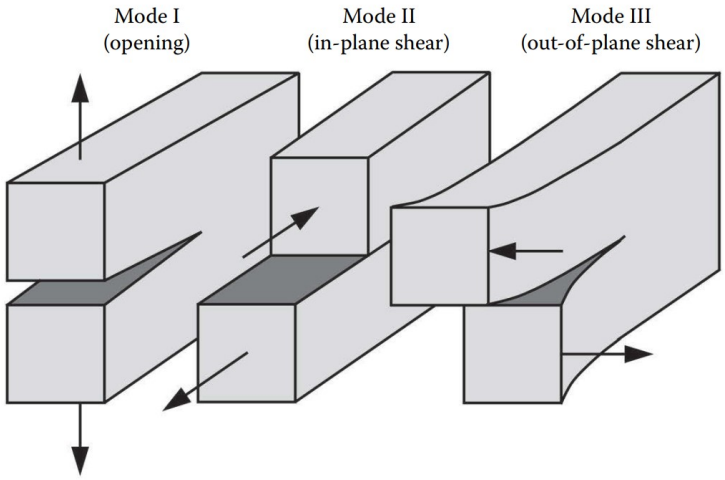

Figure 2.5: The three loading modes on a crack considered in fracture mechanics [19].

The stress intensity factor K, in one number, completely characterizes the properties of the stress field near a crack tip. By using standard procedures such as the compact tension (CT) test, a critical SIF, K_c, can be determined. This value corresponds to the SIF K in the specimen at the moment of fracture. Since the SIF is not dependent on material properties but only geometry and loading conditions (Eq. 2.9), the value of K_c determined experimentally is usually considered valid for any component made of the same material loaded in the same mode. Thus failure can be defined to occur when:

$$K \geq K_c \tag{2.12}$$

which is analogous to uniaxial tension strength, where failure occurs when:

$$\sigma \geq \sigma_u \tag{2.13}$$

where σ_u is the ultimate tensile strength.

The properties of the SIF of representing a crack tip stress field in a singular value and its material independence make it a tremendously useful tool in fatigue life prediction. After all, cracks grow only from their tips. Expanding to a fatigue context, the SIF range can be defined, analogous to the stress range:

$$\Delta K = Y \Delta\sigma \sqrt{\pi a} \tag{2.14}$$

where $\Delta\sigma$ is as defined previously. Many studies of various metals have shown a recurring relationship between the crack growth rate per cycle ($\frac{\mathrm{d}a}{\mathrm{d}N}$) and the SIF range ΔK. This is normally divided into three governing regions, as shown in Figure 2.6.

Region A is associated with essentially no crack growth and is defined by the threshold stress intensity factor ΔK_{th}. The threshold SIF is defined for a specific material as the SIF at which no crack growth occurs when exposed to cycling loads under it. In general, the value of ΔK_{th} depends on the R ratio. Components will be in this region when either the crack size is very small, or they are exposed to a small load range. Long to infinite fatigue lives are associated with this regime. On an S-N curve, this region would be associated with the endurance limit.

Skipping to region C, this region is associated with rapid and unstable crack growth. The peak SIF K_{max} (associated with σ_{max}) here is typically near the critical K_c value, and fracture (either from Eq. 2.12 or 2.13) is imminent. As failure occurs rapidly in this region, it is normally ignored in structural design for simplicity and conservatism.

Region B remains. In this case, every load cycle slowly grows the crack, but at a relatively slow and stable rate which may allow for a large number of cycles before fatigue failure. This is the region in which most fatigue analyses are performed.

The crack growth rate in Region B typically follows a power law. The most commonly

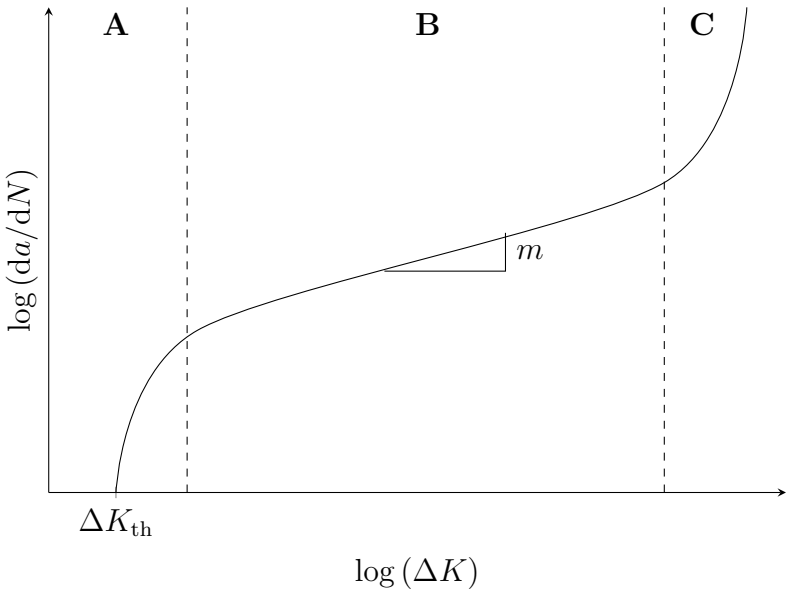

Figure 2.6: A typical $\mathrm{d}a/\mathrm{d}N$ curve with its three regions. Region A is defined by ΔK_{th} and has effectively no crack growth, B by stable crack growth, and C by rapid and unstable crack growth.

used model is Paris' law, also known as the Paris-Erdogan equation [20], which predicts the crack growth rate as a function of the SIF, and of two material parameters:

$$\frac{\mathrm{d}a}{\mathrm{d}N} = C_0(\Delta K)^m \tag{2.15}$$

where $\frac{\mathrm{d}a}{\mathrm{d}N}$ corresponds to the growth rate of the crack per cycle, C_0 and m are material constants, and ΔK is the difference in SIFs, analogous to $\Delta\sigma$ defined previously. As the crack grows, the value of ΔK increases, and the crack growth rate thus increases. This continues until fracture occurs, either because the critical SIF is reached ($K_{\max} \geq K_c$) or the net section stress is higher than the ultimate tensile capacity ($\sigma_{\max} \geq \sigma_u$). The original crack size thus has a large importance on the fatigue life of a component. For example, with a value of $m = 3$, commonly used for metals, doubling the crack size would mean that the crack growth rate would be almost tripled.

The fatigue life N_f of a component with an already initiated crack (as is assumed for

most welded joints) can be estimated by solving Eq. 2.15 for N (substituting Eq. 2.14 for ΔK):

$$N_f = \int_{a_0}^{a_f} \frac{\mathrm{d}a}{C_0 \left(Y \Delta\sigma \sqrt{\pi a}\right)^m} \tag{2.16}$$

where a_0 is the initial crack length and a_f the critical crack length for failure (either from Eq. 2.12 or 2.13). While this integral does have some closed formed solutions in specific cases, it is generally evaluated through numerical integration as Y is typically a function of a and the existence of an analytical solution is rare. This integral serves as the general basis for fatigue life predictions using fracture mechanics.

2.3 Partial Joint Penetration Welds

Partial joint penetration (PJP) welds are defined in most engineering standards as *"welds with joint penetration intentionally less than complete"* These have seldom been used in aluminum structures and essentially no research has been done on them. These welds are however often employed in steel structures where the tension capacity of a member does not need to be fully developed. In particular, significant cost savings can be found by using PJP welds in columns splices, where compressive loads can be transmitted directly by bearing and tension demands may be negligible. The welds are also commonly used in T-type joints where they may be combined with a fillet weld to provide the same strength with less filler metal than if only a fillet weld had been used. Additionally, a particular type of PJP weld often seen in truss structures is the flare-bevel groove weld, where filler metal is added in the corner radius of a square or rectangular hollow section. Examples of such PJP welds are shown in Figure 2.7.

This thesis is focused primarily on PJP groove butt welds. These welds can be separated into single and double beveled welds, which refers to whether both sides of the joint have a groove cut or only one side. Double-beveled welds are employed to reduce the amount of welding required, since to achieve the same weld throat, less weld material is required.

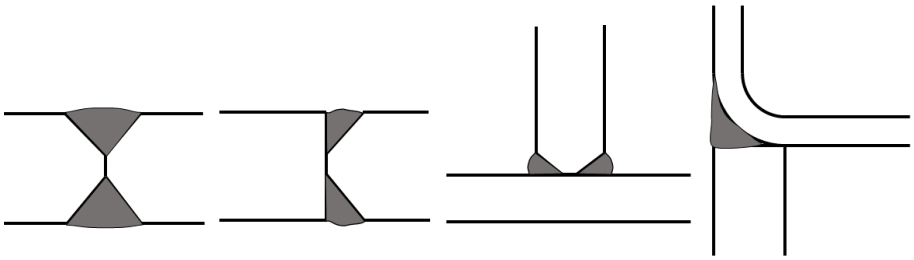

Figure 2.7: Different types of PJP weld connections. From left to right, a double-bevel PJP butt groove weld, a single-bevel PJP butt groove weld, a T-type PJP groove weld, and a flare-bevel groove weld.

Using basic trigonometry, it can be shown that the weld volume required for a single-bevel weld is:

$$V_w = \frac{1}{2} t_e^2 \tan \gamma L$$

and for a double-bevel weld:

$$V_w = t_e^2 \tan \frac{\gamma}{2} L$$

which, for a $\gamma = 60°$ groove angle, means that a single bevel weld will require 50% more filler metal than a double-bevel weld.

In most literature related to PJP butt welds, a *degree of penetration* parameter is used to define the penetration of the weld. This research project also used this parameter, defined here as such:

$$\rho = \frac{A_w}{A_g} = \frac{t_e}{t_p} \tag{2.17}$$

where ρ is the parameter describing the weld penetration, also referred to as the *degree of penetration*. A_w and A_g correspond to the net section area of the weld and the gross plate area, respectively, and t_e and t_p refer to the effective throat and plate thickness.

There is limited literature on the use of PJP welds, and it generally only pertains to

their use in steel structures. A few studies evaluated the capacity of welds subject to lack of penetration defects [21, 22], which found in general a slight increase in net section strength as defect size increases. The first direct study of PJP groove butt welds was by Popov & Stephen published in 1977 [23]. Their specific concern was on the performance of PJP welds in columns subjected to seismic loading. Six samples of wide-flange columns spliced with four different degrees of penetration were tested. Overall, it was found that as the degree of penetration ρ decreased, the net section strength increased, however no mechanism was proposed for this phenomenon.

The behaviour of PJP groove butt welds was most thoroughly studied by Gagnon and Kennedy [24] for steel structures. Their research consisted of tests on 75 samples of PJP single-bevel groove welds of different degrees of penetration in structural steel, similar to the second weld type in Figure 2.7. The authors found that in general, a lower bound for the strength (T_r) of a PJP butt weld connection could be established as such:

$$T_r = A_w \sigma_u \tag{2.18}$$

where σ_u corresponds to the ultimate strength of the base metal. This lower bound for strength applied even when samples had a significant eccentricity from warping during the welding process. In fact, eccentricity had no apparent effect on strength, due to the ductility provided by the welds.

In welds with low penetration, a significant increase in strength was found and was theorized to be due to lateral restraint existing in the welds. As ρ becomes smaller, more of the plate area between the two welds remains unloaded and thus is not subject to Poisson effects or yielding. This constrains movement in both the direction of the thickness and the width of the sample, creating a state of biaxial plane strain (*ie.* if ε_x is the principal strain in the loading direction, $\varepsilon_y = \varepsilon_z = 0$). When using the Von Mises criterion for failure, the authors found that the effective failure stress in the case of biaxial plane strain can be calculated as such:

$$\sigma_{u,eff} = \frac{1-\nu}{1-2\nu}\sigma_u \tag{2.19}$$

where ν is the Poisson ratio (usually taken as 0.30 for steel and 0.33 for aluminum). The authors thus found that in a biaxial plane strain condition, the net ultimate stress in the weld would theoretically be more than twice the value of σ_u (a value of $\nu = 0.35$ was used to account for yielding in the steel).

From their experimental results, the authors fitted the following polynomial as a more accurate estimate of ultimate strength of the weld based on the degree of penetration:

$$T_r = (1.55 - 1.16\rho + 0.61\rho^2)A_w\sigma_u \tag{2.20}$$

This equation yields a maximum possible increase in ultimate strength of 55%, much less than estimated by theory. This was attributed to the fact that ideal plane strain conditions may not be present in actual samples. The authors also noted that this polynomial fit may only apply for the specific width to thickness ratio of their samples and would be expected to change at different ratios due to reduced or increased lateral restraint.

Gagnon and Kennedy also studied the expected failure plane for the PJP groove butt weld connections using three failure criteria. First, using the maximum principal stress, the failure plane was estimated to occur at $\theta = 0°$ from the normal to the weld at an ultimate failure stress of F_u (Figure 2.8a). Using a maximum shear stress theory, the failure plane was estimated to occur at an angle $\theta = 45°$ also with an ultimate failure stress of σ_u (Figure 2.8b). Finally, using the von Mises criterion, the failure plane was estimated to occur at $\theta = 30°$ with an ultimate failure stress of $0.943\sigma_u$ (Figure 2.8c).

With a single-bevel groove weld as in this case, it is evident that the failure plane will occur on the side with the weaker material, and that the weld will thus be governed by the weaker strength. Since steel welds are practically always designed with the weld metal stronger than the base metal, this explains the relationship between the connection strength T_r and the base metal strength σ_u as seen in Equations 2.18 and 2.20. In the case where a double-bevel is used, the situation becomes less clear, as the predicted failure planes may go through the weld metal depending on the groove angle and the failure criterion (Figure 2.9).

However, in their experimental results, the authors found that the observed failure

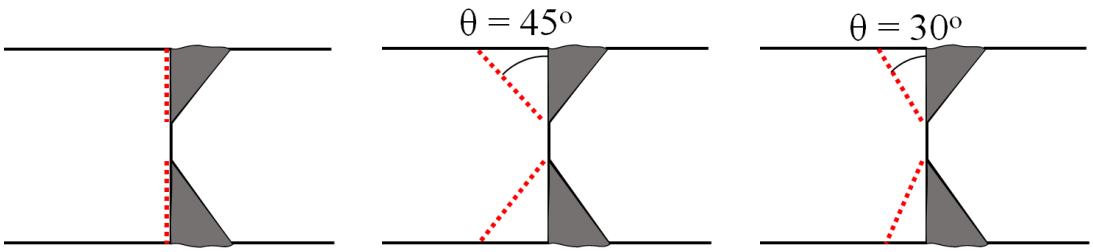

(a) Maximum principal stress criterion

(b) Maximum shear stress (Tresca) criterion

(c) von Mises criterion

Figure 2.8: Three failure surfaces (indicated by dashed lines) theorized by Gagnon and Kennedy [24]. θ is the failure plane angle. The failure surface is assumed to occur in the base metal as the weld metal is stronger.

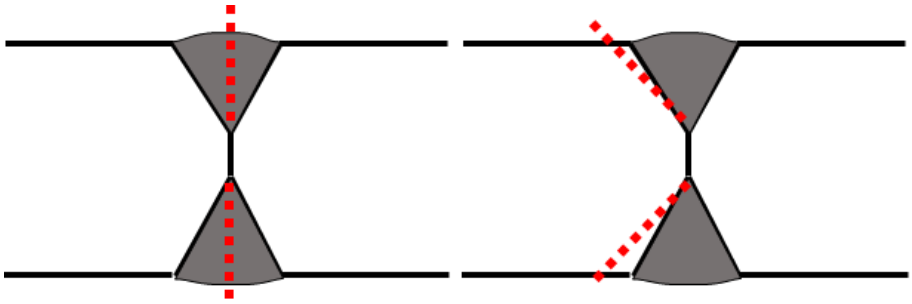

Figure 2.9: In double-beveled groove welds, the maximum principal stress criterion always predicts a failure plane through the weld metal (left), while other failure planes may occur in the base metal (right).

planes did not correspond to that predicted by theory: *"It appears that the partial welds do not know what failure theory to follow and that the behaviour is governed more by the angle of the fusion face to the throat [...]"*. In this citation, the angle of the fusion face refers to the angle formed by the weld cross-section on the unbeveled side of the weld, as shown in Figure 2.10.

Indeed, the failure planes observed in the study were consistently in or near the fusion face of the weld. More recently, Reynolds et al. [25] also found that the fusion face had a large influence on the failure plane of steel PJP welds, and that using the base metal ultimate strength yielded accurate results. This suggests that failure may always occur at

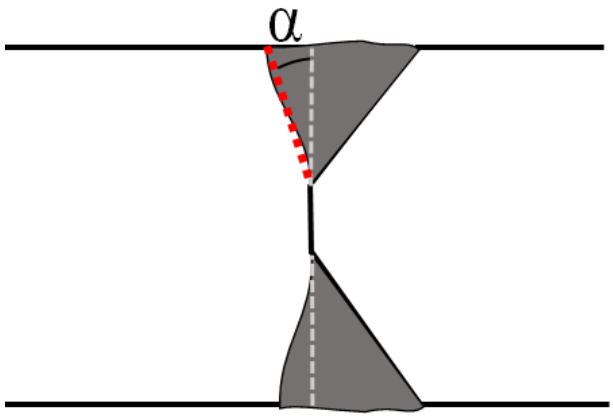

Figure 2.10: Fusion during the welding process extends past the groove preparation (dashed in light grey) at an angle α.

the fusion face and would thus always be governed by the base metal (or heat affected zone, in aluminum) strength, regardless of the groove preparation angle or if the connection is double-beveled or single-beveled.

2.3.1 PJP Welds in International Design Codes

Various aluminum design codes address partial joint penetration welds. The Canadian, American and European standards were reviewed for this project.

Canada - CSA S157

No design equations are given for the strength of PJP welds – instead, the designer is advised that "*partial penetration groove welds should not be used for joints carrying calculated forces*" (Clause 15.2.1 [9]). In the standard's commentary, a reference is given to the requirements for PJP welds in CSA W59.2 - Welded Aluminum Construction. In the current version of CSA W59.2, published in 2018, PJP groove welds are addressed specifically for the determination of the effective throat. In general, the effective throat may only be determined by procedure qualification testing for PJP groove welds. An exception

is given for PJP welds made with the GMAW (MIG) or GTAW (TIG) processes, where the effective throat is taken as equal to the groove preparation depth if the groove opening angle is above 60°.

In practice, this suggests that a standard net section check can be performed to find the strength of PJP groove welds in plates. In mathematical form:

$$T_r = \phi A_w \sigma_{wu} \tag{2.21}$$

where T_r is the welded connection's strength, ϕ is the performance factor, A_w is the weld area, and σ_{wu} is the ultimate welded tensile strength. A_w is well-defined for plates as equal to the effective throat multiplied by the length. However, the other two parameters are not.

In CSA S157, ϕ is taken as either 0.75 in the case of groove welds, and as 0.67 for fillet welds. These are defined in the standard's commentary to reduce the calculated strength from the mean value by two standard deviations, or to be at approximately the 95th percentile of survival. The commentary also however notes that the factors selected are meant to parallel the factors used in Canadian steel structures in the CSA S16 standard. However, there is a discrepancy between the S157 standard and the S16 standard, where for PJP groove welds, ϕ would be taken as 0.75 by S157 and as 0.67 by S16.

This may be explained by an implicit assumption in the S157 standard that groove welds will only be detailed with complete penetration given the warning against PJP welds described previously. In complete joint penetration welds, failure is usually assumed to occur in the heat affected zone for typical structural alloys (however, in some alloys, the weld metal strength will govern). Thus, a ϕ value of 0.75, associated with tensile rupture, would generally be appropriate for a CJP weld. However, for a PJP weld, failure could occur either in the weld metal or the base metal. The CSA S16 standard approaches this by defining the strength of PJP welds as such:

$$T_r = \min \begin{cases} \phi_w A_n \sigma_u \\ \phi_y A_g \sigma_y \end{cases} \tag{2.22}$$

where $\phi_w = 0.67$ and $\phi_y = 0.9$. A ϕ factor of 0.67, as specified in S157 for fillet welds where failure is expected to occur in the weld metal, would thus appear more appropriate. This would be consistent with the S16 standard for steel structures.

The other uncertainty is in what ultimate strength to consider. Groove welds in aluminum with complete penetration are usually checked using the minimum of the base metal strength in the heat affected zone (HAZ) and the weld metal strength. For the 6061-T6 alloy welded with 5356 filler, these strengths are respectively 165 MPa and 240 MPa – thus, in a CJP weld, failure should occur in the HAZ. However, in a PJP weld, the reduced net cross-section at the weld could induce failure through the weld even with the weld metal being stronger. This relates to the research by Gagnon and Kennedy [24]. There is thus a difficulty in assessing what strength value to use for σ_{wu}.

The *Canadian Highway Bridge Design Code* (CSA S6-14)

For most bridges in Canada, design is governed by the *Canadian Highway Bridge Design Code*, CSA S6-14, of which Section 17 covers aluminum structures. The provisions are essentially the same as CSA S157-17, except that partial penetration groove welds are explicitly forbidden for connections carrying calculated forces.

USA - *Aluminum Design Manual*

For strength design, the ADM directly addresses PJP welds. Similarly to CSA W59.2, it defines the effective throat as the depth of groove preparation, except that the minimum groove angle is 45° instead of 60° as in CSA S157. The strength of the weld is however reduced by 40%. According to the commentary, this is to account for the notching effect of the incomplete penetration, referring to the same factor applied in steel PJP welds. The design equation is thus taken as

$$T_r = \phi A_w (0.6\sigma_{wu}) \tag{2.23}$$

where ϕ is taken as 0.75, A_w is defined in the same way as in CSA S157 / CSA W59.2, and σ_{wu} is the least of the base metal HAZ and the weld metal ultimate strengths. This provides a conservative and straightforward design equation for American designers of aluminum structures. The main American bridge design standard, the AASHTO LRFD Bridge Design Specifications, specifies that the 40% reduction in strength should only be taken on the weld metal strength, and not on the base metal HAZ strength. This makes intuitive sense as the weld root, most subject to the notching effect of incomplete penetration, consists only of weld metal.

Europe - *Eurocode 9*

The Eurocode 9 – Part 1 standard directly addresses PJP welds and provides design equations for their use. These however come with a warning to the engineer that they should only be used for secondary and non-load bearing members. As in the other standards, an effective throat must be found, however the standard provides little guidance on how to do this.

The strength equation for groove welds in Eurocode 9 can be manipulated to be the same as for CSA S157 (Equation 2.21) with ϕ (actually, $1/\gamma_{Mw}$ in Eurocode 9) equal to 0.8 and A_w calculated by multiplying the effective throat and weld length. Where the Eurocode differs is in the strengths to be used – for the 5356 weld metal, its strength is taken as 190 MPa instead of 240 MPa as in CSA S157 and the ADM, a reduction of 20% in strength. The base metal HAZ strength of 175 MPa is higher than the CSA S157 and ADM values by 6%. As in the ADM, the net section is used to check both the base metal HAZ and weld metal strengths.

2.3.2 Fatigue in PJP Welds

There has been relatively little research on the fatigue performance of PJP welds, especially in aluminum.

Partial penetration steel welds

In steel, a few studies on the performance of PJP welds have been performed [26–29]. These have often been to study the effects of a lack of penetration defect in complete penetration welds. Overall, the studies highlighted some key recurring properties of PJP welds loaded in fatigue:

- Crack growth almost always begins at the weld root, regardless of the presence of reinforcement. Fatigue at the weld toe may occur in cases where the degree of penetration ρ is more than 80% and the weld reinforcement is not ground off.
- The notching effect of the lack of penetration significantly impacts the fatigue performance of PJP butt welds, with the fatigue limit at a stress range less than half of with CJP welds.
- Removing the weld reinforcement, which typically increases fatigue performance in CJP welds, significantly reduces the performance of PJP welds.
- Despite the large crack-like defect, one author [26] theorized that a crack initiation phase may occupy almost half the total fatigue life of the sample. This may be related to the residual stresses in the weld preventing crack opening. There is however extremely limited data.

Partial penetration aluminum welds

For aluminum welds, research is very limited. Two major experimental programs are present in literature. Two main data sets for the fatigue performance of PJP welds were identified.

The first data set comes from the University of Illinois at Urbana-Champaign [30]. The data comes from a project which is almost completely analogous to a study in steel cited previously [26]. Almost 100 weld samples were tested at varying degrees of penetration, from $\rho = 45\%$ to $\rho = 98\%$. The samples consisted of plates with thicknesses of 9.5 mm

[3/8”] and 25 mm [1”], made of 5083 alloy base metal and welded with 5183 filler metal. Half of the samples had the weld reinforcement removed and the other half was left intact. The fatigue tests were run at two nominal stress ranges defined over the gross area: 82.7 MPa and 131 MPa. The stress ratio was $R = 0$ in all tests.

The second data set is from a set of studies in Germany in the late 1990s to early 2000s which researched the fatigue performance of aluminum PJP welds [31,32]. Comprehensive fatigue tests of 5 and 25 mm thick plates joined with PJP welds were undertaken. These samples were made using the 5083 alloy base metal and 5183 filler metal, as in the first data set (one co-author in the study was also present in the Illinois study). The samples had degrees of penetration of $\rho = 69\%$ and $\rho = 78\%$ respectively, which includes the thickness of the weld reinforcement. The reinforcement was considered as the experiments showed that fatigue cracks grew through the weld reinforcement (Figure 2.11).

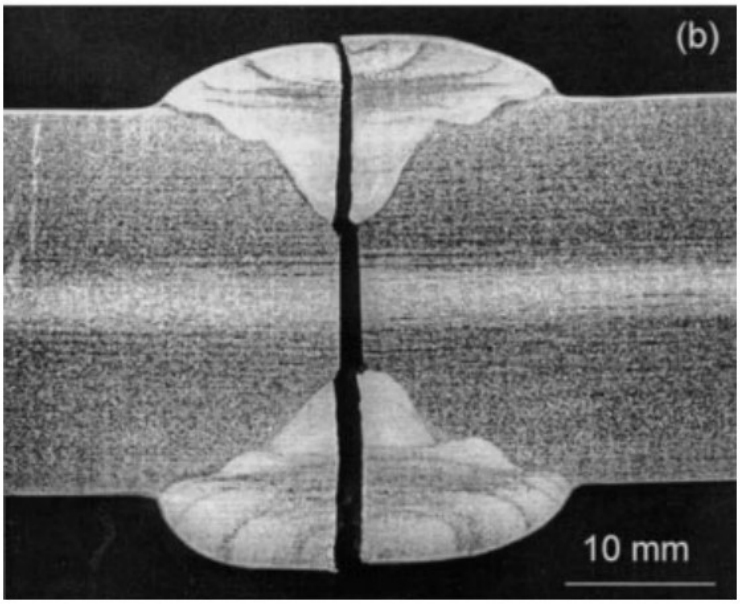

Figure 2.11: The fatigue crack grows from the root directly through the weld and its reinforcement in an aluminum PJP weld [31].

This second data set was originally designed to research weld repair in aluminum vehicle components. Because of the difference in application, some key characteristics of the

samples were not as would be common in a structural application. First, the 5083 alloy is somewhat less common in structural applications, which typically make more use of 6000-series alloys. Second, all samples were heat-treated to anneal the metal and remove practically all residual stresses. This is not representative of welds as they would be observed in structures. Lastly, the weld reinforcement was not removed from the samples. As explained when discussing fatigue in steel PJP welds, the reinforcement brings significant improvements to fatigue life as the crack grows from the weld root. Nevertheless, the study provides valuable insight in the behaviour of aluminum PJP welds.

Overall, further insights can be gained from these studies on the performance of aluminum PJP welds, additional to what was previously listed on steel samples.

- All the fatigue properties of PJP welds mentioned when previously discussing steel samples also apply to aluminum PJP welds.
- As mentioned with steel, there are varying opinions about the presence of an initiation phase. It should be noted that the literature suggesting that an initiation phase occurs stems mostly from one research center [26, 30].
- An increase in weld porosity is typically associated with PJP welds, however the overall lack of penetration defect consistently governs fatigue performance.
- The base metal thickness has little effect on fatigue.

Design S-N Curves for Aluminum PJP Welds

Neither CSA S157 or the Aluminum Design Manual provide design S-N curves or details for PJP welds. However, Eurocode 9 does provide such curves for design. Additionally, the International Institute of Welding (IIW) has published its *Recommendations for Fatigue Design of Welded Joints and Components* [18] which also includes a design curve for PJP welds (although it comes with the recommendation to use a fracture mechanics approach). These two curves are shown in Figure 2.12, with the Category E CSA S157 / ADM curve as a comparison. One should note that no consideration is made for the alloys used in the

structure - indeed, the fatigue properties of aluminum are typically assumed not to vary considerably by alloy.

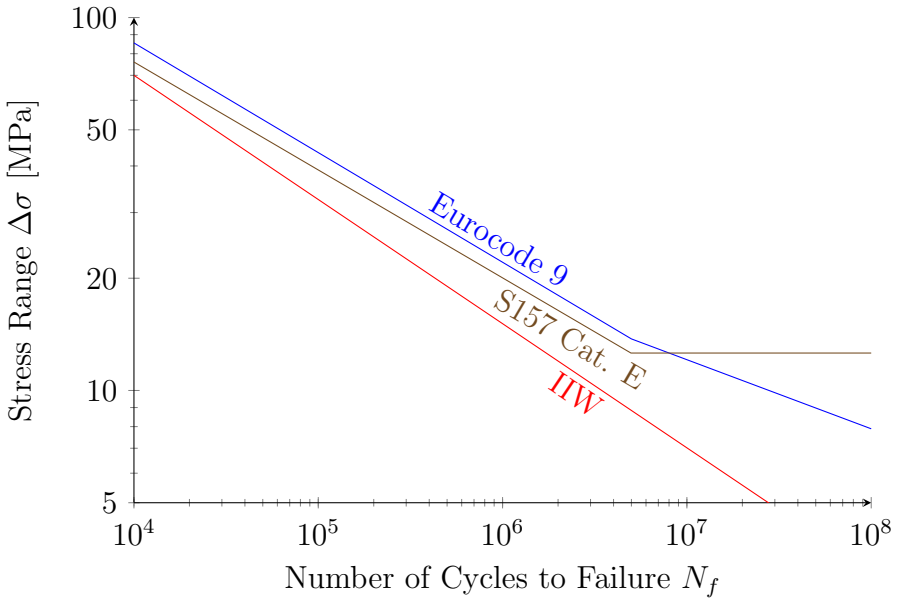

Figure 2.12: Design S-N curves for PJP butt welds used in Eurocode 9 [33] and in the IIW *Recommendations* [18]. The CSA S157 Category E curve is also superimposed for comparison.

Chapter 3

Experimental Program

A comprehensive experimental program was designed to study the behaviour of PJP butt welds, both in static and cyclic loading.

3.1 Samples

In total, 84 plate samples were fabricated to be tested under static and fatigue loading. The samples all consisted of two plates welded together using double V-groove PJP welds, with a 60° groove angle (see Figure 3.1). Two plate thicknesses were evaluated, 9.5 mm (3/8") and 19.05 mm (3/4"), with a constant width of approximately 62 mm. The samples were not "dog-boned" as is often the case in tension and fatigue tests, because the lack of penetration was so severe that there was no concern of failure occurring anywhere but at the weld. Groove preparation depths (S on Figure 3.1) were varied in 1 mm increments from 2 mm to 7 mm. The welds were ground flush at the toe. Since crack initiation was expected to occur at the root, this was deemed conservative, as it removed excess material (the so-called weld reinforcement), which cannot be counted on due to its highly variable geometry, and could artificially increase strength slightly if left in place.

The samples were manufactured by three different fabricators located in New Brunswick. Two of the fabricators (Fabricators A and C) used a 100% argon shielding gas. Fabricator

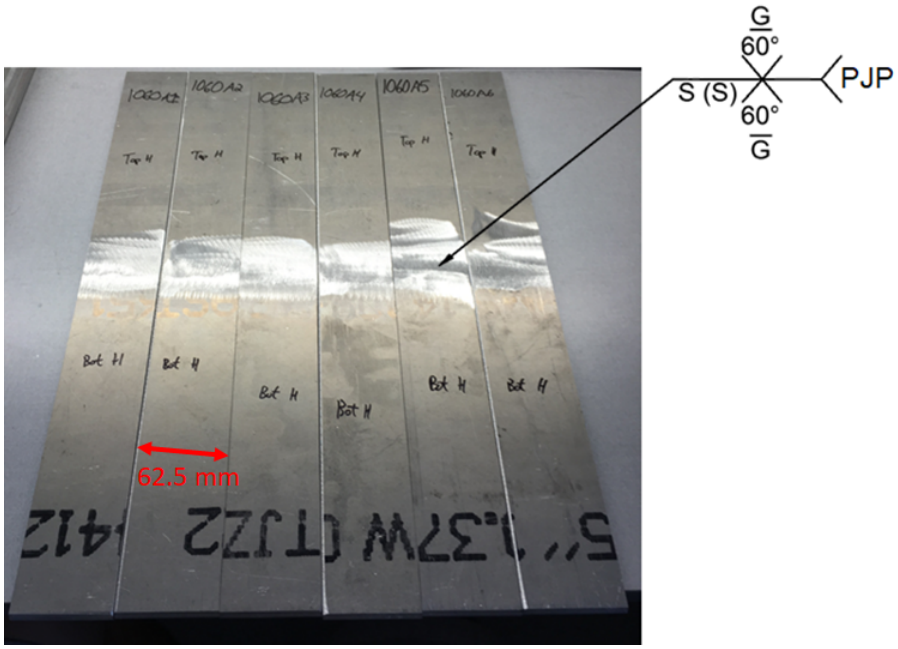

Figure 3.1: Samples with weld symbol detailing the PJP groove welds. S is the parameter representing the required effective throat and the groove depth, which were taken as equal.

B used a 50% argon – 50% helium mix, which generally produces deeper penetration and reduced porosity. In all cases, the base metal alloy was 6061-T6 and the weld metal alloy was 5356.

3.1.1 Sample Designation

The samples were all designated in consistent fashion for ease of identification as such: XXYYFN. XX represents the nominal thickness of the sample, rounded to the nearest 10 mm. YY is the nominal degree of penetration ($\rho_{\text{specified}}$) in percent, rounded to the nearest 10%. F corresponds to the fabricator (A, B or C), and N is the sample number for that category. For instance, the 4th sample in the batch with 9.5 mm [3/8"] thickness, 2 mm groove depth ($\rho = 42\%$), from fabricator A, would have the designation 1040A4. Table 3.1 summarizes the different sample types and their relevant parameters.

Table 3.1: Tested samples and experimental parameters

Sample type	Number of Samples	Plate thickness t (mm)	Groove depth S (mm)	Degree of penetration ρ (%)	Shielding gas
1040A	6	9.53	2	42	100% Ar
1060A	6	9.53	3	63	100% Ar
1080A	6	9.53	4	84	100% Ar
1040B	6	9.53	2	42	50% He - 50% Ar
1060B	6	9.53	3	63	50% He - 50% Ar
1080B	6	9.53	4	84	50% He - 50% Ar
2050C	16	19.1	5	53	100% Ar (Ultra-pure)
2060C	16	19.1	6	63	100% Ar (Ultra-pure)
2070C	16	19.1	7	74	100% Ar (Ultra-pure)

3.2 Macroetching and Hardness Mapping

In addition to the static and fatigue test specimens, for each 9.5 mm thick sample type (six in total), a 25 mm wide strip was cut at the start and end of the weld. The strips were then polished and etched to show the grain properties of the weld and heat affected zone (HAZ). The same samples then had their local hardness mapped over the cross-section of the weld and the mapping was calibrated to the etched image.

In general, sample preparation procedures vary as there are a large range of potential samples and applications for macroetching. There are however the ASTM standards E3 *Standard Guide for Preparation of Metallographic Specimens* and E340 *Standard Practice for Macroetching Metals and Alloys*, which provide best practices for macroetching [34,35]. These were generally followed for the preparation of the samples.

The samples were first cut and then mounted in a heat-activated resin, where the resin in powdered form is set by applying high heat and pressure in a specially designed mounting

press. The samples, now mounted in a puck, were sanded with progressively finer grit until a flat and smooth surface was achieved. The samples were then polished using diamond abrasives down to approximately 0.5 µm. Once polished and cleaned, the last step consisted of etching the samples. For this purpose, Keller's reagent was used, which consists of a mixture of hydrochloric acid, nitric acid, and hydrofluoric acid. A quick immersion of the sample with the reagent spectacularly reveals grain boundaries almost immediately. Care must be taken not to apply the reagent for too long (on the order of seconds), or else the sample may become "overetched", where the entire surface of the sample is etched and grain boundaries are not visible.

In all steps, minimizing heat was a major consideration to ensure that the microstructure and properties of the HAZ are not affected. When cutting the samples, a liberal amount of coolant was used both for lubrication and heat dissipation. The mounting press was run at relatively low temperature (approx. 150 °C) to minimize the heat input to the aluminum. During sanding and polishing, water was used as a lubricant and coolant to control temperature.

The etched samples were then processed using a Clemex CMT automated microhardness testing system (Figure 3.2). First, a 5x magnification lens was used to capture and stitch together images of the entire weld cross-sections. These stitched images were used to evaluate the grain properties of the samples, and were the final product of the macroetching procedure.

Once the imaging was completed, the micro-hardness testing procedure began. A grid was established over the sample, setting approximately 400 data collection points per sample, at a typical spacing of 600 µm across the thickness and 700 µm across the width. Figure 3.3 shows a typical grid applied on a weld cross-section. This grid spacing was selected to be able to cover the extents of the weld and heat affected zone in a reasonable amount of time. The spacing was also well above recommended spacing limits, at about 12 times the typical indent size while the minimum recommended spacing is 2.5 times [36].

At every point on this grid, the Clemex tester automatically performed a Vickers hardness test. During these tests, a 100 gf (∼1 N) load was applied for a duration of 10 seconds

Figure 3.2: The Clemex CMT automated microhardness testing system. *Image from Clemex.*

by a standard diamond-shaped indenter (Figure 3.4). The dimensions of the diamond-shaped indent were then automatically measured by the Clemex system and were used to calculate the Vickers hardness with the standard formula [36]:

$$HV = 1.8544\frac{F}{d^2} \tag{3.1}$$

where HV is the Vickers hardness number, F is the applied force in kilograms-force and d, in millimeters is the average of d_1 and d_2 shown in Figure 3.4. The hardness measured with this method was then used to determine the extents of the heat affected zone in the samples. As an example, if the indentation width d is measured as 0.5 mm after applying a 0.5 kgf load, the Vickers hardness would be calculated as 370 HV.

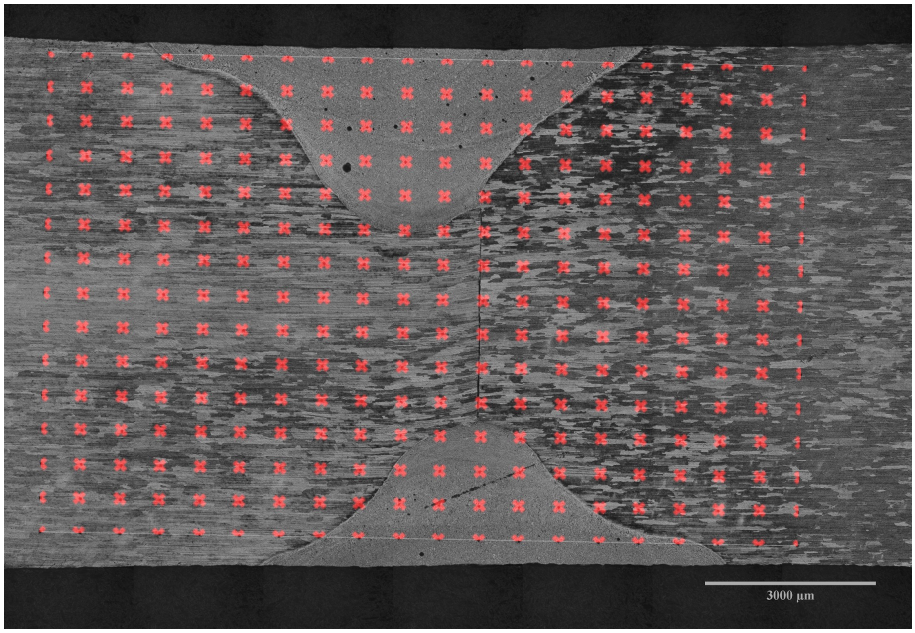

Figure 3.3: Typical grid pattern used in microhardness testing of the samples, in this case from the 1060B sample type.

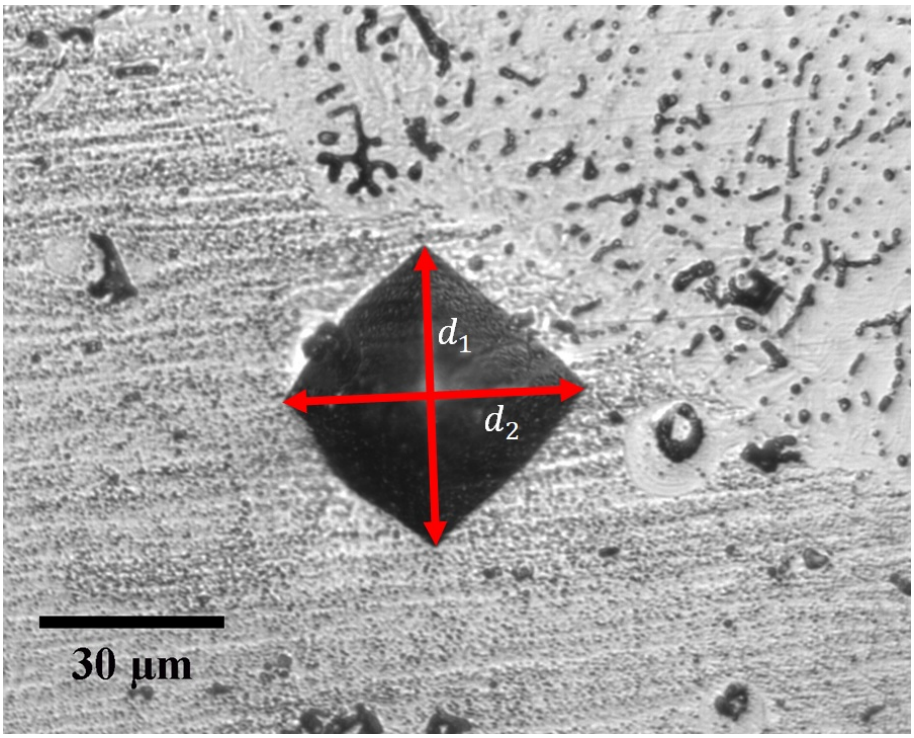

Figure 3.4: A typical indent from the microhardness test. The average of d_1 and d_2 is used in Eq. 3.1 to calculate the Vickers hardness.

3.3 Static Tests

Static tests were performed to failure on two samples of each type (Table 3.1) to study their strength and loading behaviour. Samples were loaded monotonically in displacement control at a constant testing rate in tension until failure. The tests were performed in the University of Waterloo's Structures Laboratory. The loading frame used was an MTS Criterion C64 servo-hydraulic machine, with a 500 kN capacity.

In the first tests, two 50 mm extensometers were used on opposing corners of the sample, as shown in Figure 3.5. This allowed correcting for accidental bending and eccentricities from grip misalignment or weld warping. Using the typical assumption that the eccentricities produce a linear bending strain profile, the average of the strain at each corner is the strain at the neutral axis, where there is no bending strain, and thus only the tensile strain is present. Early analysis showed that the difference in strains at each corner was mostly negligible due to redistribution once yielding began. Thus, in the 19 mm samples, only one extensometer was used to allow unobstructed measurements using digital image correlation.

3.3.1 Digital Image Correlation

In the 19 mm thick samples, digital image correlation was used to identify local strain patterns around the welded areas. Digital image correlation (DIC) is a relatively modern technique, which uses image processing to analyze localized strain during testing. It allows high precision measurements of strain at any location of the studied surface. To achieve these measurements, a complex algorithm tracks the displacement of unique points on the surface as the load is applied. By measuring the relative displacement between points, a strain field can be generated, showing local strains at a high resolution.

The principal challenge with this technique is in obtaining a field of unique points, which can be identified and tracked throughout the loading sequence. In general, metal surfaces are too smooth and homogeneous for the algorithms to reliably track enough unique points. To permit reliable tracking and high precision measurements, the conventional technique

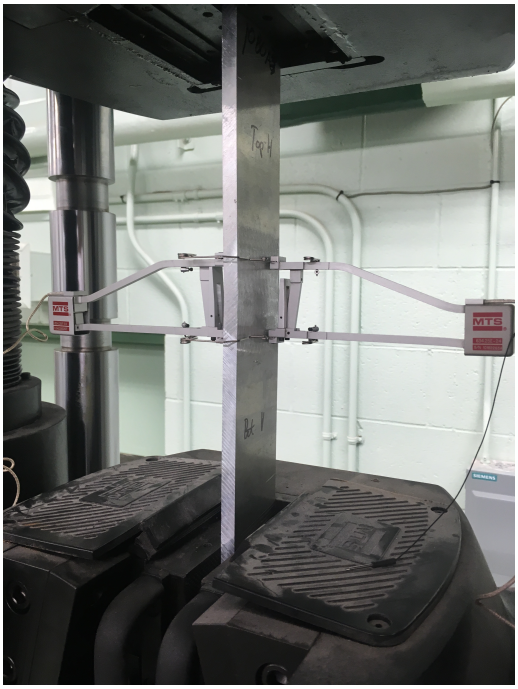

Figure 3.5: Sample in loading frame with two extensometers at each corner.

employed is to apply a speckle pattern to the studied surface. To do this, the surface was first painted white, and then, black spray paint was applied lightly and from a relatively far distance, allowing only some flakes of black paint to land on the surface. Because of the inherent randomness of spray-painting, the flakes on the surface were in all practical terms completely unique and their high contrast with the white surface made them very straightforward to track with DIC algorithms. Figure 3.6 shows a speckle pattern applied using this method on one of the 19 mm samples.

Another critical component of DIC measurements is the quality of the images. A blurry or low resolution image will inherently be less precise than a sharp, high resolution image. Making use of a readily available technology, a smartphone was used to film the tests in ultra-high definition (4k UHD). The high resolution allowed precise measurements and the small smartphone provided great versatility to maneuver within the safety constraints of the laboratory.

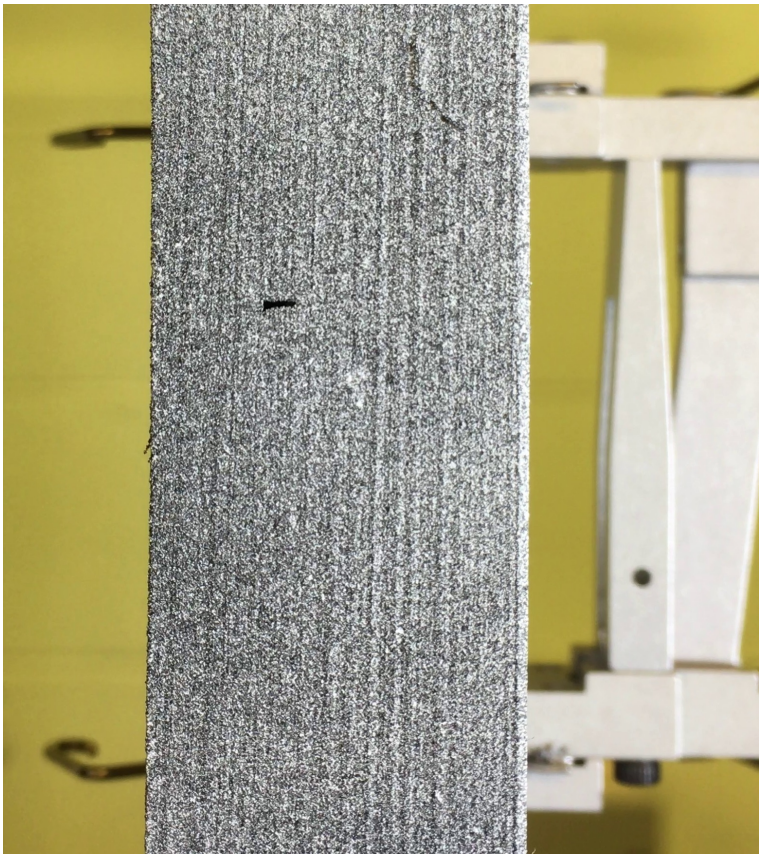

Figure 3.6: Speckle pattern applied on a 19 mm thickness sample.

3.4 Fatigue Tests

An extensive fatigue testing program was developed with a total of 56 samples. The testing program was undertaken in the University of Waterloo's Civil Engineering Fatigue Laboratory, in a universal test frame rated for cyclic loads ranging between ± 100 kN. All tests were performed at room temperature (∼21 °C). A constant amplitude (CA) loading scheme was used, with the cyclical load in a sinusoidal shape. The cycle frequency varied between 10 Hz and 35 Hz, with the higher loaded samples tested at the lower frequencies to avoid excessive resonance in the laboratory.

Net section stress ranges varying between 20 MPa and 115 MPa were chosen; these

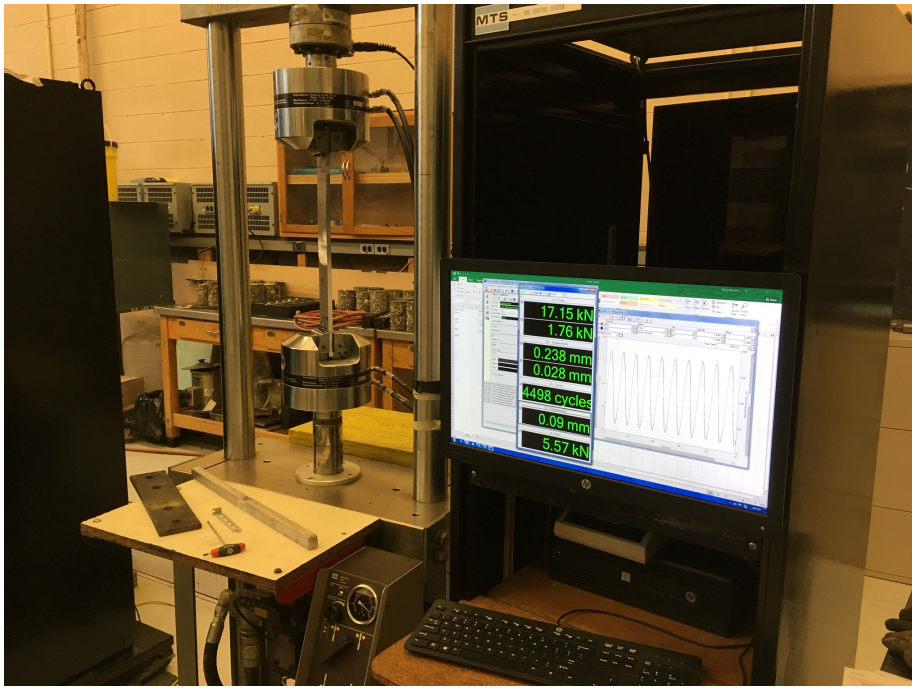

Figure 3.7: The frame setup for fatigue tests.

were predicted to produce a life range varying between 10,000 and 10,000,000 cycles. For these tests, the stress range was defined by the net section area across the weld, consistent with past literature and developed models. Measurements of the actual net section area could only be performed after failure, so nominal dimensions were used as opposed to as measured. Two stress ratios were tested: $R = 0.1$ and $R = 0.5$. The purpose of the two different stress ratios was to determine qualitatively the influence of residual stresses from welding.

A displacement limit of approximately 0.05 mm above the displacement at peak load was imposed. This consistently stopped the test automatically as soon as the sample entered the rapid crack propagation phase just before failure (Figure 3.8). Once the test was started again after tripping the displacement limit, failure normally occurred after no more than 500 cycles. Observation of the last cycles served to confirm that the crack was growing from the root as predicted, and showed that yielding and plasticity effects only

took place at a large scale for a few cycles before failure.

Figure 3.8: A cracked sample just before failure. The weld is difficult to see as its reinforcement was ground off, but the crack grows through it.

3.5 Weld Throat Determination

A critical component of the experimental program was in determining accurately the actual size of the welds. Because the net section stress is defined by the load and by the weld area, any deviation between the specified and actual weld sizes could significantly affect the calculations of strength and fatigue performance. Initially, actual weld size was to be determined by measuring the effective throat of macro-etched samples. However, early tests showed that there were significant variations in the effective throat along the length of the weld, and that more frequent measurements would be required.

A new technique was conceived where images of the failure plane were taken after the samples were tested and had failed at the weld. An edge detection algorithm was then employed on the images to measure the total cross-sectional area that was **not** welded, which was subtracted from the gross cross-sectional area (Figure 3.9). The unwelded area was used to minimize the influence of permanent deformation. As essentially no load was carried by the unwelded area, there was no plastic deformation even in static tests to failure. In fatigue tests, since the crack grows from the root, large deformations only develop at the exterior edge of the weld, and only just before failure, which translates to negligible plastification in the unwelded area with fatigue samples as well. This measurement method is also consistent with past literature [23, 24] (though in these studies, the unwelded area was only measured manually at a few points).

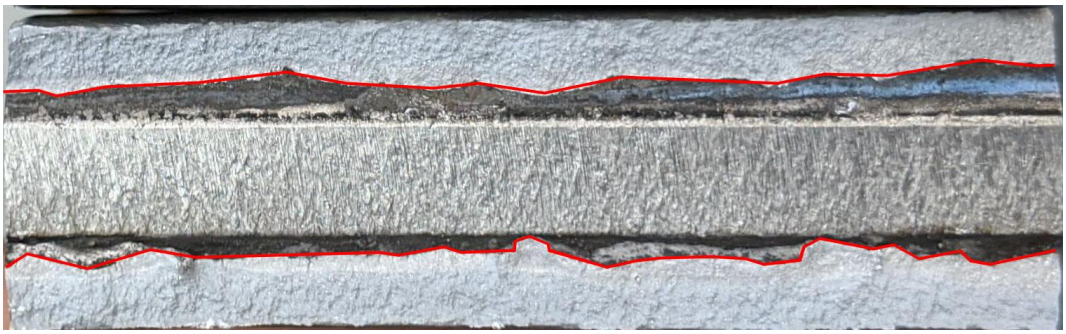

Figure 3.9: Failure plane image showing unwelded area boundaries used to calculate actual weld size. The darker area near the red lines consists of the base metal where a lack of fusion or penetration occurred.

3.5.1 Weld Roughness Measurements

It was theorized that the large variations in effective throat may have an effect on the fatigue performance of the welds. To measure this, an investigation of the effects of roughness was undertaken. Using the image processing methodology previously described, 100 equally spaced points were defined along the weld root, shown in Figure 3.10. This data was used to establish a consistent measurement of roughness and to measure its effect on fatigue performance, as described in Section 6.4.5.

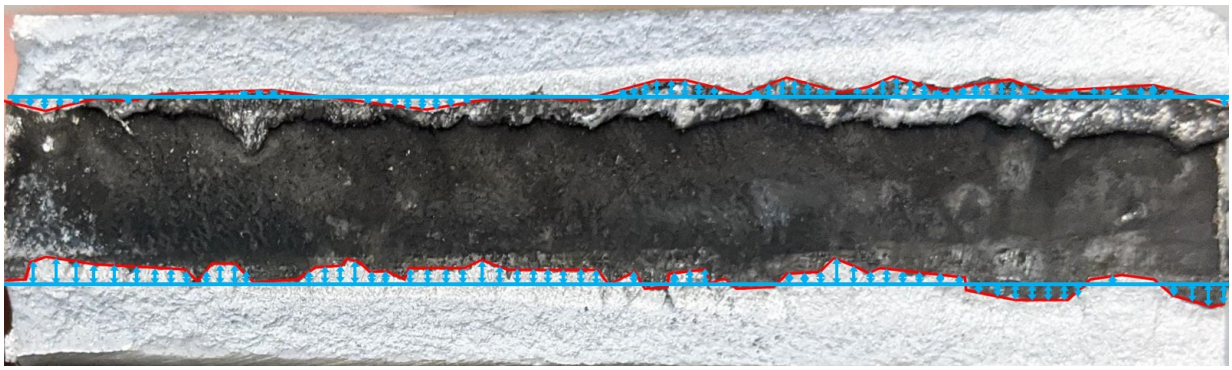

Figure 3.10: Deviations from the mean effective throat of samples were measured at 100 equally-spaced points along the width for the top and bottom welds and used to analyze the weld roughness.

Chapter 4

Fracture Mechanics Analysis of Fatigue Performance

Because PJP welds may arise in a variety of situations, it may not always be possible to refer to standard S-N curves to predict their performance. As such, a linear-elastic model was developed to help predict their performance in a variety of cases. The general theory behind fracture mechanics is explained in Section 2.2.2. The PJP butt welds are essentially the same as a standard center-cracked tension (CCT) specimen (Figure 4.1). The CCT specimens have a well-defined equation for the shape factor Y [19]:

$$Y = \sqrt{\sec\left(\frac{\pi a}{2W}\right)}\left(1 - 0.025\left(\frac{a}{W}\right)^2 + 0.06\left(\frac{a}{W}\right)^4\right) \tag{4.1}$$

where $2a$ is the total crack width and $2W$ is the total sample width. For PJP welds, $2W$ is equal to the thickness of the plates and $2a$ is equal to the depth of the unwelded portion of the joint. In practice, the polynomial term is negligible until the crack depth is more than 90% the thickness of the plates, so it is omitted for simplicity [37]:

$$Y = \sqrt{\sec\left(\frac{\pi a}{2W}\right)} \tag{4.2}$$

Figure 4.2 shows how the difference between Equations 4.1 and 4.2 is negligible in all cases for the PJP weld samples.

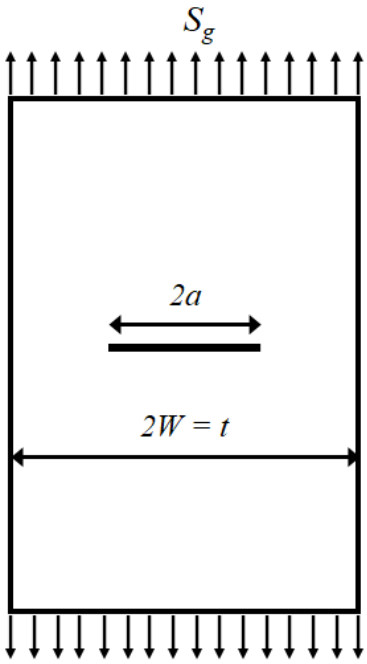

Figure 4.1: A typical center-cracked tension (CCT) specimen, which has the same geometry as the PJP butt weld samples. There is a slight difference in nomenclature, where the "width" $2W$ for CCT specimen is considered the thickness t in the PJP samples.

4.1 Critical Degree of Penetration

With PJP welds, it is much more convenient to consider the net section stress, σ_n, as opposed to the gross section stress σ which is normally used in calculating the stress intensity factor (SIF) K. By relating the SIF based on net section stress and the degree of penetration, an interesting behaviour appears. The consideration of net section stress instead of gross stress creates a sort of dueling effect between the gross stress σ and the

shape factor Y in the SIF equation:

$$K = \sigma Y \sqrt{\pi a} \tag{4.3}$$

If the net section stress σ_n is kept constant, *increasing* the degree of penetration ρ will *decrease* the shape factor Y and the $\sqrt{\pi a}$ terms, as the size of the flaw $2a$ is reduced (Y also increases with a). The relationship between a and ρ is shown below, which explains this:

$$a = \frac{t}{2}(1 - \rho) \tag{4.4}$$

Conversely, the gross section stress σ will *increase* with the degree of penetration, as an increased degree of penetration means a larger area for the net section stress to be applied on. This means a higher total load is applied and thus causes an increase in gross stress. This relationship between the gross stress, net section stress and the degree of penetration is simple:

$$\sigma = \sigma_n \cdot \rho \tag{4.5}$$

Putting Equations 4.3, 4.4, 4.2 and 4.5 together, an equation to determine the SIF K can be derived which depends only on the degree of penetration ρ, the net section stress σ_n and the plate thickness t:

$$K = \sigma_n \rho \sqrt{\sec\left(\frac{\pi}{2}(1 - \rho)\right)} \sqrt{\frac{\pi t}{2}(1 - \rho)} \tag{4.6}$$

The relationship between the degree of penetration and the SIF for a constant thickness and net section stress can be seen graphically in Figure 4.2.

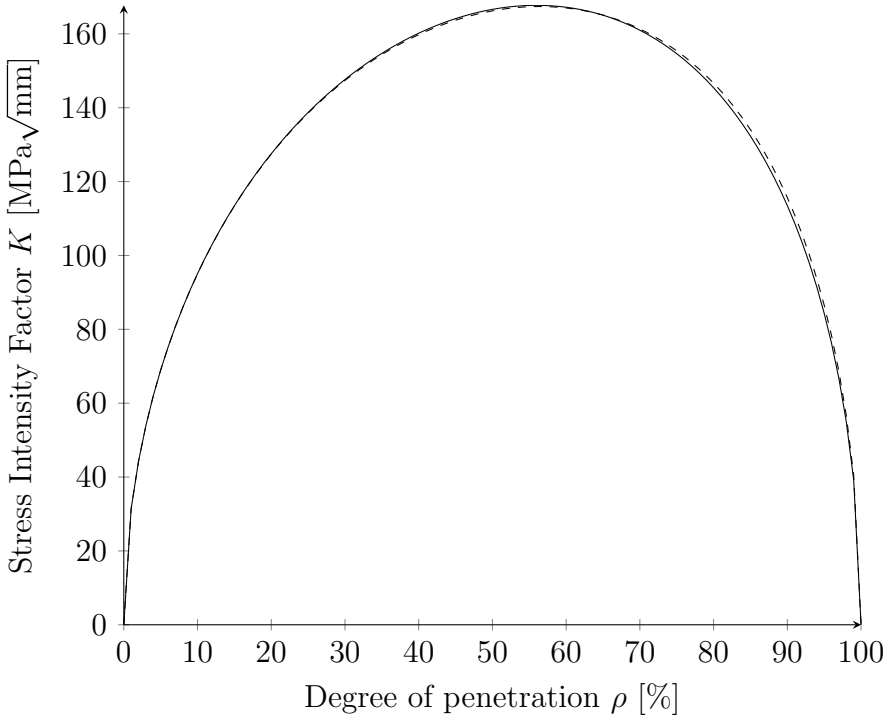

Figure 4.2: Influence of degree of penetration ρ on the stress intensity factor K, under constant **net section** stress $\sigma_n = 100$ MPa and thickness $t = 10$ mm. The dashed line shows the same relationship calculated using the full formula for Y, which is practically the same.

The dueling effect between σ and a is clearly seen in Figure 4.2. It is most evident at the two extremes, where $K = 0$ for both $\rho = 0\%$ and $\rho = 100\%$. When $\rho = 0\%$, this means that there is no weld filler metal at all, and thus the net sectional area is zero. There is thus no load through the sample and the gross stress σ is also zero. When $\rho = 100\%$, the full thickness of the plate is welded and there is no crack. Thus, $a = 0$ and the $\sqrt{\pi a}$ term goes to zero. What happens in-between the two extremes is more interesting. As ρ increases, initially σ governs the SIF equation, rapidly increasing until a maximum is reached, at which point the crack length effect dominates and the SIF reduces to zero.

The location of the maximum value can be calculated by taking the derivative of Equation 4.6 with respect to the degree of penetration ρ.

$$\frac{dK}{d\rho} = \sigma_n \sqrt{\frac{\pi t}{2} \sec\left(\frac{\pi}{2}(1-\rho)\right)} \left[\sqrt{1-\rho}\left(1 - \frac{\pi\rho}{4}\tan\left(\frac{\pi}{2}(1-\rho)\right)\right) - \frac{\rho}{2\sqrt{1-\rho}}\right] \tag{4.7}$$

Setting the equation equal to 0 to find the maximum, and dividing by $\sigma_n\sqrt{\frac{\pi t}{2}}$:

$$0 = \sqrt{\sec\left(\frac{\pi}{2}(1-\rho)\right)} \left[\sqrt{1-\rho}\left(1 - \frac{\pi\rho}{4}\tan\left(\frac{\pi}{2}(1-\rho)\right)\right) - \frac{\rho}{2\sqrt{1-\rho}}\right] \tag{4.8}$$

It becomes clear that the value of ρ causing the highest SIF is independent of the thickness and the net section stress. Using a numerical solver, it was found that the maximum SIF occurs at $\rho \approx 56\%$. This is of great practical importance. As described previously, the range of evaluated nominal degrees of penetration was from 42% to 84%. With the maximum SIF occurring at 56%, the range of studied samples was therefore consistently near the maximum. In fact, when considering the actual measured penetration, the $\rho = 75\%$ samples had most the deviation from the maximum SIF, but this remained less than 10% deviation, hardly a large difference when considering typical scatter in fatigue data. It could thus be predicted from this model that because the stress is defined over the net sectional area, the degree of penetration has relatively little influence on the SIF in practical applications of PJP welds.

4.2 Applicability of LEFM

A significant assumption with LEFM is that the material behaviour remains linear-elastic even at the highest loads. In reality, yielding will occur in the metal and some stress redistribution will occur in the plastic zone. This is discussed in further detail in Section 2.2.2. As shown in Equation 2.11, the size of the plastic zone is defined by the SIF and the yield

stress:

$$r_p = \frac{1}{3\pi}\left(\frac{K}{\sigma_y}\right)^2 \tag{4.9}$$

The size of the plastic zone calculated using this equation assumes a plane strain condition, which is expected to consistently be the case as the weld length will reasonably always be longer than the thickness of the plate. In alloys that strain-harden significantly, it may be more accurate to consider the *flow strength*, taken as the average between the yield stress and ultimate stress [37] and indicated as σ_o.

A quick verification for the validity of LEFM in the PJP welds was performed. The SIF was calculated assuming:

- Plate thickness of 19 mm, the thickest samples examined;
- A flow stress of 165 MPa, the average of yield (95 MPa) and ultimate strength (240 MPa) for the 5356 alloy per CSA S157;
- Net section stress of 190 MPa, corresponding to the maximum stress for fatigue loading with a stress range of $\Delta\sigma = 95\,\text{MPa}$ at a stress ratio of $R = 0.5$.

Entering these parameters in Equation 4.6 yields a stress intensity factor of $K = 439\,\text{MPa}\sqrt{\text{mm}}$. Calculating the plastic zone size with Equation 4.9 finds a plastic radius of 0.75 mm, which is much smaller than either the crack or the weld size. It was thus deemed appropriate to use linear-elastic fracture mechanics.

4.3 Fatigue Life Prediction with LEFM

With the previous calculations performed for the stress intensity factor, the Paris-Erdogan equation could then be applied to predict the fatigue life of the welded components. As a

reminder, the Paris-Erdogan Equation takes the following form:

$$\frac{\mathrm{d}a}{\mathrm{d}N} = C_0(\Delta K)^m \tag{4.10}$$

where C_0 and m are material constants defining the crack growth rate.

In general, there is little difference between aluminum alloys for C_0 and m and high scatter in crack growth tests suggests that no specific consideration for the alloy is required, even more so in welds where the notching effect is particularly pronounced [38]. It is somewhat common in aluminum fatigue design to use a multi-linear fatigue crack growth relationship, often attributed to crack closure phenomena appearing from an oxide layer formation or plasticity depending on the load magnitude. There is a breadth of crack growth rate data in the literature, with a few different examples shown in Figure 4.3.

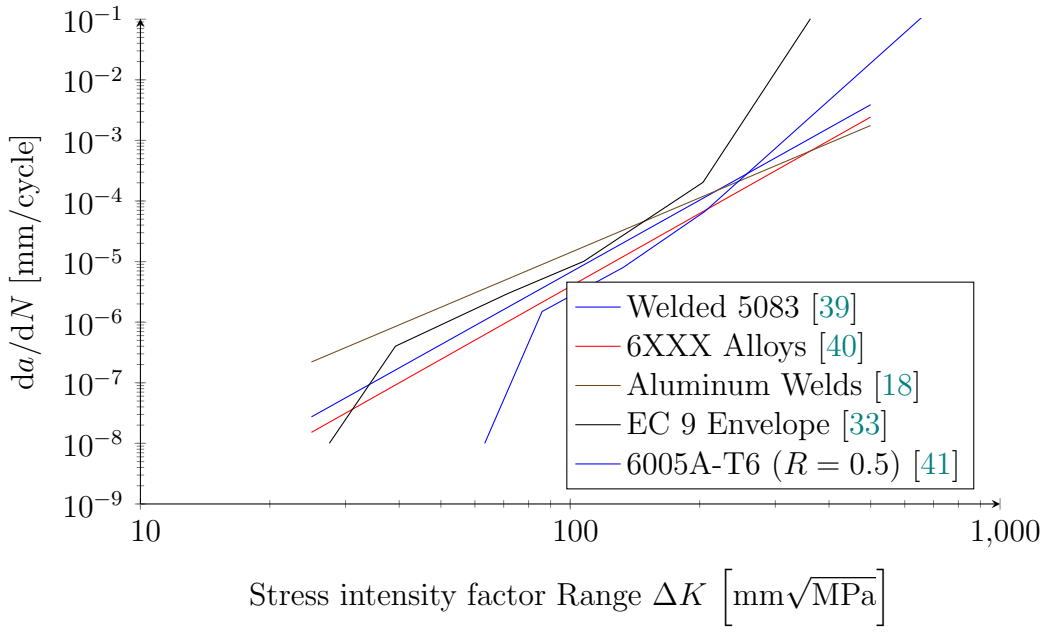

Figure 4.3: Fatigue crack growth rate data from literature on aluminum welds.

It was decided to use C_0 and m values on the upper range of the literature, which were used in the work of Ranjan et al. [39]. This was decided because welds are typically

expected to have high levels of residual stresses and because it was desired to use closure-free crack growth data (discussed below). The exact values used in the LEFM model are shown in Table 4.1.

Table 4.1: Parameters used in LEFM analysis.

Parameter	Value	Units	Ref.
σ_y	95	MPa	[9]
σ_u	240	MPa	[9]
σ_o	165	MPa	[42]
C	7.97×10^{-14}	(MPa, mm)	[39]
m	4	(MPa, mm)	[39]
ΔK_{th}	$56.7 - 72.3R \geq 21$	MPa$\sqrt{\text{mm}}$	[18]

To find the fatigue life, Equation 4.10 is integrated over a crack size range, as explained in Section 2.2.2. This takes the form:

$$N_f = \int_{a_o}^{a_f} \frac{\mathrm{d}a}{C_0 \Delta K^m} \tag{4.11}$$

where a_o is the size of the initial crack, equal to $\frac{t}{2}(1-\rho_o)$. a_f is the crack to cause failure, which for aluminum alloys is essentially always the ductile fracture criterion:

$$a_f = \frac{t}{2}\left(1 - \frac{\rho_o \Delta\sigma_n}{\sigma_u(1-R)}\right) \tag{4.12}$$

where ρ_o is the initial degree of penetration.

The equation was modified to consider two effects in particular: plasticity-induced crack closure and the threshold SIF range:

$$N_f = \int_{a_0}^{a_f} \frac{\mathrm{d}a}{C_0\left(\Delta K_{\text{eff}}^m - \Delta K_{\text{th}}^m\right)} \tag{4.13}$$

The derivations behind ΔK_{eff} and the $\Delta K_{\text{eff}}^m - \Delta K_{\text{th}}^m$ terms are explained in the next two sections.

4.4 Crack Closure

In general, the crack growth rate varies with the stress ratio R. A common model to explain this behaviour is crack closure. This phenomenon takes place when the sample is fully loaded in tension and plastic deformation occurs at the crack tip. The plastic deformations do not fully revert when the sample is unloaded. This lingering deformation causes a closure effect, where the crack remains closed even under tensile loading until the crack opening stress σ_{op}. Its equivalent stress intensity factor, K_{op}, is also considered and may be more convenient to use. To account for this, an effective SIF range, ΔK_{eff}, is defined:

$$\Delta K_{\text{eff}} = K_{\max} - K_{op} = U \times \Delta K \tag{4.14}$$

where U is a factor relating ΔK to ΔK_{eff}. The value of ΔK_{eff} is then used in the Paris-Erdogan equation (Equation 4.10) to better predict the fatigue crack growth rate.

There are many published formulas and methods to estimate the value of U, ranging from elaborate strip-yield models to simple linear relationships. In this case, it was decided to use Newman's crack opening stress equation [42], modified by McClung [43] to consider the SIF instead of stress. This has been found to agree well with aluminum welds [44]. While Newman's model is based on the ratio $\sigma_{\max}/\sigma_o$ corresponding to stresses, McClung suggests using $K_{\max}/K_o$, with the SIFs defined as such:

$$K_{\max} = \sigma_{\max} Y \sqrt{\pi a} \text{ and } K_o = \sigma_o \sqrt{\pi a} \tag{4.15}$$

Importantly, the shape factor Y is not included when calculating K_o, which allows for the consideration of geometry in the crack closure equation.

Newman's equation consists of a fitted curve that considers the effects of yield strength, strain hardening, triaxiality, maximum stress and stress ratio. In plane strain conditions,

with $R > 0$ and as modified by McClung, it takes the following form:

$$U = \frac{1 - K_{op}/K_{\max}}{1 - R} \tag{4.16}$$

$$K_{op}/K_{\max} = C_0 + C_1 R + C_2 R^2 + C_3 R^3 \tag{4.17}$$

where:

$$C_0 = 0.255 \times \left[\cos\left(\frac{\pi}{2}\frac{K_{\max}}{K_o}\right)\right]^{1/3} \tag{4.18}$$

$$C_1 = 0.202 \times \frac{K_{\max}}{K_o} \tag{4.19}$$

$$C_2 = 1 - C_0 - C_1 - C_3 \tag{4.20}$$

$$C_3 = 2C_0 + C_1 - 1 \tag{4.21}$$

This equation was thus used to model the crack closure phenomenon in the PJP welds.

4.5 Threshold SIF Range

As shown in Figure 2.6, there is a threshold value of ΔK under which crack growth is not expected to occur. As the SIF range decreases, the crack growth rate rapidly goes to zero near ΔK_{th}. The transition from region A (no crack growth) to region B (crack growth per Eq. 4.10) was implemented in the model as such [44]:

$$\frac{\mathrm{d}a}{\mathrm{d}N} = C_0(\Delta K_{\text{eff}}^m - \Delta K_{\text{th}}^m) \tag{4.22}$$

With the parameters indicated in Table 4.1, the crack growth rate curve used in the analysis was generated and is shown in Figure 4.4.

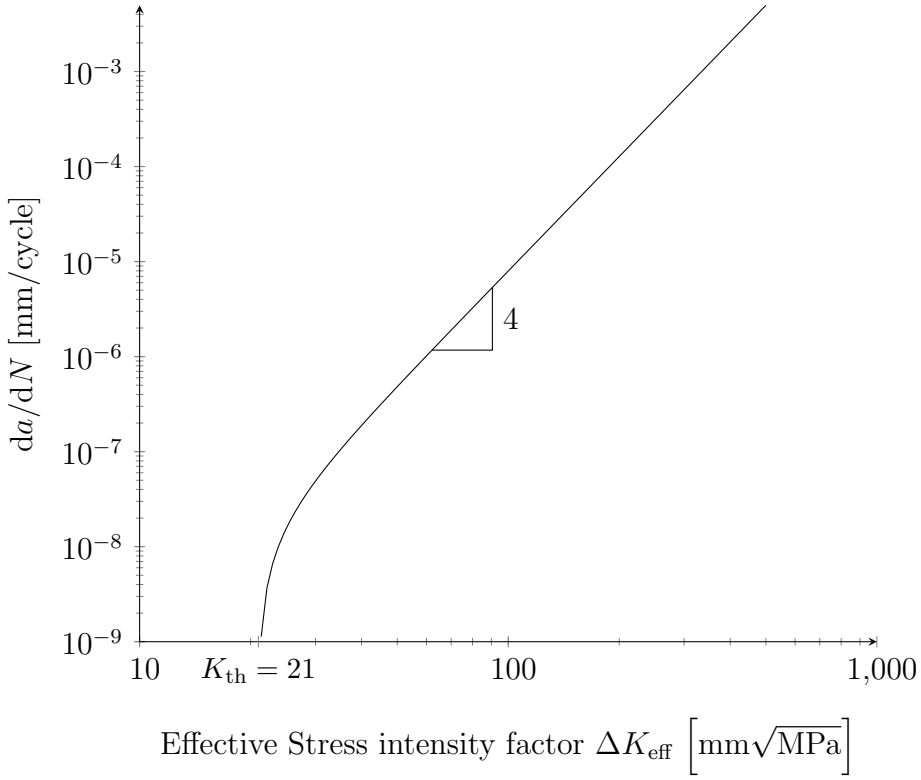

Figure 4.4: Fatigue crack growth rate curve used in the LEFM analysis.

4.6 Revisiting the Critical Degree of Penetration

As mentioned earlier in Section 4.1, the definition of stress across the net weld cross-section rather than the gross cross-section creates some interesting trends. Given that the degree of penetration causing the highest SIF was found to be a constant at $\rho = 56\%$, it was suspected that a similar effect would be seen in fatigue life because the SIF range ΔK governs fatigue crack growth. An analysis analogous to the SIF study was thus performed, where the initial degree of penetration was varied with every other parameter staying constant, to observe the impact on fatigue life. After performing numerical integration on Equation 4.13, the results were graphed and are shown in Figure 4.5.

Following the same methodology as was used with the critical stress intensity factor,

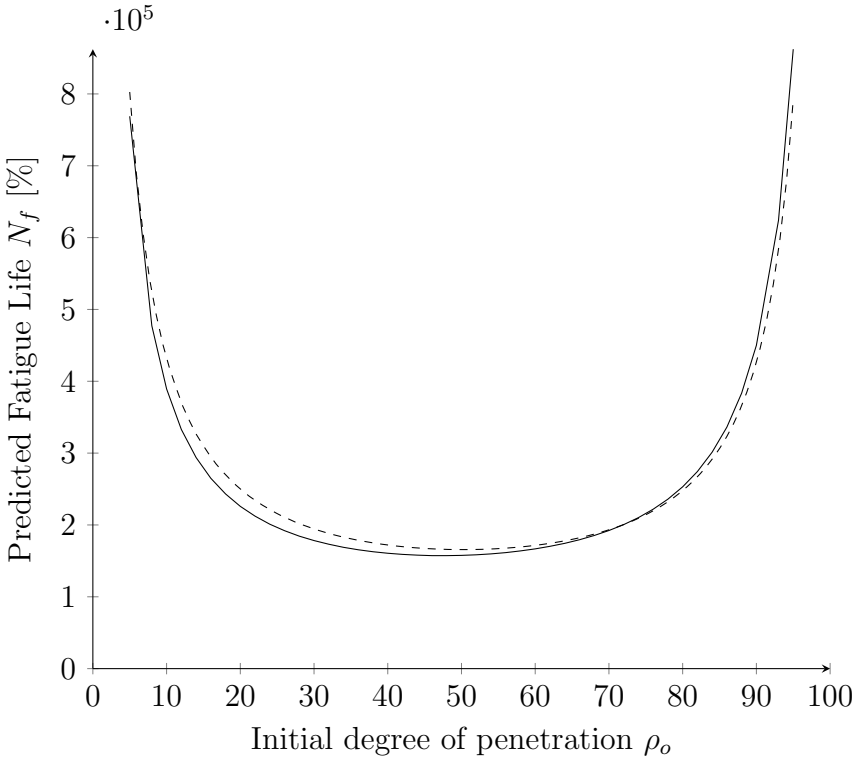

Figure 4.5: Influence of degree of penetration ρ on the fatigue life N_f, under net section stress range $\Delta\sigma_n = 50\,\text{MPa}$ and $R = 0.5$ on a 10 mm plate sample. In dashed line, the approximation from the LEFM model.

the derivative of N_f with respect to ρ_o, the initial degree of penetration, can be taken to find the critical value of ρ_o. The goal is thus to minimize Equation 4.13. Substituting Equations 4.3, 4.5 and 4.14 into Equation 4.13:

$$\frac{\mathrm{d}N_f}{\mathrm{d}\rho_o} = \frac{\mathrm{d}}{\mathrm{d}\rho_o}\int_{a_o}^{a_f} \frac{\mathrm{d}a}{C_0\left[\left(U(a)\times\rho_o\sigma_n\sqrt{\sec\left(\frac{\pi a}{2t}\right)}\sqrt{\pi a}\right)^m - \Delta K_{\text{th}}^m\right]} \tag{4.23}$$

From Equation 4.4, a_o can also be expressed as a function of ρ_o. Similarly a_f can be expressed as function of ρ_o by Equation 4.12. The final equation thus takes the form:

$$\frac{\mathrm{d}N_f}{\mathrm{d}\rho_o} = \frac{\mathrm{d}}{\mathrm{d}\rho_o} \int_{\frac{t}{2}(1-\rho_o)}^{\frac{t}{2}\left(1-\frac{\rho_o \Delta\sigma_n}{\sigma_u(1-R)}\right)} \frac{\mathrm{d}a}{C_0 \left[\left(U(a) \times \rho_o \sigma_n \sqrt{\sec\left(\frac{\pi a}{2t}\right)}\sqrt{\pi a}\right)^m - \Delta K_{\mathrm{th}}^m\right]} \tag{4.24}$$

Unfortunately, there is no closed-form solution for this integral. The basic Paris-Erdogan equation was thus used as an estimate. In general, U changes very little with ρ and the effects of ΔK_{th} are negligible in all but the smallest loads and cracks. The principal source of error is in the geometry factor, which increases rapidly when $\rho < 0.1$. To approximate its effect, Y was taken as a constant calculated by using $0.8\rho_o$. The 0.8 factor was selected to consider the rising value of Y as the crack grows and was found to provide a close match between the simplified and complete integrals. Since the crack growth rate is smallest initially, this is a relatively good approximation. The life was thus estimated by integrating Equation 4.11:

$$N_f = \frac{a_f^{1-m/2} - a_o^{1-m/2}}{C_0 \left(Y \Delta\sigma \sqrt{\pi}\right)^m (1 - m/2)} \tag{4.25}$$

and substituting Equations 4.4, 4.5 and 4.12:

$$N_f = \frac{\left(\frac{t}{2}\left(1 - \frac{\rho_o \Delta\sigma_n}{\sigma_u(1-R)}\right)\right)^{1-m/2} - \left(\frac{t}{2}(1-\rho_o)\right)^{1-m/2}}{C_0 \left(\sqrt{\sec\left(\frac{\pi}{2}(1-0.8\rho_o)\right)}\rho_o \Delta\sigma_n \sqrt{\pi}\right)^m (1 - m/2)} \tag{4.26}$$

This equation is plotted in Figure 4.5. Taking the derivative with respect to ρ_o and setting it equal to zero:

$$\begin{aligned} 0 = & \frac{\left(\frac{t}{2}\right)^{1-m/2}}{C_0\left(\Delta\sigma_n\sqrt{\pi}\right)^m(1-m/2)} \\ & \times \frac{1}{\rho_o^m\left(\sec\frac{\pi}{2}(1-0.8\rho_o)\right)}\left[\frac{1-\frac{m}{2}}{(1-\rho_o)^{\frac{m}{2}}} - \frac{B\left(1-\frac{m}{2}\right)}{(1-B\rho_o)^{\frac{m}{2}}}\right. \\ & \left. + \left(\frac{0.8\pi m}{4}\tan\left(\frac{\pi}{2}(1-0.8\rho_o)\right) - \frac{m}{\rho_o}\right)\left((1-B\rho_o)^{1-m/2} - (1-\rho_o)^{1-m/2}\right)\right] \end{aligned} \tag{4.27}$$

where $B = \frac{\Delta\sigma_n}{\sigma_u(1-R)} = \sigma_{n,\max}/\sigma_u$. Dividing out the first two terms, the following remains:

$$\begin{aligned} 0 = & \frac{1-\frac{m}{2}}{(1-\rho_o)^{\frac{m}{2}}} - \frac{B\left(1-\frac{m}{2}\right)}{(1-B\rho_o)^{\frac{m}{2}}} \\ & + \left(\frac{0.8\pi m}{4}\tan\left(\frac{\pi}{2}(1-0.8\rho_o)\right) - \frac{m}{\rho_o}\right)\left((1-B\rho_o)^{1-m/2} - (1-\rho_o)^{1-m/2}\right) \end{aligned} \tag{4.28}$$

This shows that the critical value of ρ_o minimizing fatigue life is dependent on the slope m in the Paris-Erdogan equation, the maximum stress, and the ultimate strength of the material. As the slope m is presumed to remain constant for all aluminum alloys, replacing it with $m = 4$ simplifies the equation:

$$0 = \frac{B}{(1-B\rho_o)^2} - \frac{1}{(1-\rho_o)^2} + \left(\frac{1}{1-B\rho_o} - \frac{1}{1-\rho_o}\right)\left(0.8\pi\tan\left(\frac{\pi}{2}(1-0.8\rho_o)\right) - 4/\rho_o\right) \tag{4.29}$$

By solving numerically for ρ_o as a function of $B = \sigma_{n,\max}/\sigma_u$, it becomes apparent that the maximum stress has relatively little effect on ρ_c, the critical value of ρ_o. As shown in Figure 4.6, over the entire range of B, ρ_c spans only a 20% range, with the average at $\rho_c = 60\%$.

A second interesting component is seen in Figure 4.5. The N_f – ρ_o curve has a wide U shape, with relatively little change occurring until extreme values of ρ_o are reached, which

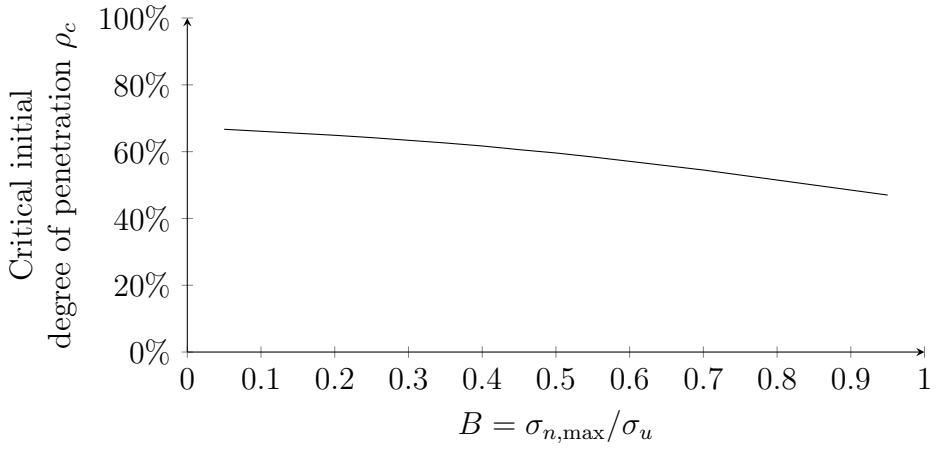

Figure 4.6: The critical degree of penetration for minimum fatigue life as a function of the ratio of the maximum net section stress and the ultimate strength.

are unlikely to be seen in actual design. The initial degree of penetration ρ_o can vary by up to 16% each way from its minimum before the predicted fatigue life is over 10% of the minimum fatigue life. If a practical range of ρ_c is estimated as 40% to 80%, using the minimum fatigue life will at most under-estimate the fatigue life by 25%, which is small given that these are usually compared by orders of magnitude.

Chapter 5

Finite Element Analysis Model

To supplement hand calculations, a two-dimensional finite element analysis (FEA) model was created using the Dassault Systèmes ABAQUS software. A script developed in Python was used to automatically generate geometry, assign material properties, generate a mesh and run the analysis. This allowed any parametric study to take place and ensured that all model parameters remained the same unless they were explicitly changed. Dimensions of the model are shown in Figure 5.1.

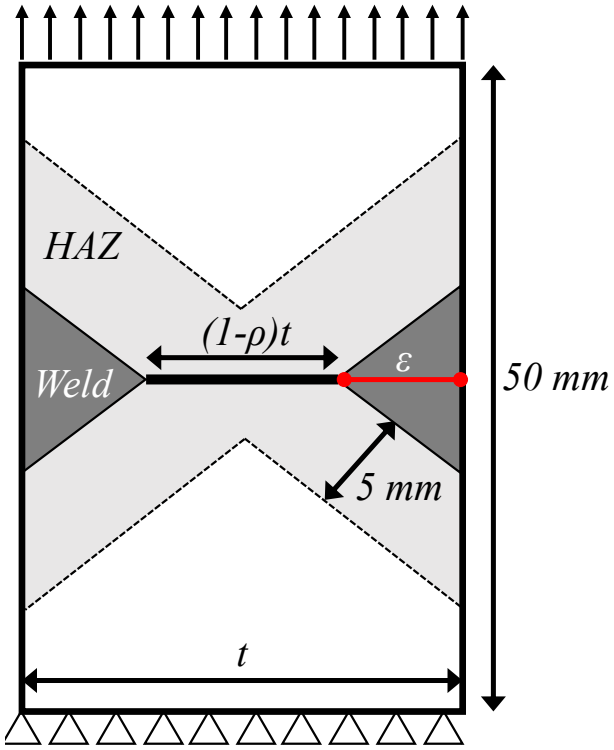

Figure 5.1: Diagram of the FEA model used in the analysis. In red is the virtual extensometer used to measure the constraint from the unloaded portion of the plate (only used in static tests).

5.1 Static Loading

Two principal observation goals were set for the finite element model:

- The effect of triaxiality and lateral restraint and the impact by degree of penetration. A virtual extensometer was applied accross the weld to measure strains perpendicular to the loading axis.
- The impact of varying material strength. While the model cannot be used to detect failure load, a significant component of the stress-strain curve can be obtained and provide insight on this effect.

5.1.1 Limitations of the FEA Model

Perhaps the greatest limitation with simulating tension tests using the finite element method is the high complexity of modeling ductile fracture. While some models do exist to consider ductile fracture, they are normally rather complicated and applicable to very specific scenarios. It should thus be noted here that the FEA model in this study was **not** expected to simulate testing until failure. Even without simulating failure, the FEA model could still provide extremely valuable information.

Another limitation of the model is that by remaining in two dimensions, triaxiality cannot be fully considered. The out of plane Poisson effects cannot be fully modeled because generally, the ends of the welds are in a state of plane stress (since no material remains to prevent strain), and the middle is generally in a state of plane strain. It was assumed in this model that a plane strain condition existed across the whole length of the weld, as the plane stress condition would only be over a small proportion of the weld near the ends.

5.1.2 Material Properties

Because structural aluminum alloys generally have high ductility, a purely linear-elastic model would not be adequate to represent their behaviour in static loading. In particular, aluminum welds typically have two different alloys and a heat affected zone, all of which have different mechanical properties. For example, there is a large difference in the strain hardening characteristics of the different metals used in welding the 6000 series alloys with 5000 series weld filler metal, as 5000 series harden much more than 6000 series alloys.

To account for this, a trilinear plasticity model was integrated into the analysis. This consisted of the yield point, an intermediate point to account for strain hardening profiles, and the ultimate point. Three different materials were defined in the model: the 5356 weld filler metal, the heat-affected 6061 base metal, and the fully tempered 6061-T6 alloy. This simplified model allowed for the accounting of different strain-hardening profiles and varying yield strengths.

For the 6061-T6 base metal, the yield strength, ultimate strength and ultimate strain were taken as the average of the measured values provided in fabricator-supplied mill test reports. For both the base metal and the HAZ properties, the intermediate point was established at $\varepsilon_u = \varepsilon_u/10$ and $\sigma = (\sigma_y + \sigma_u)/2$.

For the heat affected zone, the yield and ultimate strengths were estimated from micro-hardness measurements, which are described in further detail in Section 6.2. Using a bank of static test data on aluminum alloys from a previous project at the University of Waterloo, correlations between hardness and strength were determined:

$$\sigma_y = 3.15 \times HV - 113 \tag{5.1}$$

$$\sigma_u = 2.62 \times HV - 5.8 \tag{5.2}$$

These relationships were determined using samples with hardnesses varying between $HV = 60$ and $HV = 120$ and should only be considered valid within this range. These correlations were then used with a hardness value of $HV = 75$. This method is consistent with previous validated models in literature [44]. The HAZ was taken as the area within 5 mm of the weld fusion zone – this distance corresponds to what was observed during the macro-hardness testing.

Although the hardness of the weld metal was also measured in the micro-hardness tests, lack of data for the 5356 alloy precluded using the hardness data to estimate strength. Values measured in previous literature were thus used [45] in the model. The intermediate point was established at $\varepsilon = \varepsilon_u/4$ and $\sigma = (\sigma_y + \sigma_u)/2$. The difference in the strain location for the intermediate point compared with the 6061 alloy reflects the different strain hardening profile.

The three stress-strain curves used in the FEA model are shown in Figure 5.2. All three materials were set to have an elastic modulus of $E = 70\,000$ MPa and a Poisson ratio $\nu = 0.33$.

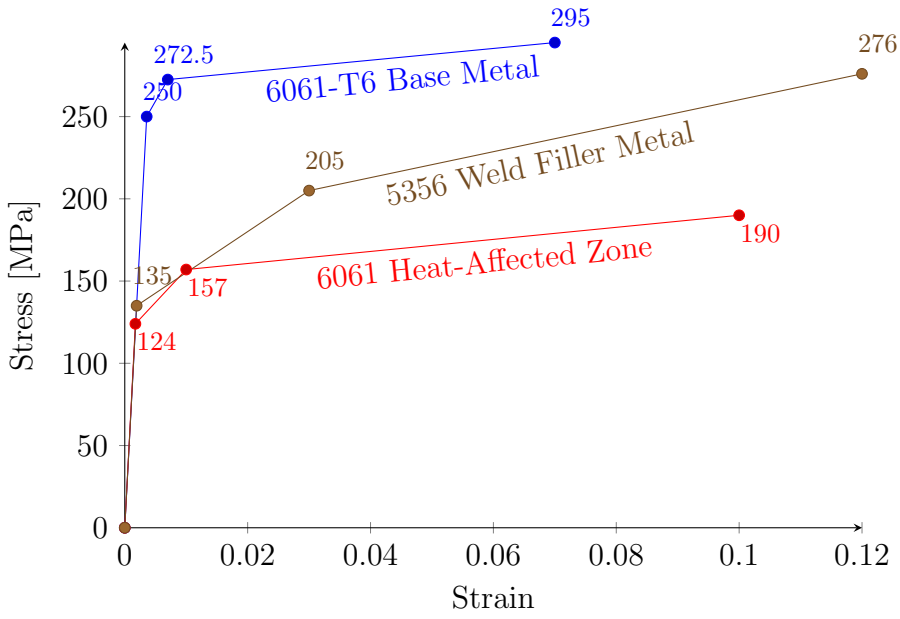

Figure 5.2: Trilinear stress-strain curves for the three materials considered in the FEA model. The 6061 alloy has two curves, the weaker one specific to the heat affected zone.

5.2 Fatigue Performance Predictions

While the directly calculated LEFM analysis is a powerful tool to estimate the fatigue performance of the PJP welds, it is somewhat limited in application due to the difficulty in finding the shape factor Y for complicated shapes. An example would be with flare bevel welds, whose geometry does not resemble any published solution for the SIF. A J-integral approach was thus used to find the SIF at the crack tips for various configurations of the butt welds. In particular, cases where the crack is not centered do not have published closed-form solutions for the SIF, a situation observed on some samples due to misalignment defects or differing weld bead size on each side of the plate. This model was generated to be versatile, with the intention of extending its capabilities to apply to flare bevel welds as part of the project described in Chapter 7.

The basic principle behind the J-integral is the use of a contour integral over the strain

field near a crack tip to find the amount of energy required to extend a crack, known as the strain energy release rate [46]. This is useful as it provides an analogue to the stress intensity factor which can directly consider the effects of plasticity. When a linear-elastic material behaviour is assumed, an exact relationship between J and K exists:

$$J = K^2 \times \left(\frac{1 - \nu^2}{E} \right) \tag{5.3}$$

in the plane strain condition (the $1 - \nu^2$ term disappears in plane stress).

Modern FEA software such as ABAQUS include advanced algorithms which perform fast and efficient calculation of the J-integral on any domain or contour, under any loading. Using the relationship shown in Equation 5.3 thus allows direct evaluation of the SIF using the finite element method of essentially any geometry and loading.

Another property of the J-integral is its path independence. In linear-elastic materials and to some extent in elastic-plastic materials, the J-integral has complete path independence [46]. Regardless of the contour chosen for the integration, the final value will always be the same. In a finite element model where numerical inaccuracies are unavoidable, this property of the J-integral is extremely valuable to verify convergence of the integral over multiple paths, as differences between contour values are directly indicative of errors in the model.

5.2.1 Material Properties

It is crucial to note that the FEA model to evaluate the J-integral is based on linear-elastic material behaviour. As such, the only two material properties input in the model were the modulus of elasticity $E = 70\,000\,\text{MPa}$ and Poisson's ratio $\nu = 0.33$. The weld and HAZ were not considered in the model, their elasticity and Poisson ratio assumed to be the same as for the base aluminum.

5.2.2 Comparison with Published Solution

To first confirm the adequacy of the model, it was compared to the published solution (Equation 4.1) for a centre-cracked tension sample as shown in Figure 4.1. The results are shown in Figure 5.3 to match almost exactly, which confirms the adequacy of the J-integral to find the SIF.

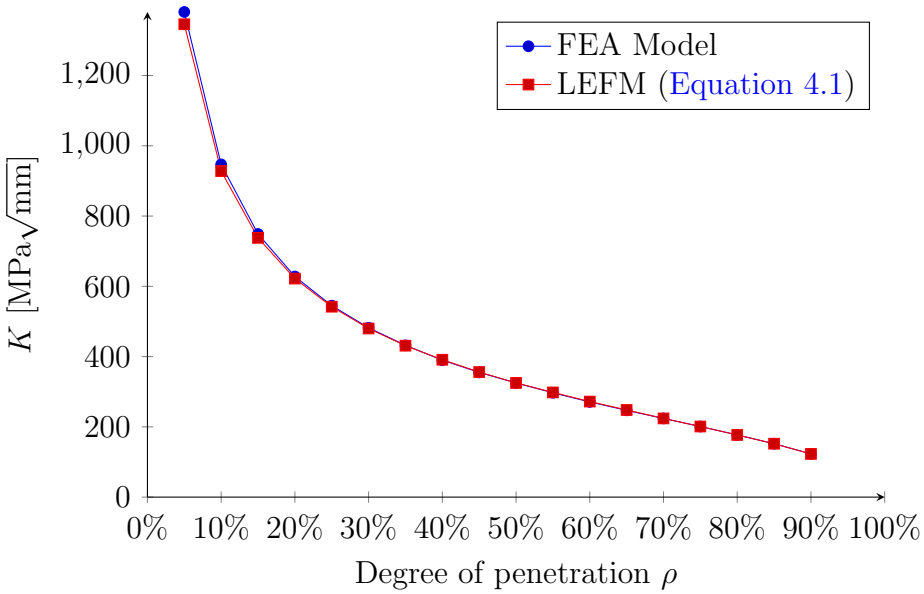

Figure 5.3: Comparison of the FEA model and the LEFM analysis for a centre-cracked tension sample with $\sigma = 100\,\text{MPa}$ and $t = 9.5\,\text{mm}$.

5.2.3 Defining and Modeling Asymmetry

Once the model was validated against LEFM, the next step undertaken was to model asymmetries in the samples. Two sources of asymmetry were considered. First, the angular misalignment (from warping in the welds) was directly considered in the model by the angular misalignment factor k_φ. The parameters used to describe the angular misalignment are shown in Figure 5.4.

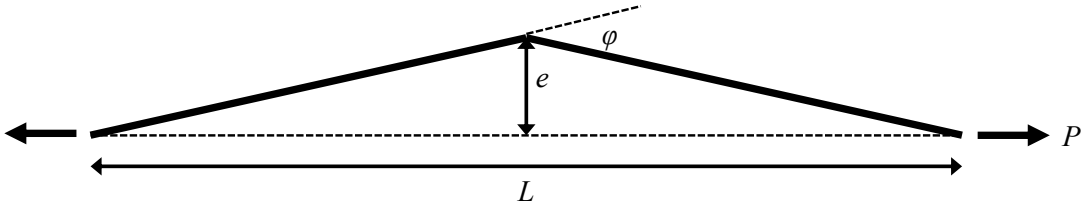

Figure 5.4: Dimensions considered when defining angular misalignment. The weld axis is going into the page, located at the bend.

It should be noted that the length of the sample has a large influence in the bending stress generated from angular misalignment. The bending moment generated from the angular misalignment can be calculated as such:

$$M = P \times e \tag{5.4}$$

$$= P \times \frac{L}{2} \tan\varphi \approx \frac{L}{2}\varphi \tag{5.5}$$

Where L is the sample length and φ is the misalignment angle (in radians), shown in Figure 5.4. The moment is thus clearly dependent on the sample length. This is further complicated when considering second order effects, as the tensile load flattens the sample and thereby decreases the value of e. To consider these second order effects, a theoretical formula was used to find a factor k_φ relating the normal stress and the bending stress for a certain angle [18]:

$$k_\varphi = \frac{3\varphi L}{2t} \times \frac{\tanh\beta}{\beta} \tag{5.6}$$

where:

$$\beta = \frac{L}{t}\sqrt{\frac{3\sigma}{E}} \tag{5.7}$$

To directly compare analysis results with experimental results, a length of 400 mm was assumed when calculating φ; this was the length of the tested samples less the depth of the

wedges of the loading frame. This was deemed conservative when compared with design as most welded samples will be much longer than 400 mm, at which point the $\tanh \beta/\beta$ term quickly tends to zero.

The second source of asymmetry considered was in the crack location, as shown in Figure 5.5. It was suspected that under the eccentric loading, a crack would initially grow faster on one side than on the other. At that point, two counter-acting effects were considered. First, as the crack grows more to one side, that side loses stiffness the amount of load carried by that side is reduced, which slows down the crack growth on that side. Second however, as the crack grows, it becomes closer to the surface and thus the local SIF would be expected to increase, increasing crack growth on that side. To represent the asymmetry in the crack location, a dimensionless asymmetry parameter was defined:

$$\omega = 1 - \frac{w_1}{w_2}, w_1 \leq w_2 \tag{5.8}$$

where w_1 and w_2 are shown in Figure 5.5. When $\omega = 1$, the crack reaches the surface on one side, and when $\omega = 0$, the crack's centreline corresponds to the plate's mid-thickness line.

With the parameters defined, the model was run over a large range of values of ρ and ω, first considering a purely axial load, and followed by a purely bending load. From the results, values of Y were extracted (using Equation 5.3 and Equation 4.3) and tabulated as a function of ρ and ω. The J-integral analyses were run over a range of thicknesses to confirm that the value of Y is independent of thickness. The tables were then used as a mapping to find the SIF over the fatigue life of the sample during numerical integration. The tabulated Y values are shown in Appendix A. Because the shape factor was defined as a function of dimensionless parameters ρ and ω and under a uniform remote stress, the calculated shape factor values implicitly include effects such as the section properties changing as the crack grows.

From these, the numerical integration process proceeded, essentially using the same method as Equation 4.13. Using the principle of superposition, the stress intensity factors

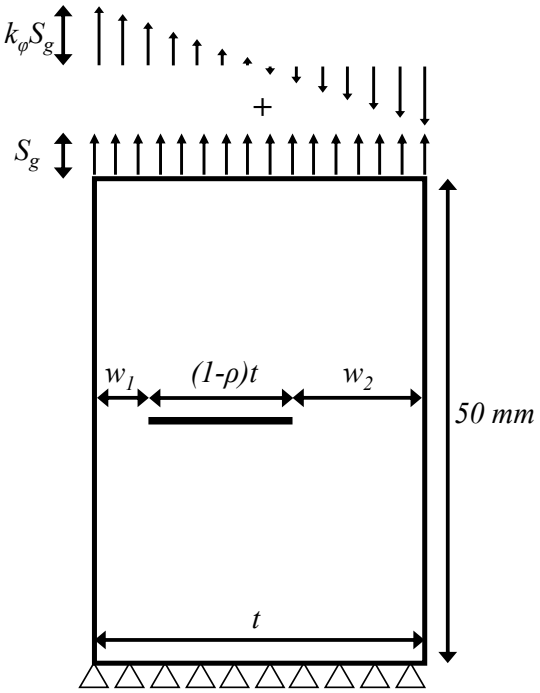

Figure 5.5: Definition of loading and dimension parameters for the asymmetrical FEA model.

from axial and bending loads were added together:

$$\Delta K = \Delta K_{\text{axial}} + \Delta K_{\text{bending}} \tag{5.9}$$

A particular consideration when calculating the SIF from bending is that the value of k_φ varies with the applied stress due to second order effects, as shown in Equation 5.6. To account for this, the SIF for bending was calculated using a modified stress range:

$$\Delta\sigma_{\text{bending}} = (k_{\varphi,\max}\sigma_{\max} - k_{\varphi,\min}\sigma_{\min}) \tag{5.10}$$

$$\tag{5.11}$$

where $k_{\varphi,\max}$ and $k_{\varphi,\min}$ are calculated with Equation 5.6 by replacing σ with $\sigma_{\max}$ and $\sigma_{\min}$, respectively. It should be noted that because the bending stress range was no longer

directly proportional to the axial load, a different stress ratio would be calculated. This affected the crack closure model as it is dependent on the R ratio. However, it was decided to keep R as the value specified in axial loading, since the SIF from bending was a small proportion of the total SIF for all but the last few cycles.

5.3 Mesh and Analysis Parameters

As previously mentioned, using a script to automatically generate the FEA model allowed direct control over parameters and ensured replicability. For the static case, it was decided to model only one quarter of a sample, and to use the symmetry properties to reduce the computational effort. Material non-linearity was considered through the stress-strain curves indicated previously, and geometric non-linearity was also directly considered by using the NLGEOM option in ABAQUS. It was decided to fully model the sample in the linear fatigue model, to allow the inclusion of asymmetrical defects and misalignments. Given the relative simplicity of the fatigue model, the computational effort required was small, and thus including the complete model had negligible impact on the total analysis time.

The static samples were modeled as fixed at one end, and had a moving boundary condition in the direction of the load at the other end, simulating a displacement-controlled test. For the fatigue model, a pressure load was applied at the end to simulate a remote stress σ. Motion in the Y-direction was unrestrained, which allowed full development of Poisson effects.

The mesh was primarily composed of 2D second-order quadrilateral elements with reduced-integration, using a plane strain assumption (CPE8R type in ABAQUS). For the linear elastic J-integral model, collapsed CPE8R elements were used at the weld root to better represent the singularity at what is effectively a crack-tip. Instead of a quadrilateral shape, in collapsed elements, three of the eight nodes are "combined" into one which gives the element a triangular shape, and mid-point nodes are advanced to a quarter of the length between the crack tip and the other end of the element. These elements were then

arranged in a pie shape around the crack tip, shown in Figure 5.6.

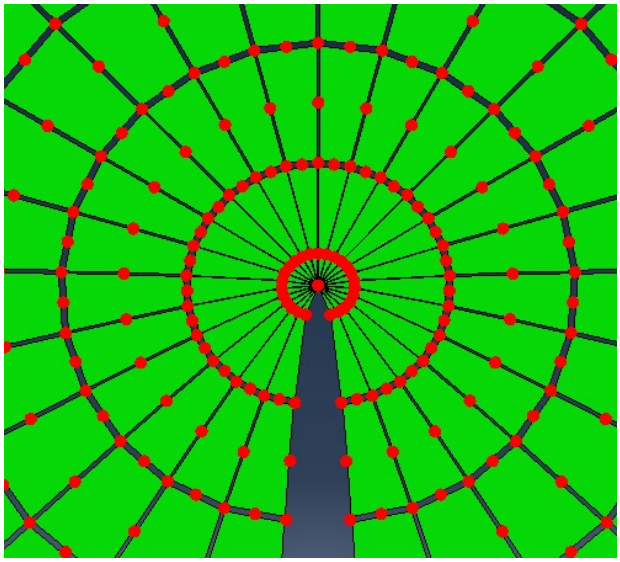

Figure 5.6: Typical mesh at the crack tip for the linear elastic model used in the J-integral method. The bright red points represent node locations. Note the inside-most ring which has its nodes at the quarterpoint instead of the midpoint.

For the static tests, the mesh outside the crack-tip region was automatically generated with a specified average element size of $t/100$, and inside the crack-tip region, approximately $t/400$. Some manual adjustments to the mesh were required at extreme values of ρ to assist the automatic mesh generator, but care was taken that this would only increase the mesh density. A typical meshed quarter-model is shown in Figure 5.7 In the contour integral tests, the mesh was much coarser at $t/20$, reducing down to approximately $t/100$ near the crack tip. A total of 6 contours were considered in the J-integral calculation to ensure path independence. This was found, through a mesh convergence study described below, to provide more than adequate results.

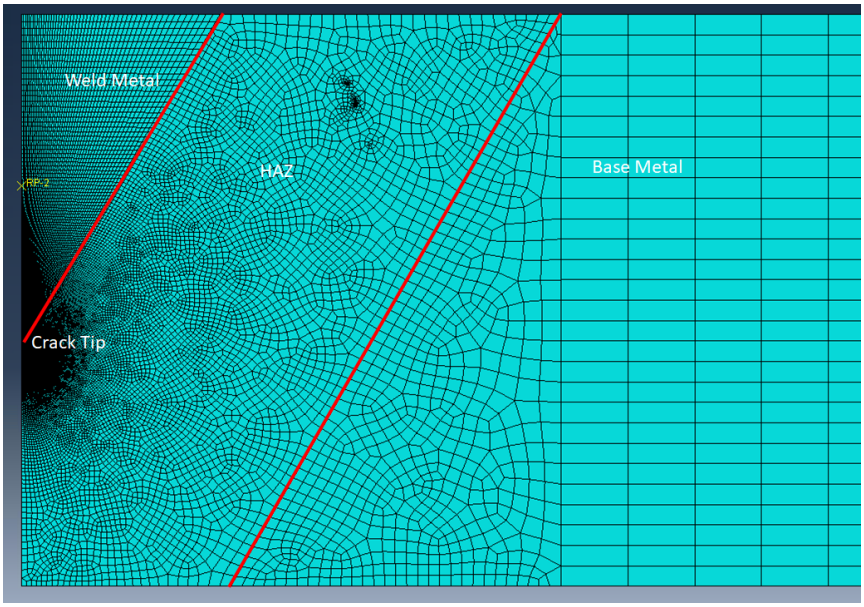

Figure 5.7: Typical mesh on a quarter-model of the statically loaded samples.

Static tests mesh convergence study

The parameter used to establish convergence in static tests was the Y-direction strain found by the virtual extensometer shown in Figure 5.1. This value was directly compared with experimental results. It was measuring highly localized values in the most highly stressed part of the model, making it an essential parameter for convergence in this case. The value at a net section stress of $\sigma_n = 180\,\text{MPa}$ was chosen, which is the value at which the lateral strain measurements were taken. Two degrees of penetration, $\rho = 10\%$ and $\rho = 90\%$ were chosen, as the extremes of ρ were suspected to be susceptible to the most numerical instability. The results of the convergence study are shown in Figure 5.8, confirming that the mesh size of $t/100$ was adequate.

Contour integral mesh convergence study

Two parameters were considered for convergence with the fatigue tests. In both cases, the convergence study was done on a sample with $\rho = 10\%$ and $\omega = 0.9$, which was identified

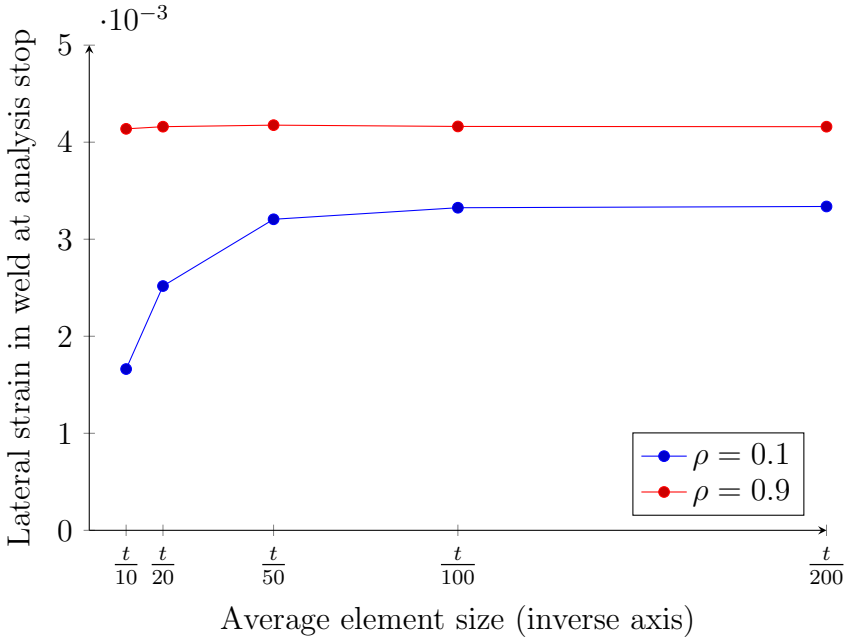

Figure 5.8: Mesh convergence study on the strain measured using the virtual extensometer shown in Figure 5.1.

as the range of parameters most susceptible to numerical instability. First, the result of the J-integral was taken at the crack tip as it was the main output desired from the FEA model used in fatigue. This was done at both the crack tip nearer the edge and the one farther from the edge as the sample was asymmetrically loaded (Figure 5.5), but the dependency on the mesh size was much higher at the crack tip nearer to the edge and so the convergence study is only shown for this side.

Second was the error in path independence of the J-integral value. The relative error between the maximum and minimum values of the J-integral of all contours was thus calculated. In general, this error should remain under 5% to confirm convergence. As multiple contours are taken, they will have different values due to errors in approximation. Path independence is however an important property of the J-integral and thus, the difference in value by contour should be minimized. The results of the convergence study on the J-integral value is shown in Figure 5.9 and on the path independence in Figure 5.10. It

can be seen that the J-integral converges extremely rapidly, with a very coarse mesh being completely adequate to calculate the contour integral, justifying the use of a $t/20$ mesh size which has less than 0.01% relative error with the $t/50$ mesh size. The path independence always remains under 5% even at the coarsest mesh.

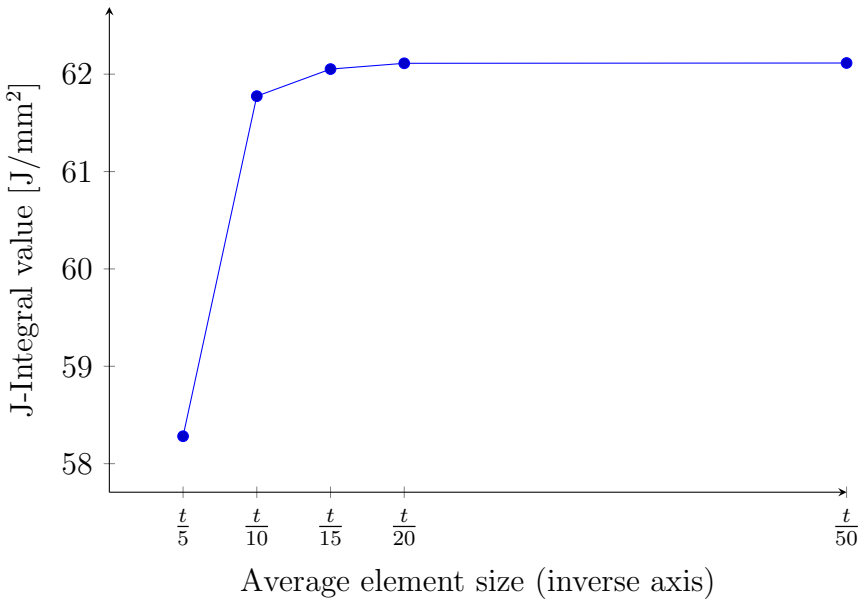

Figure 5.9: Mesh convergence study on the calculated value of the J-integral.

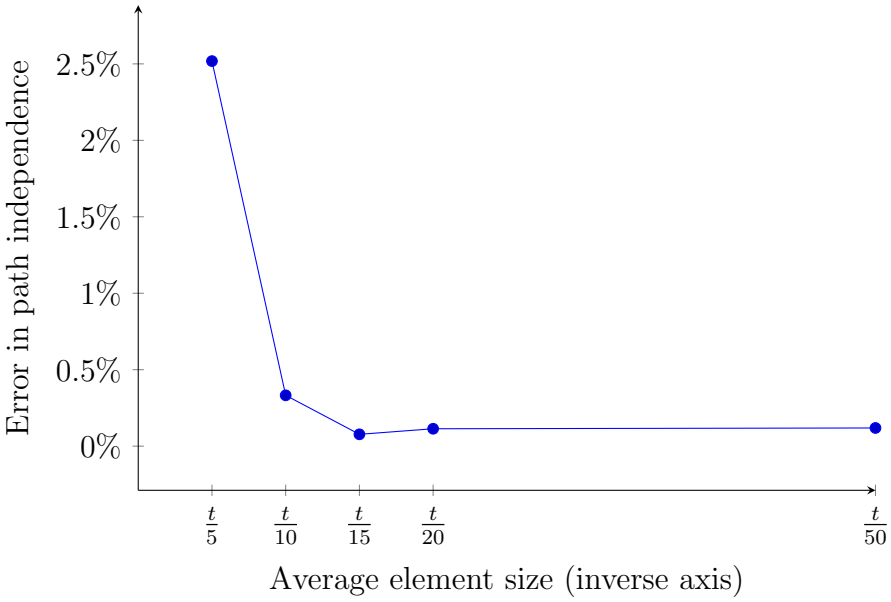

Figure 5.10: Mesh convergence study on the path dependence of the J-integral.

Chapter 6

Results and Discussion

6.1 Effective Throat of Welds

After testing the welds to failure, it was immediately clear that some samples suffered from major lack of penetration defects, as shown in Figure 6.1. Every sample thus had its actual weld size measured by the method described in Section 3.5.

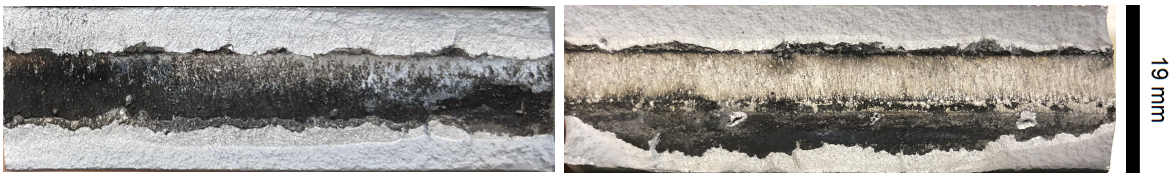

Figure 6.1: On the left, a weld with a penetration specified at 50%. On the right, a weld with 70% specified penetration. The actual degrees of penetration were 55% and 44% respectively.

Additionally, significant porosity was observed in some welds as shown in Figure 6.2. This corresponds with previous findings in the literature which noted that PJP welds generally exhibited more porosity than their CJP counterparts [30].

Figure 6.3 shows the measured degree of penetration as opposed to its specified value, while Figure 6.4 shows the difference in penetration observed for different levels of specified

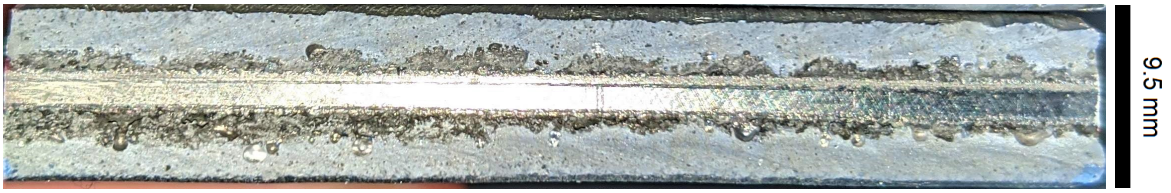

Figure 6.2: Failure plane of a 1080A sample showing significant porosity.

penetration. These measurements indicate severe discrepancies between the weld size as specified and as observed. In general, welds with their degree of penetration specified as 50% or less had their actual weld size either larger or equal to specified. However, once the specified degree of penetration increased, there was significant under-penetration, leading to welds up to 30% smaller than specified. In fact, for the 19 mm [3/4"] plates, there was no increase and even a decrease in absolute weld size with a higher groove preparation depth.

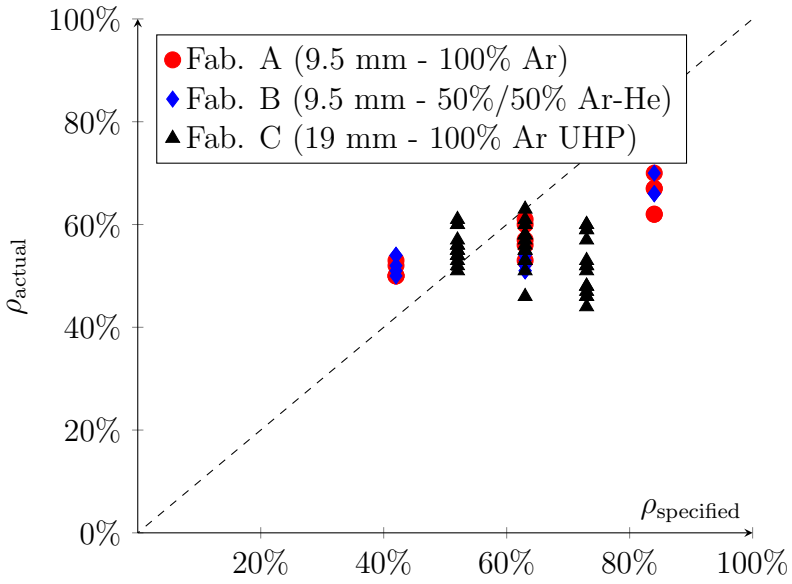

Figure 6.3: Measured degree of penetration as a function of the specified degree of penetration. The dashed line indicates the line where $\rho_{\text{actual}} = \rho_{\text{specified}}$.

Observation of the samples confirmed that the grooves had been properly prepared,

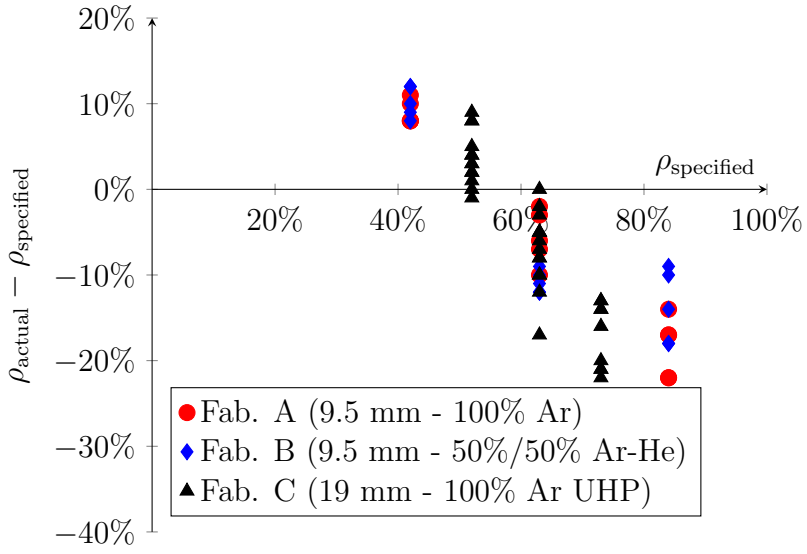

Figure 6.4: Difference in the degree of penetration ρ between actual and specified weld size. Positive values indicate welds measured larger than specified, and negative values smaller welds than specified.

with the groove depths and angles corresponding to their design specification as shown in Figure 3.1. With a groove angle of 60 degrees specified, this satisfies both the CSA W59.2-18 (minimum 60°) and the Aluminum Design Manual (minimum 45°) requirements for the effective throat to be taken as equal to the groove depth.

As can be seen in Figure 6.4, the samples from the three fabricators all exhibited the same discrepancy between specified and actual penetration. This suggests that the underpenetration may not be due to errors in the welding processes but rather because the code-specified minimum groove angles were not large enough to ensure proper penetration. An immediate solution would be rigorous evaluation using ultrasonic testing, a non-destructive testing method that allows the measurement of the effective throat of PJP welds.

6.1.1 Weld Roughness

The measurements taken as described in Section 3.5.1 were used to quantify the roughness of the welds. The mean weld throat and every deviation over 100 equally spaced points were measured for each sample and the standard deviation was calculated. The standard deviation $\hat{\sigma}$, used as a parameter for roughness, was then compared to the degree of penetration ρ. It was clearly observed that the samples from fabricator C, which have a 19 mm thickness, had significantly rougher welds, as shown in Figure 6.5.

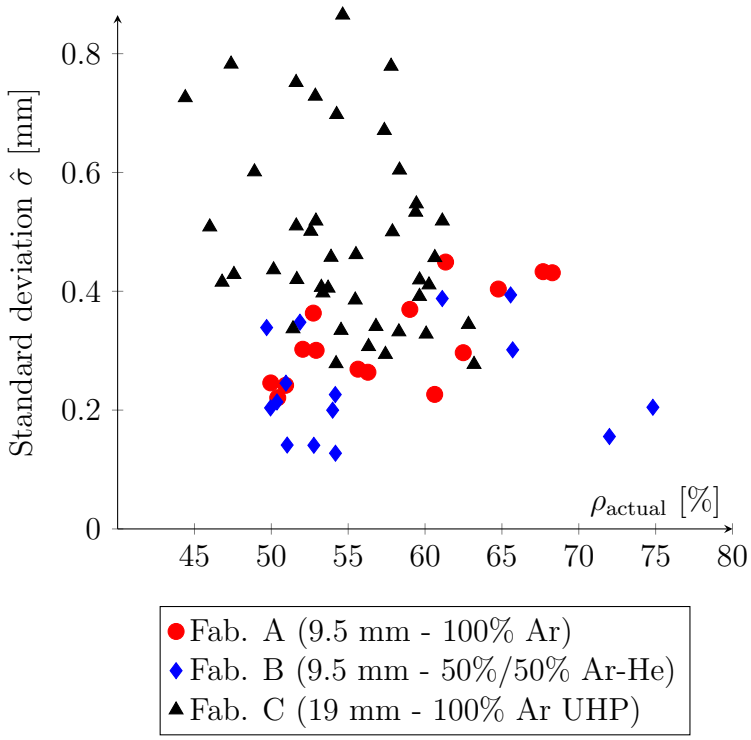

Figure 6.5: The roughness of the welds with varying degrees of penetration. It can be seen that the 19 mm samples had much higher roughness.

To adjust for the thickness of the plates, the coefficient of variation was calculated, defined as such:

$$COV = \frac{\hat{\sigma}}{t_e} \tag{6.1}$$

Where t_e is the average effective throat, measured by dividing the total weld area by the width of the sample. Since the effective throat t_e is a function of the sample thickness, for the same degree of penetration, doubling the thickness doubles the effective throat. Finding the COV was thus in essence an adjustment for thickness. When looking at the COV in Figure 6.6, all significant differences between fabricators essentially disappear. Additionally, there is no clear correlation between the degree of penetration and the weld roughness.

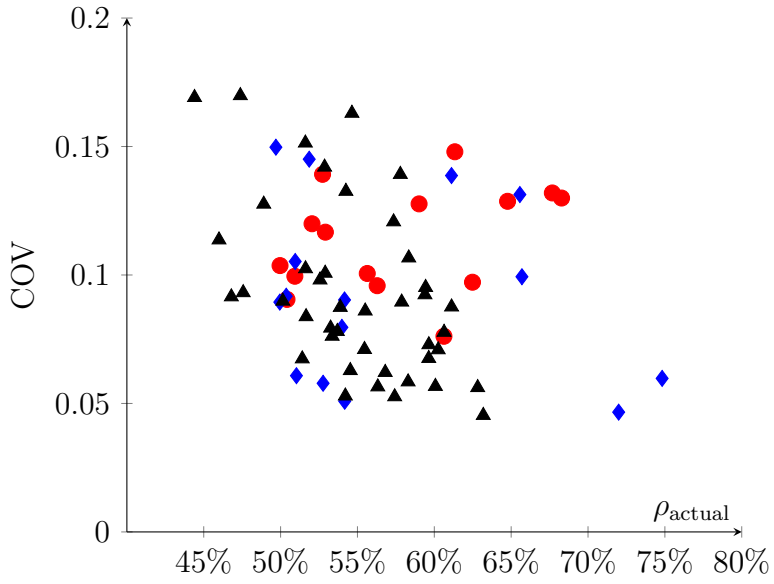

Figure 6.6: The coefficient of variation of weld throat depths with varying degrees of penetration. There is no clear relationship between the COV and the degree of penetration ρ. Legend is the same as in Figure 6.5.

6.2 Weld Cross-Section and Micro-Hardness Measurements

The micro-hardness measurements taken per Section 3.2 show the extents of the heat affected zone in Figure 6.7. A few interesting effects can clearly be observed.

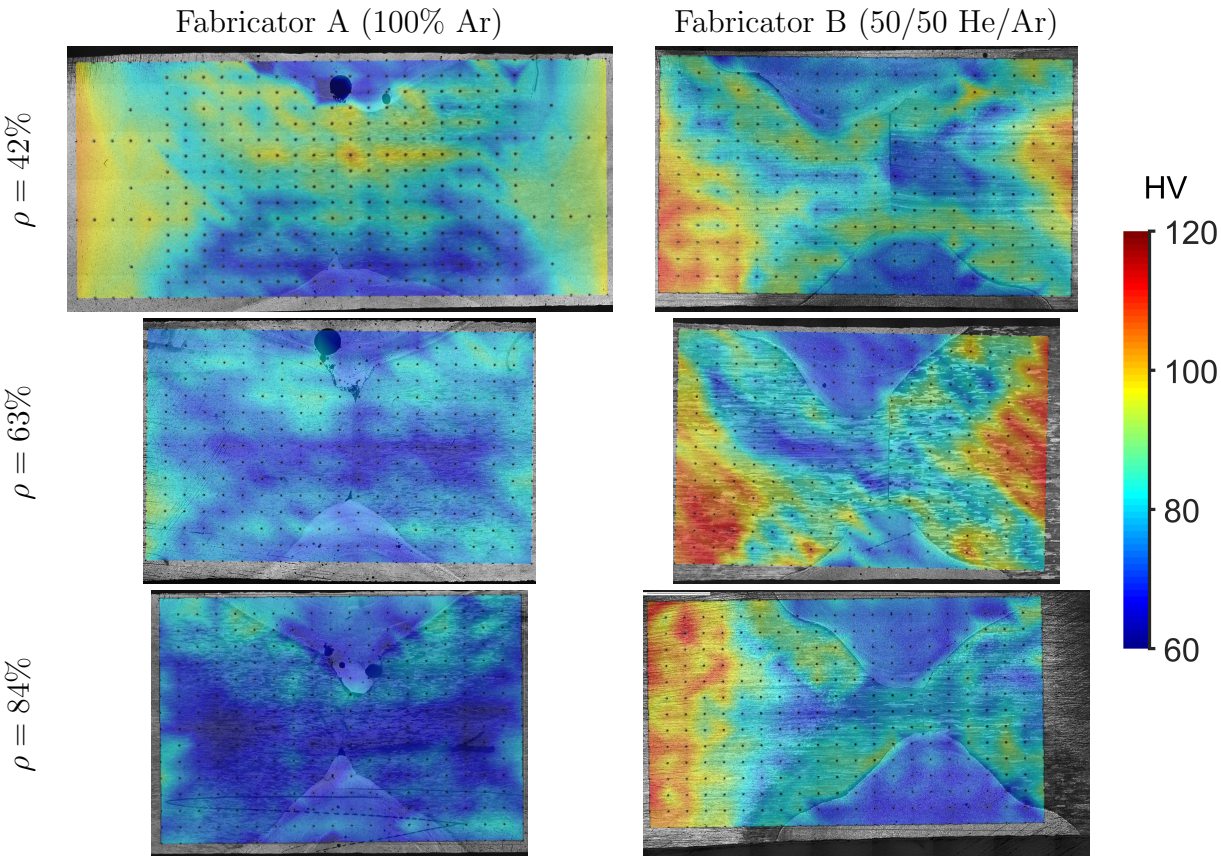

Figure 6.7: Hardness maps of the welded samples. Each image is at the same scale, with the height of each picture equal to the plate thickness (9.5 mm). The degree of penetration (specified) is shown on the left, and the hardness is measured on the Vickers scale as shown on the right.

The welds are consistently the softest part of the measured area. This however does not translate to them being weaker. Since the welding alloy (5356) is different than the base metal (6061), the metals have very different strain hardening profiles (5356 has a lower yield strength but hardens much more dramatically than 6061). Hardness is thus a much better direct comparison tool between the yield strengths of the two different alloys than ultimate strengths.

In all cases, there is a visible weak path which crosses from one side of the plates to the

other. This supports the concept of using the HAZ strength when checking the strength of PJP welds. Samples from fabricator A, who used a 100% argon shielding gas, generally had a much larger HAZ than fabricator B. Comparison of records shows that samples from both fabricators were welded using similar parameters, which suggests that the shielding gas had a large influence on the extent of the HAZ. However, in both cases, there is a weak path as described previously, which suggests that the shielding gas may not have a large influence on the performance of the PJP welds.

A "halo effect" occurs near the weld metal, which corresponds to findings observed in past studies [6]. This effect is shown more clearly in Figure 6.8. The lowest hardness is in the weld metal: this is because the 5356 alloy has relatively low yield strength, but hardens significantly and has a high ultimate strength. Moving away from the weld metal, there is then a zone of relatively high hardness, where the temperature was high enough during the welding process to completely dissolve all alloying metals, which strengthens the aluminum (though not as much as when it is fully tempered and precipitates are at their optimal concentration). Next is a significant drop in hardness that occurs because the heat of welding is not enough to dissolve all alloying metals, but enough to precipitate and lump them at grain boundaries, a process called over-aging. These lumped precipitates significantly weaken the metal. Finally, the hardness increases again as the over-aging effect diminishes until the hardness of the base metal is reached.

The softening has some noticeable asymmetry, where one side of the plate is harder than the other. The softer side likely corresponds to the first side that was welded. As the welder makes the first pass, the previously described "halo effect" as previously described takes place. After the second pass, the heat of welding is enough to over-age the entire HAZ around the first pass, which leads to the softened condition around the entire weld. The HAZ around the second pass, exposed to the highest heat, has a zone of increased hardness where the alloying metals were fully dissolved.

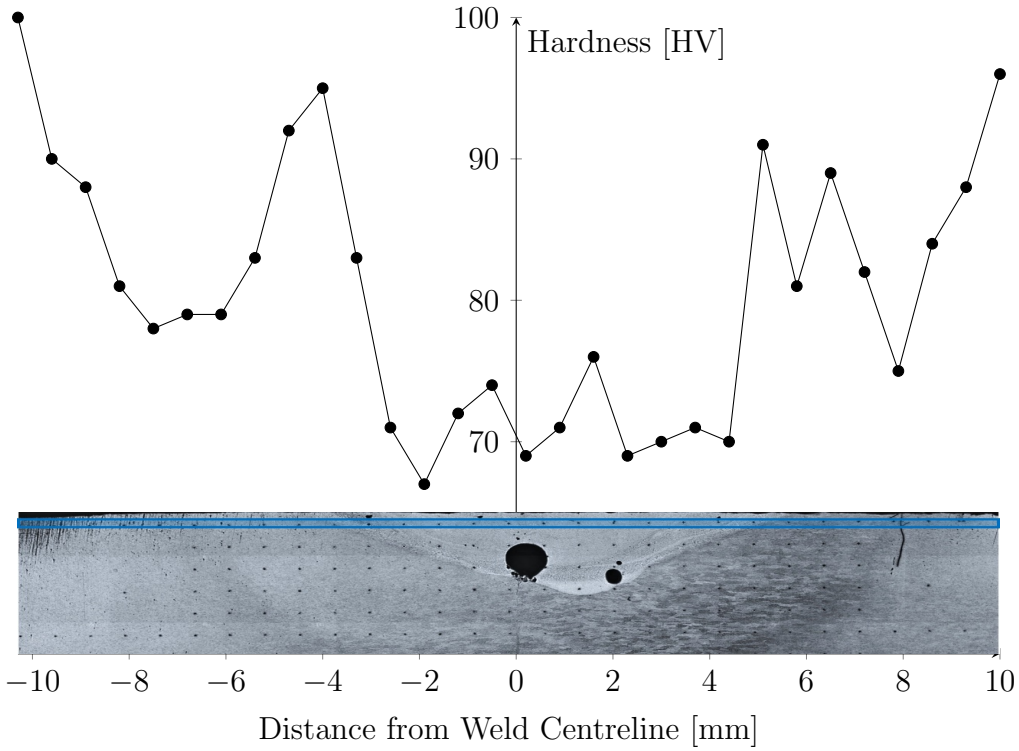

Figure 6.8: Hardness along the heat affected zone and the weld of the 1040A sample. The measurements were taken along the highlighted region. Note that the weld is skewed to one side, but the $x = 0$ location was defined by the groove centreline.

6.3 Static Tests

Overall, the static tests showed the PJP welds had relatively high strength, but very low ductility.

A typical stress-strain curve is shown in Figure 6.9. The Portevin-Le Chatelier (PLC) effect is clearly visible in the stress strain curve. This effect is characterized by the sharp serrations observed after yielding. In many 5000 series aluminum alloys, the onset of yielding causes supersaturated magnesium solutes to precipitate in voids created by plastic dislocations. In general, the PLC effect is much less pronounced in the 6061 alloy (which

do not contain supersaturated magnesium). In some cases, welded 6061 aluminum does exhibit a PLC effect due to the over-aging effect described in Section 2.1.1 and because of excess precipitates after welding [47]. The presence of serrations in the stress-strain curve thus indicates that yielding occurs either in the weld metal or in the HAZ, as expected, but it is difficult to affirm whether yielding is occuring in the weld or the HAZ.

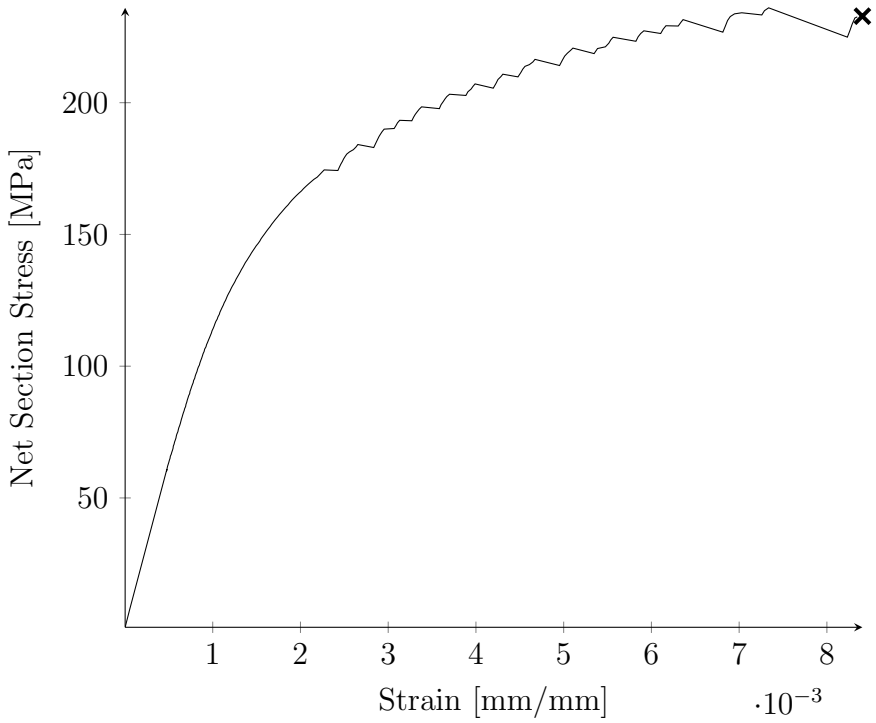

Figure 6.9: Stress-strain curve for the 1060A2 sample. The serrated pattern after yielding is attributed to the Portevin-Le Chatelier effect.

6.3.1 Strength

In all cases, failure occurred over the net section at the weld. To directly compare strength, the load at failure was divided by the net cross-sectional area, measured as explained in Section 3.5.

Influence of degree of penetration

The strength of the welds was compared to the degree of penetration in two ways - first was looking at the failure load of the welds, which did not consider the degree of penetration. Second, the net section failure stress was compared, which allowed direct comparison of the metal strength as a function of the degree of penetration, using the measured effective throat of the weld.

Figure 6.10 shows the relationship between the failure load and the degreee of penetration as measured. It can be seen that as the degree of penetration increases, so does the failure load. This is what was expected, as a higher degree of penetration translates to more weld metal resisting the load.

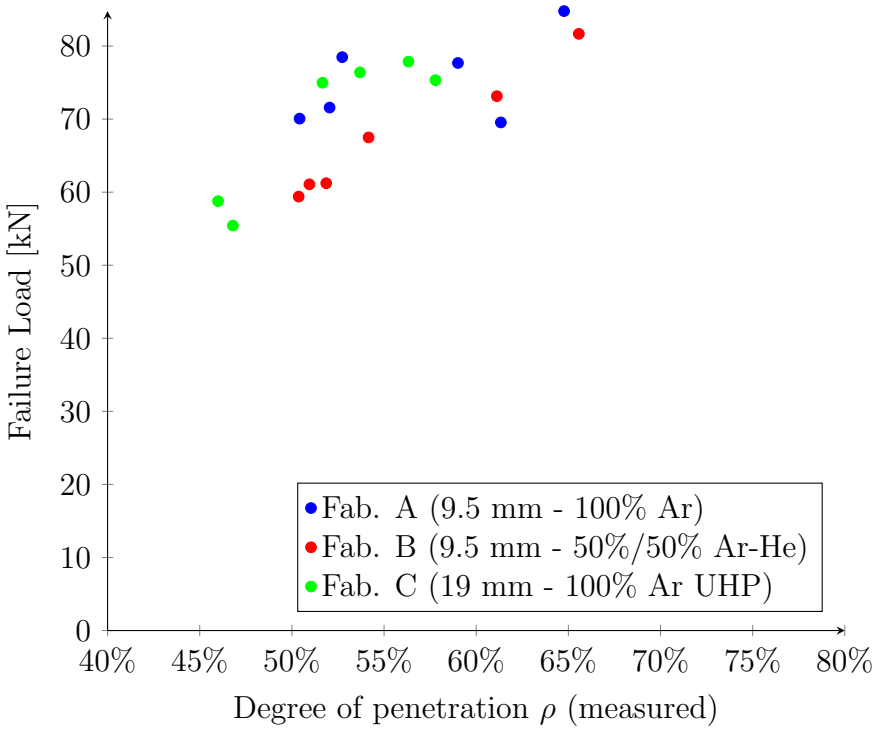

Figure 6.10: The failure load of samples as a function of degree of penetration. Note that for the 19 mm samples, the failure load was divided by two to adjust for plate thickness.

Similarly, Figure 6.11 shows the net failure stress from the tests as a function of the degree of penetration. Because of significant under-penetration as discussed previously, data over a smaller effective range of ρ than originally desired were observed in tests. This prevented inferring any significant trends between strength and the degree of penetration, as was found by Gagnon and Kennedy [24].

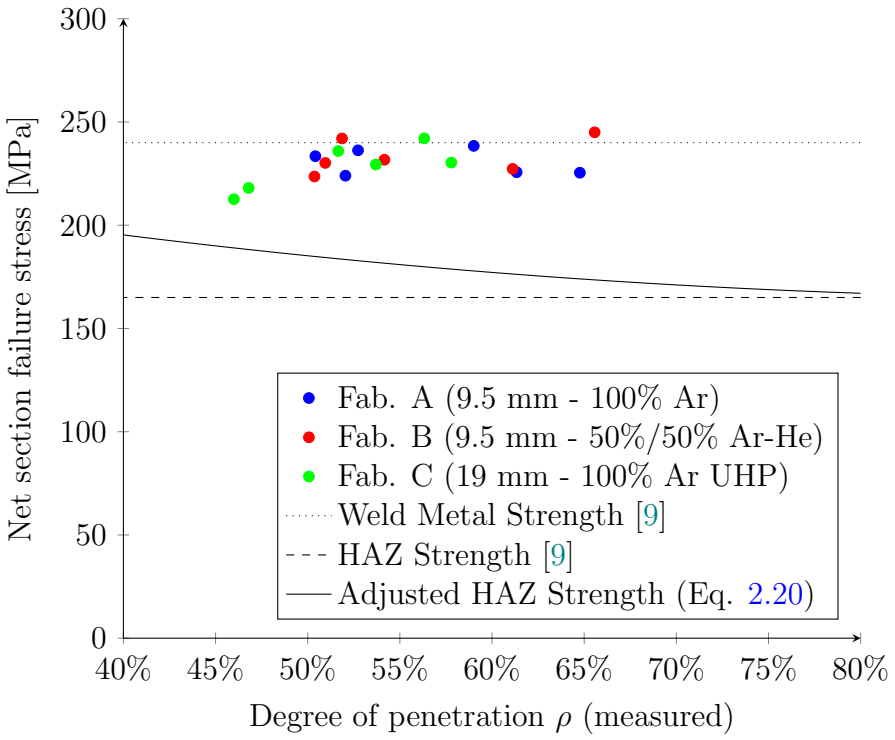

Figure 6.11: The net section failure stress and degree of penetration of samples tested statically. The HAZ and weld metal strengths were obtained from the CSA S157-17 standard, and the adjusted HAZ strength as calculated by Gagnon & Kennedy [24].

It can be seen that all samples failed near the weld filler metal strength, and much higher than the HAZ strength. Since the failure planes generally occurred near the interface of the filler and base metal interface, the overall strength may be a function of the strength of both metals. This would thus suggest that the HAZ strength is a conservative value to use in design. Using the the finite element model described in Section 5.1 allowed further

investigation on the effect of material properties.

Effect of material properties

To study the effect of varying material properties, the yield and ultimate strengths were changed by a factor of ±10% and the corresponding effect on the stress-strain curve is displayed in Figure 6.12. The exact difference on the failure stress cannot be determined as the FEA model does not simulate failure; however, the effect on the stress-strain curve is strongly indicative of the sensitivity to changing any of the three materials.

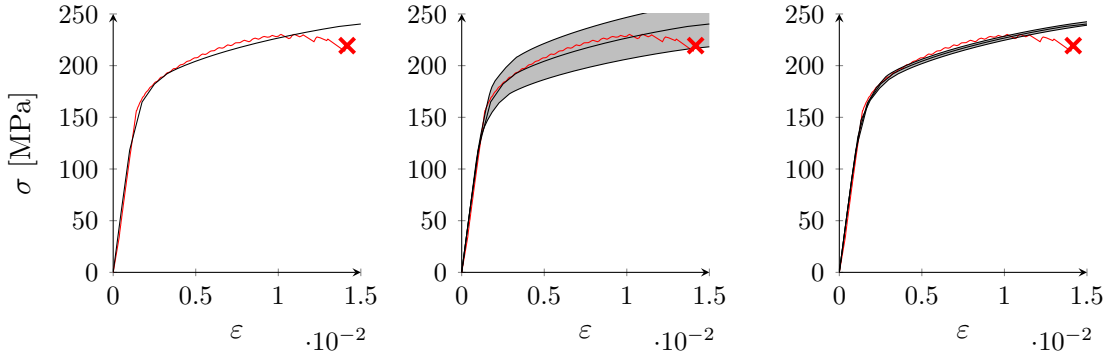

(a) Base Metal **(b)** Heat-Affected Zone **(c)** Weld Metal

Figure 6.12: Stress strain curves generated with the FEA model by varying the strength of each material by ±10%, shown in the gray range. In red, the measured stress-strain curve for the 2060C16 sample. The FEA model does not simulate failure conditions and thus does not follow the measured stress-strain curve near failure.

It is clear from Figure 6.12 that the strength depends entirely on the heat affected zone. Changing the weld metal strength impacts the overall strength negligibly, and the base metal does not affect it at all. In large part, this is explained by the HAZ being much weaker than the other materials. However, this does not fully explain the trend; the weld metal has essentially the same yield strength as the HAZ but its strength has essentially no effect on the stress-strain curve. This suggests that the failure plane always occurs in the HAZ.

6.3.2 Strain Field and Lateral Restraint

As explained in Section 3.3.1, DIC measurements were taken during tests to measure the strain field as the samples were loaded. To validate the results, a virtual extensometer with 50 mm gauge length was applied on the DIC. The corresponding stress-strain curves are shown to be in good agreement in Figure 6.13. The finite element model described in Section 5.1 was validated using extensometer-measured stress-strain data, and was also found to be in good agreement.

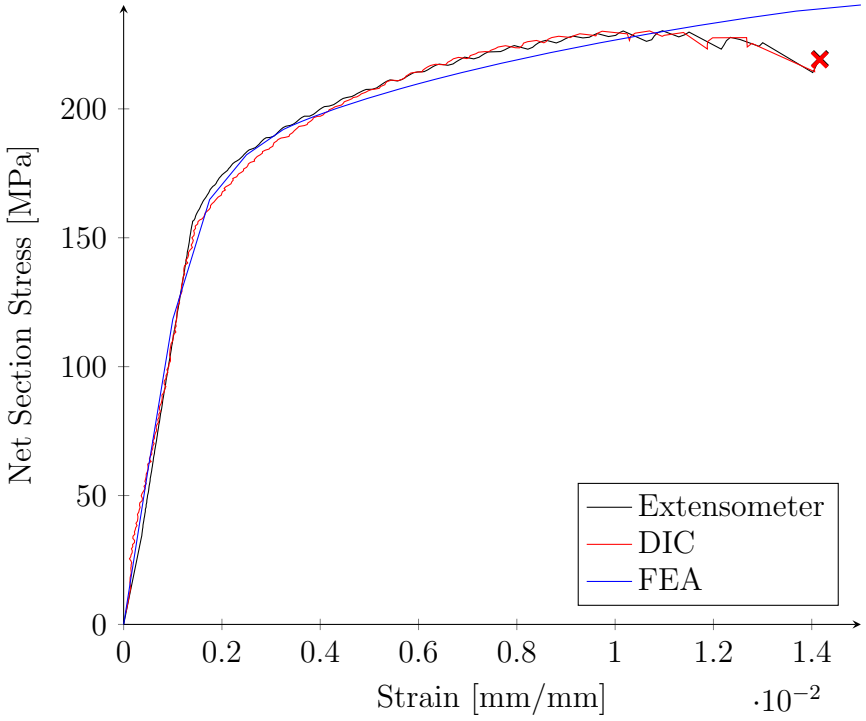

Figure 6.13: Stress-strain curves measured using an extensometer and with DIC for the 2060C16 sample. The curve generated from the FEA is also superimposed. The curves match nicely, validating the DIC and FEA measurements.

In their study, Gagnon and Kennedy [24] indicate that increased lateral restraint as the degree of penetration decreased provided an increase in net sectional strength. To verify the presence of this restraint, the FEA model was used to look at the strain in the

direction perpendicular to the load, which would be expected to reduce at lower degrees of penetration due to the described restraining effect. To do so, a virtual extensometer was added to the FEA model and the DIC measurements, which measured the strain across the weld perpendicular to the load axis. A typical strain field found by the DIC measurements, which was used to calculate the lateral strain, is shown in Figure 6.14.

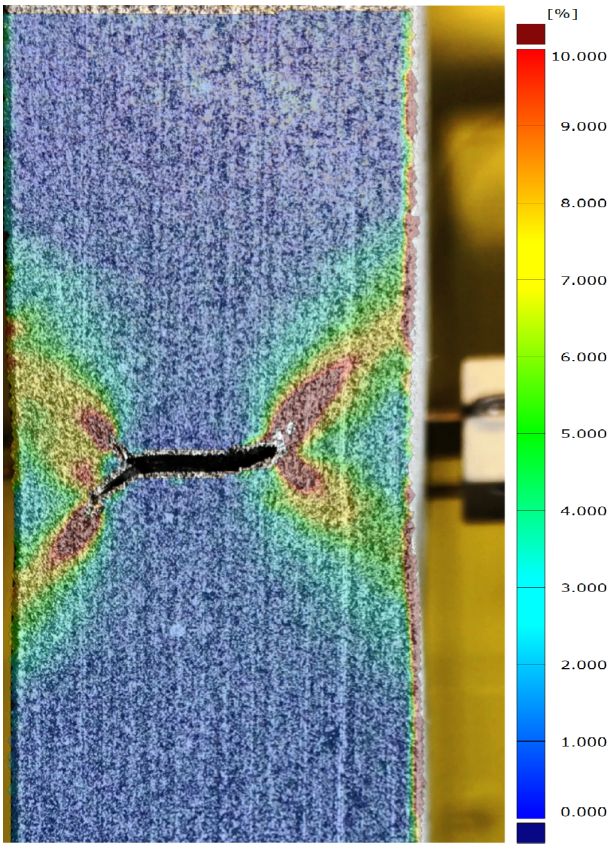

Figure 6.14: Strain field from DIC measurements on the 2060C16 sample.

To validate the measurements, the strain from the FEA was compared to the DIC measurements, as shown in Figure 6.15. Here it can be seen that the model is in good agreement with the measurements until the global strain reaches approximately 0.006. The flat curve in the early stages of loading in the DIC data is attributed to the effects of residual stresses, which were not considered in the FEA model. The divergence of the curves at

high strain is most likely the result of the loss of accuracy of the DIC measurements near the crack and the sample edge when yielding occurs as these are the most distorted areas. Since the primary concern was in observing the trend of lateral strain with regards to the degree of penetration (and not the precise values of strain), this divergence was deemed adequate.

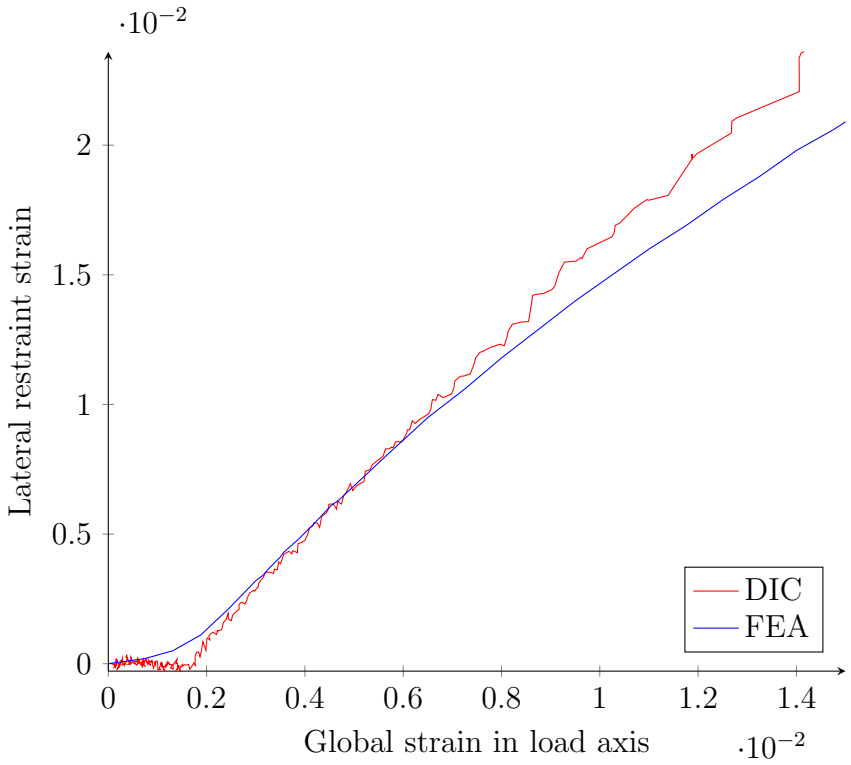

Figure 6.15: The strain in the direction parallel to the "crack" as a function of the global strain measured in the direction of loading by a 50 mm extensometer.

With the model validated, the next step was to examine the restraining effects at various degrees of penetration. The lateral restraint strain at a net section stress of 180 MPa was measured at various degrees of penetration. This corresponds to the limit at which the FEA model showed a good match with the DIC data. At this value, plasticity effects are well developed, and inaccuracies from the FEA model's lack of consideration for failure are negligible. The results of this study are shown in Figure 6.16.

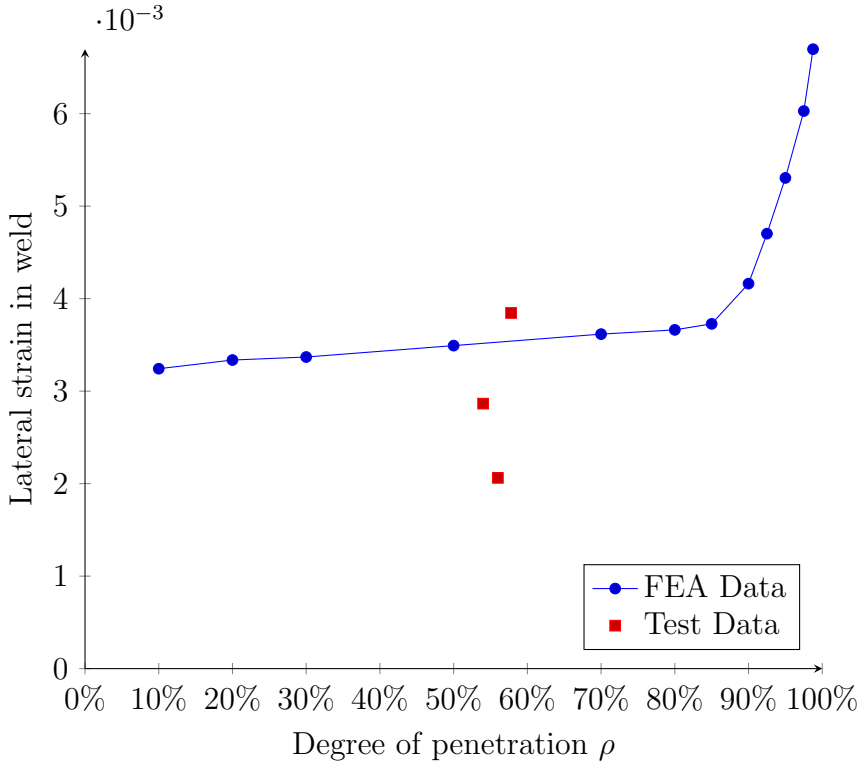

Figure 6.16: The lateral strain in the weld at a net section stress of 180 MPa. Lower levels of strain indicate higher restraint, increasing the effective strength. The individual points correspond to the data measured from DIC.

Overall, it is seen that as the degree of penetration increases, so does the lateral strain in the weld. The increased confinement from the unloaded portion of the joint significantly reduces strain in the lower penetration welds. Overall, these results support the findings of Gagnon and Kennedy [24] that the lateral restraint in strain in the weld is a strengthening mechanism for PJP welds. The data from DIC were also plotted over the existing data, however the range of degrees of penetration is too small to confirm any trends. The three data points also exhibit a high variance, likely owed to the fact that the DIC measurements are relatively inaccurate at a such a small scale near the weld, and to the difficulty in tracking points near the crack tip and the plate edge.

6.3.3 Ductility

Overall, the PJP welds exhibited extremely low ductility, which is typically high in aluminum welds because of the annealing effect of welding. Two phenomena cause this reduction in ductility. First is that since the welded area is much weaker than the base metal, fracture occurs near the weld before the onset of yielding in the base metal. However, this affects all aluminum welds. PJP welds suffer from a second reduction in ductility due to the lateral restraint explained in the previous section. The lateral restraint, which raises the effective strength of the weld, also stiffens against yielding movement. The weld thus remains elastic for a larger proportion of its loading.

A method sometimes employed to increase weld strength in aluminum is to perform a post-weld heat treatment, which can bring material properties to their base unwelded values. However, it is doubtful that this would increase ductility as it would essentially leave all yielding to occur in the weld metal, as the heat affected zone would no longer be yielding. Furthermore, such processes are impractical to perform in typical structures other than specialized applications such as highway luminaries.

The stress-strain curve for the PJP welds is compared to the base metal 6061-T6 in Figure 6.17. The lack of ductility is particularly critical in aluminum welds as, unlike structural steel, welds are often weaker than the base metal and all ductility in a structure may come from the connections. As such, using PJP welds in highly loaded or low-redundancy members would be ill-advised. Though unmentioned in the respective commentaries, this is likely a principal reason to discourage or outright ban the use of PJP welds in aluminum design standards.

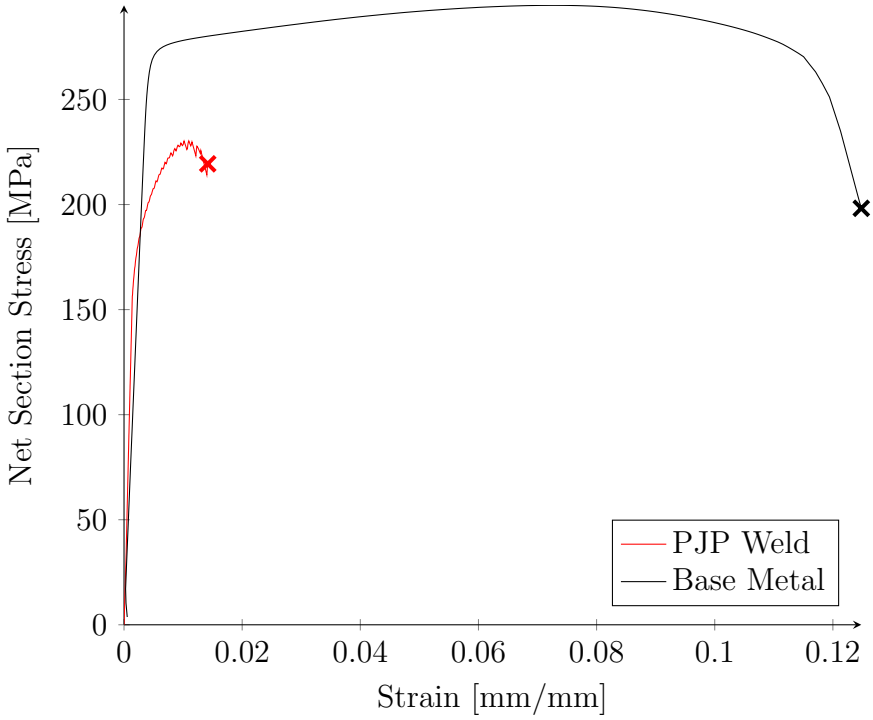

Figure 6.17: Stress-strain curve of a PJP weld compared to the 6061-T6 base metal.

6.4 Fatigue Performance

6.4.1 Statistical Analysis of Fatigue Data

It is typical for fatigue test data to have considerable scatter due to the inherent randomness of crack initiation and growth. The International Institute of Welding (IIW) publishes guidelines on the analysis of fatigue data that were used when analyzing the fatigue results in this experimental program [18].

As explained in Section 2.2.2, the relationship between stress range and the number of

cycles is assumed to have an exponential form:

$$\Delta\sigma = \left(\frac{C}{N}\right)^{\frac{1}{m}} \tag{6.2}$$

or, to determine the life for a stress range:

$$N = C\Delta\sigma^m \tag{6.3}$$

This can be linearized as such:

$$\log N = \log C - m \log \Delta\sigma \tag{6.4}$$

By using a least squares regression, the best-fit values of C and m can be determined. It is also desirable to determine "characteristic" values of C and m, associated with a certain probability of survival. In this study, a survival probability of 95% was selected, at a confidence level on the mean of 75%. Establishing the characteristic values allows direct consideration of the scatter in data and the survival probabilities selected are in line with most design standards.

The method proposed by the IIW begins with the assumption that the slope m is constant at all confidence levels. Thus, only the value of C is changed from the mean to reflect the desired survival probability. The first step is to calculate the corresponding value of C for each data point, by rearranging Eq. 6.4:

$$\log C_i = \log N_i + m \log \Delta\sigma_i \tag{6.5}$$

The average $(\log C)_m$ and standard deviation $\hat{\sigma}$ of $\log C_i$ values are then calculated. From this, the characteristic value of C at the given survival probability level can be calculated:

$$\log C = (\log C)_m - k \times \hat{\sigma} \tag{6.6}$$

where k is a factor accounting for the size of the data set. In some design standards, k is

taken as a constant value of 2, corresponding to the mean less two standard deviations as a characteristic value. The IIW however suggests that sample size should be considered in the value of k, to account for uncertainty in the variance of the data. This is done using a formula based on Student's t-distribution for variability of the mean, and the χ^2 distribution to account for the unknown variance:

$$k = \frac{t_{(\beta,n-1)}}{\sqrt{n}} + \phi^{-1}_{(\alpha)}\sqrt{\frac{n-1}{\chi^2_{\left(\frac{1+\beta}{2},n-1\right)}}} \tag{6.7}$$

where n is the number of samples, t, ϕ^{-1} and χ are the two-sided t-distribution, inverse normal distribution and χ^2 distribution, α is the survival probability (taken as 0.95) and β is the level of confidence of the mean (taken as 0.75). When $n = 20$ samples are tested, Equation 6.7 is equal to 2, and Equation 6.6 becomes approximately equivalent to the mean less two standard deviations used in some standards. Testing less than 20 samples makes Equation 6.7 give more conservative results, and more than 20 samples less conservative, representing increased certainty in both the mean and variance as more samples are tested. The characteristic value of C can thus be calculated for the desired survival probability.

6.4.2 Stress-Life Data

The stress-life data obtained from tests is shown in Figure 6.18 for tests with $R = 0.1$ and Figure 6.19 for tests with $R = 0.5$. Consistent with the CSA S157 standard and the ADM, the fatigue limit was assumed to occur at 5,000,000 cycles [9, 10]. The best-fit and 95% survival lines are also plotted, calculated in accordance with the previous section. The test samples which failed with $N < 10,000$ cycles were not considered when fitting the S-N curve, as maximum stresses near the yield strength significantly affect performance and do not exhibit the linear relationship observed in S-N curves.

Figure 6.20 compares the S-N curves for all three fabricators (fabricator C at $R = 0.1$ and $R = 0.5$) by comparing the stress range estimated to cause failure at $N = 2{,}000{,}000$ cycles. This is also the reference fatigue strength used by Eurocode 9 and the IIW [18, 33].

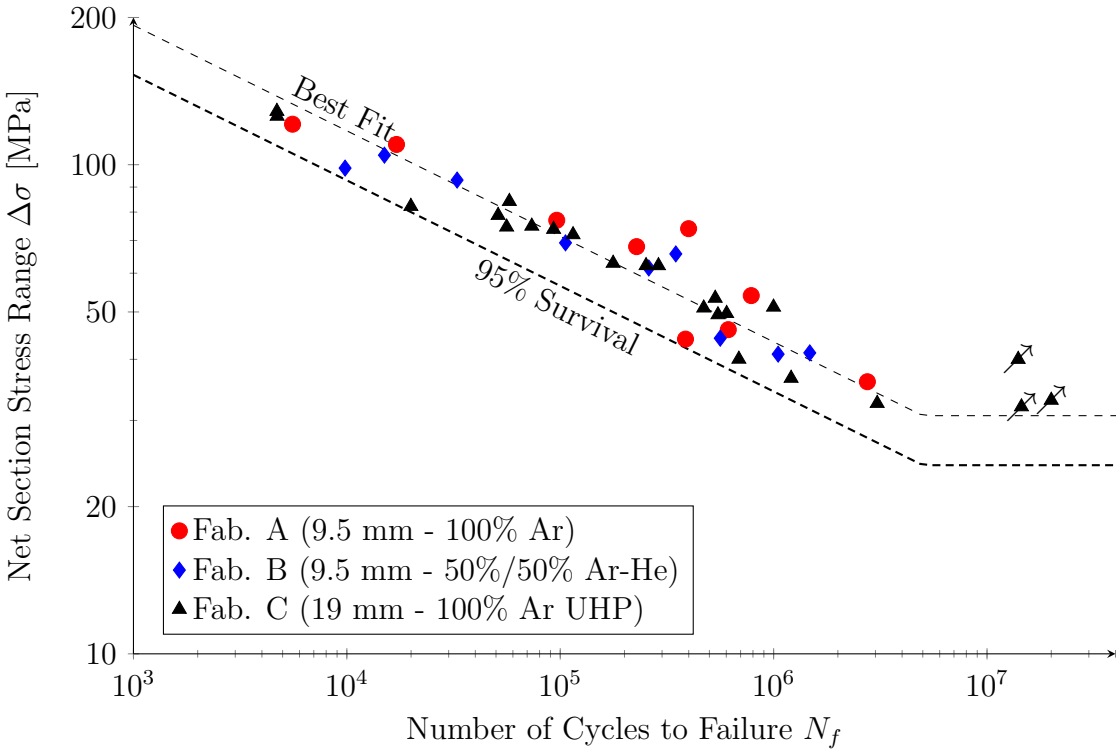

Figure 6.18: Stress-life data for all tested samples with $R = 0.1$.

Effect of stress ratio

It is observed that the samples tested at $R = 0.5$ have a lower fatigue performance, with the stress range at $N_f = 2{,}000{,}000$ approximately 25% lower than at $R = 0.1$ (Figure 6.20). This does not agree with common wisdom that the stress ratio or mean stress has negligible effect in welded joints, described in Section 2.2.1. There are two principal causes which could explain this:

- Residual stresses are typically lower in small-scale samples such as those tested in this study. The IIW [18] suggests testing these samples at $R = 0.5$ or higher to mimic the effect of higher residual stresses. Alternatively, if testing is done at lower stress ratios such as $R = 0$, the IIW suggests to simply reduce the stress range by 20% for a given life.

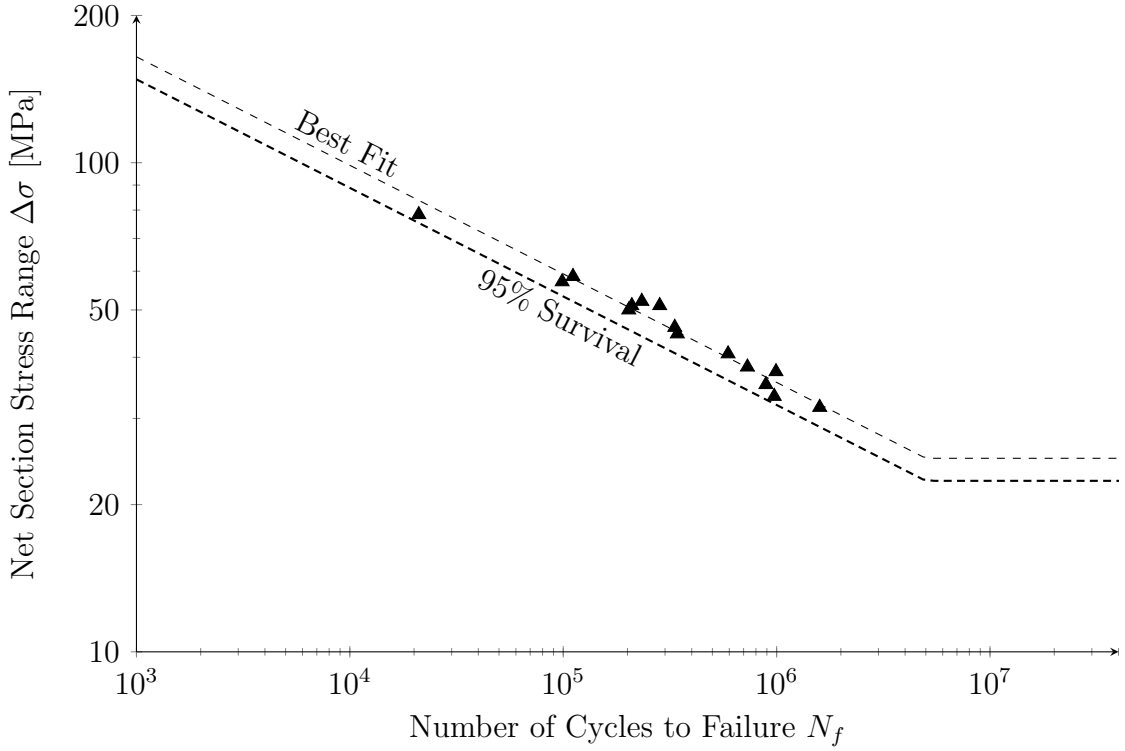

Figure 6.19: Stress-life data for all tested samples with $R = 0.5$.

- There is a possibility that residual stresses are lower in aluminum PJP welds than anticipated. This could stem from some stress relieving in the welding process, metal relaxation, or other processes. One would anticipate reduced residual stresses to reduce the crack propagation rate by reducing the effective stress ratio.

Since all samples tested at both $R = 0.1$ and $R = 0.5$ were exactly the same size and thickness, it is impossible to determine the effect of sample size on the residual stress and the impact of stress ratio on weld performance. However, lower residual stress in smaller samples is a known phenomenon and it seems highly plausible that this is the driving factor for the difference between $R = 0.1$ and $R = 0.5$ samples. Some tests at greater thicknesses and weld sizes would provide a quick means to evaluate this effect. If it is suspected, as the second bullet proposes that residual stresses are low in PJP welds overall, direct residual

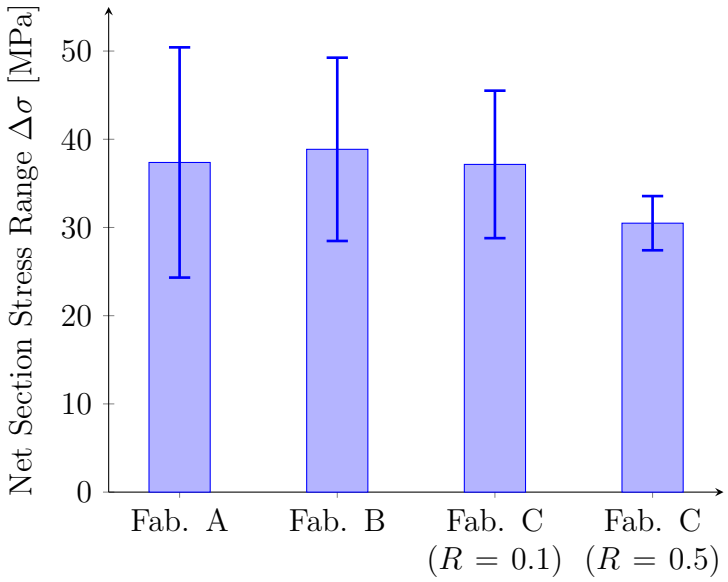

Figure 6.20: The stress range associated with a total life of $N_f = 2,000,000$ cycles. The error bars indicate the 95% survival stress range as calculated previously.

stress measurements could be undertaken using methods such as X-ray diffraction.

There is also a significant decrease in variance in the $R = 0.5$ tests. In fact, while the best-fit estimate is lower, the 95% survival estimate for fatigue performance is almost the same as for the $R = 0.1$ samples. This is most likely attributable to the reduced influence of residual stresses. The mean stress applied by the loading frame is practically constant, but the mean stress from residual stresses is not, due to variations in the weld throat, inherent defects, metal relaxation, etc. In the $R = 0.5$ samples, the machine-applied mean stress is a much bigger proportion of the total mean stress, which abates the variance from residual stresses. This also suggests that residual stresses are lower than expected, contrary to conventional wisdom.

6.4.3 Adjusted Stress-Life Data and Comparison with Standard S-N Curves

As previously explained, the stress ratio had a larger influence on fatigue performance than was expected from the literature review. The IIW recommends using test data at $R = 0.5$ in welds [18], and it was decided to adjust the $R = 0.1$ data to their equivalent at $R = 0.5$. This was done using the Walker equation as a correction for mean stress, which has been found to correspond well to aluminum samples [48]. The Walker equation takes the following form:

$$\Delta\sigma_{R=-1} = \Delta\sigma \left(\frac{2}{1-R}\right)^{1-\gamma} \tag{6.8}$$

where $\Delta\sigma_{R=-1}$ is the equivalent stress range at $R = -1$, *ie* with full stress reversal, γ is a material constant, which was found to be approximately 0.63 for 6061-T6 aluminum and 0.66 for a 5000-series alloy in a previous study [48]. This can quickly be checked by comparing the $R = 0.1$ and $R = 0.5$ data at 2,000,000 cycles, as they should have the same equivalent stress range at $R = -1$

$$37.15 \left(\frac{2}{1-0.1}\right)^{1-\gamma} = 30.48 \left(\frac{2}{1-0.5}\right)^{1-\gamma} \tag{6.9}$$

Solving:

$$\gamma = 0.66 \tag{6.10}$$

This is the same value as the one found in previous studies [48]. While this is certainly not a rigorous fitting procedure for γ, it does confirm that the material behaviour is generally as expected. The stress range for data at $R = 0.1$ can thus be converted to its equivalent

at $R = 0.5$.

$$\Delta\sigma_{R=0.5} = \Delta\sigma_{R=0.1}\frac{\left(\frac{2}{1-0.1}\right)^{1-0.66}}{\left(\frac{2}{1-0.5}\right)^{1-0.66}} \tag{6.11}$$

$$\Delta\sigma_{R=0.5} = \Delta\sigma_{R=0.1} \times \frac{30.48}{37.15} \tag{6.12}$$

$$\Delta\sigma_{R=0.5} = \Delta\sigma_{R=0.1} \times 0.819 \tag{6.13}$$

Note that since only two stress ratios were tested, this simplifies down to scaling the stress range by a constant. However, the solved value of $\gamma = 0.66$ matching with previous studies confirms that this method is adequate. With all data points converted, a new stress-life diagram was created, shown in Figure 6.21.

When comparing with the CSA S157 (and the ADM) standard S-N curves, there is a clear discrepancy in terms of slope, which will be discussed further below. It can be seen that Category E curve is the only one that is conservative for all test cases. However, in the high cycle fatigue, it is excessively conservative when compared to the data. Category D, on the other hand, is closer to the test data and the 95% survival curve. However, in the low-cycle regime, it is somewhat unconservative. Category C is practically always unconservative and clearly unsuitable for the design of PJP welds.

The fatigue limits predicted by the standard curves for Categories D and E are clearly much lower than the data seems to suggest, and the best-fit line is also under the three runout samples. In the case of the best-fit line, the "knee" where the fatigue limit begins was manually selected at 5,000,000 cycles. This was done because there were few samples with extremely high cycle counts. It is also consistent with the CSA S157 and ADM design standards, which set the knee at 5,000,000 cycles. The design standards may have selected this value with added conservatism, as the assumption of infinite fatigue life would be associated with components undergoing less maintenance and higher damage in case of failure.

When comparing with the CSA S157 S-N curves to the best-fitted S-N curve, there is a clear discrepancy in terms of slope. The slope calculated from the test samples is

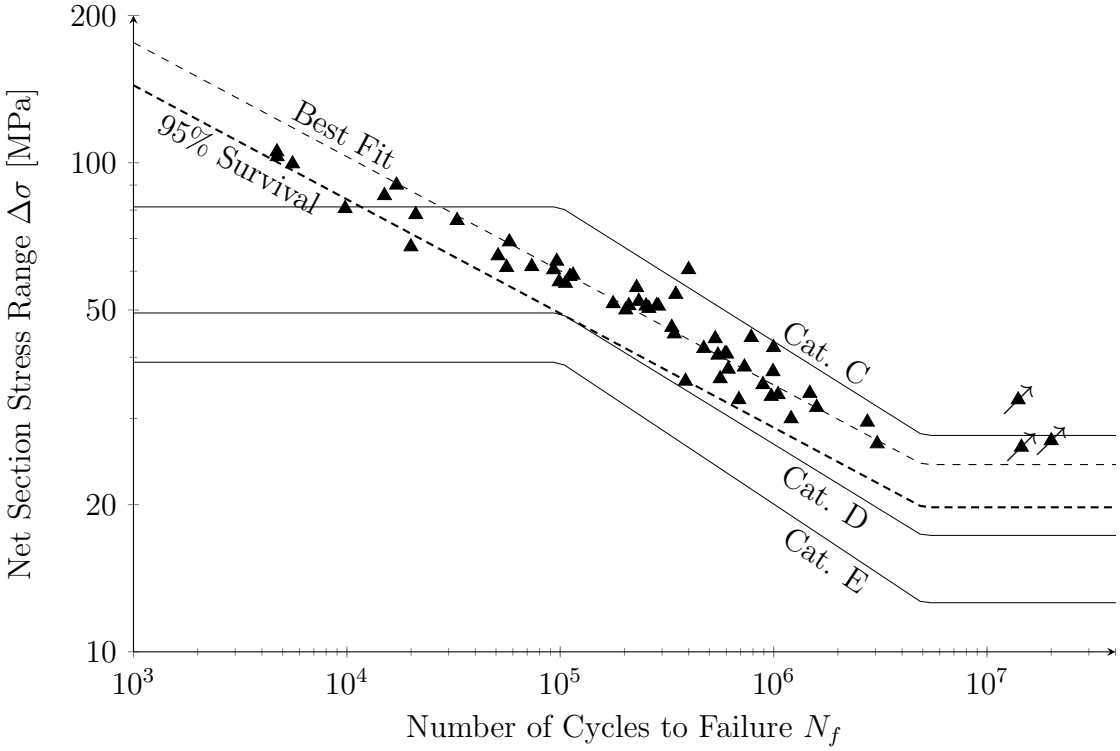

Figure 6.21: Stress-life data for all tested samples, adjusted for $R = 0.5$. The three solid lines represent the standard S-N curves used in CSA S157 and the ADM.

approximately 4.3, while the standard curves are all at approximately 3.6. It was thus decided to perform a statistical test to confirm whether Category D or E S-N curves could be used for PJP welds. Another publication by the IIW provides information on performing this test [49]. The approach employed is to show with a given confidence level that PJP welds will always have a higher fatigue performance than predicted by the design S-N curve. In other words, the number of cycles to failure at a given stress level will always be higher than predicted by the design S-N curve, with 95% confidence.

The first test to perform is the determination of whether the slope is within the acceptable confidence interval for the slope found by regression analysis. The confidence interval

on the slope can be calculated as such:

$$CI_m = m \pm t_{(\alpha,n-2)}\hat{\sigma}\sqrt{\frac{1}{\sum_{i=1}^{n}\left(\log\Delta\sigma_i - \overline{\log\Delta\sigma}\right)^2}} \tag{6.14}$$

where t is the two-sided Student t-distribution with significance α and with $n-2$ degrees of freedom, where n is the number of samples, $\log\Delta\sigma_i$ is the logarithm of stress range for individual samples and $\overline{\log\Delta\sigma}$ is the mean of all $\log\Delta\sigma_i$. Using this formula, the 95% confidence interval for slope was found to be between 3.86 and 4.71. Since Categories D and E have slopes of 3.73 and 3.45 respectively, it was found that the slope from the tests could not be assumed with confidence to be the same as in the detail categories.

However, it was decided to continue with the statistical test, by "forcing" the fitted slope to be equal to the Category D standard and finding the best fit given the slope. While this may not be statistically rigorous, it is commonly done in the analysis of fatigue data, for example, the IIW recommends that the slope be taken as $m = 3$ in all welded joints [18]. There is also a certain amount of engineering judgement required, since the slope is rather sensitive to extreme data points. If samples with $N < 50{,}000$ are truncated instead of only the samples with $N < 10{,}000$, the slopes already become much closer and the Category D slope fits within the confidence interval found by Equation 6.14. This is shown in Figure 6.22. The decision to overrule the statistical test of similar slopes was therefore justified. With this achieved, the second component of the test can be formulated as a simple observation that the 95% survival curve is above the standard S-N curve.

Visually, the Category D S-N curve and the 95% survival curve overlap almost perfectly. The value of C used in Equation 6.3 associated with the 95% survival curve is 195.2×10^9, while the value of C used for the Category D curve is 206×10^9, a difference of 5%. This indicates that using the Category D S-N curve would be slightly unconservative and outside the 95% confidence range. It also remains clear that Category E, much lower than Category D, is far below the 95% survival line and thus provides more than adequate safety.

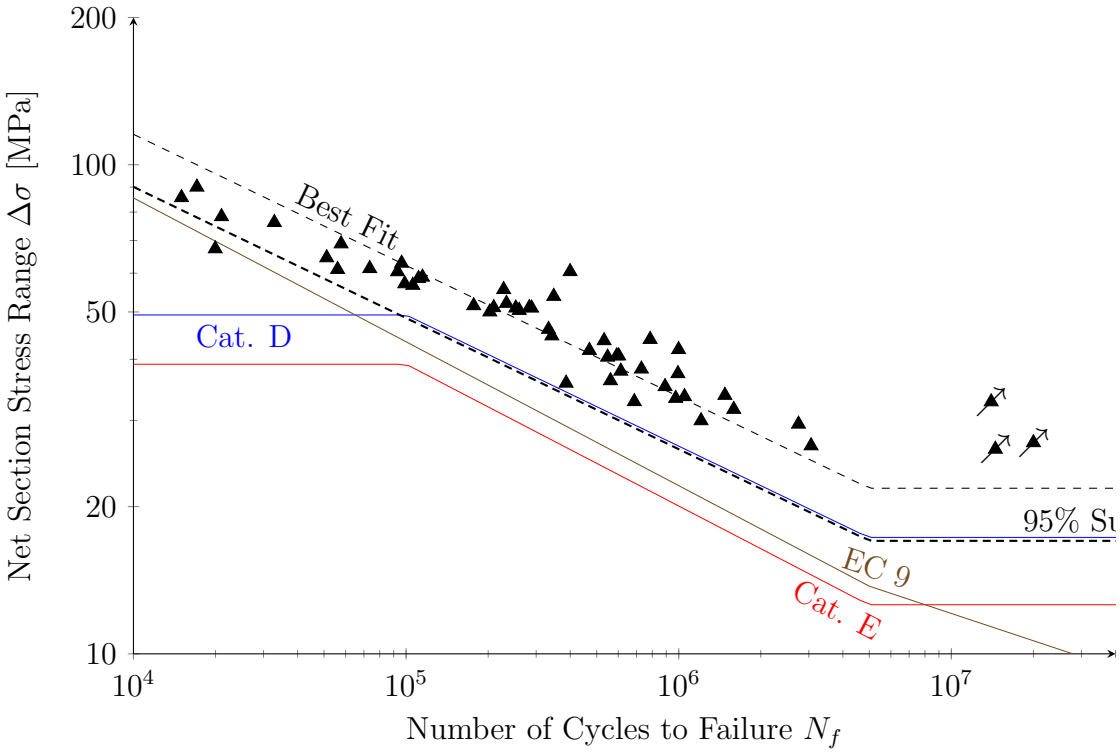

Figure 6.22: Stress-life data for all tested samples, adjusted for $R = 0.5$, but with the best-fit and 95% survival lines based on a "forced" sloped value of 3.73, the same as the Category D S-N curve in the CSA S157 standard.

6.4.4 Comparison of Stress-Life Data with Models

Effect of plate thickness

The LEFM model predicted a significant influence on fatigue life from the plate thickness, as a consequence of the $\sqrt{\pi a}$ term in the SIF equation (Equation 4.3) that varies with the absolute length of the crack. However, the test results did not show such an influence, as shown in Figure 6.23.

The disagreement in trends is rather perplexing. Doubling the thickness approximately halves the fatigue life of the samples, but no such trend is clear from the data. The predictions using a thickness of 9.5 mm seem to correspond much better with all data

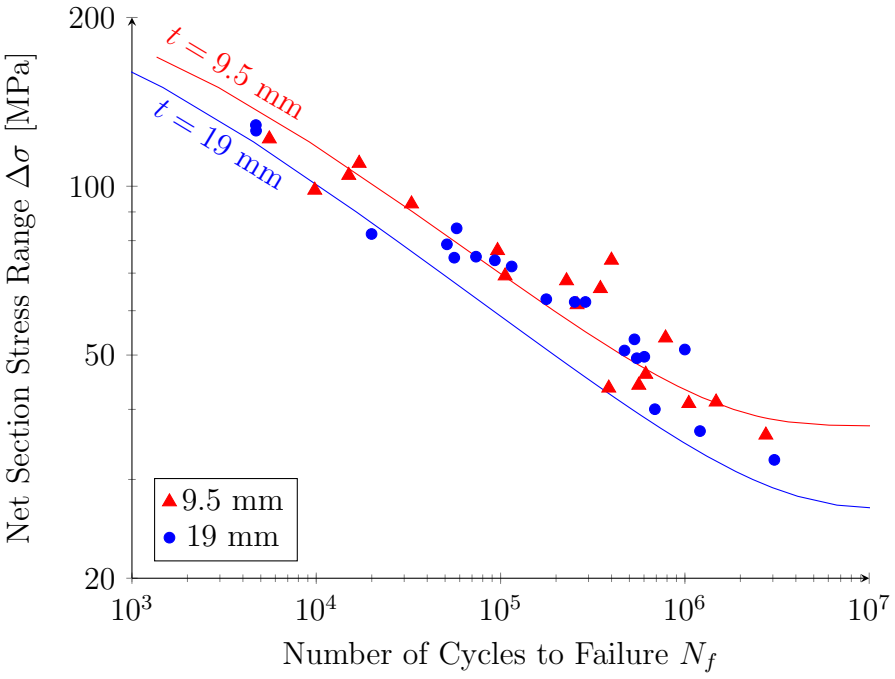

Figure 6.23: Stress-life data for all tested samples with $R = 0.1$, separated by thickness. The lines indicate the results from the LEFM model.

points. It is not clear what explains this discrepancy. The influence of triaxiality, residual stresses, weld geometry, under-penetration and its effect on the crack tip geometry, and other defects, may all have a part to play in the explanation. Further tests on a larger range of thickness would be required to evaluate whether the thickness effect was lost in the scatter of the data or if such an effect truly is mitigated.

Effect of the degree of penetration

As discussed in Section 4.6, it was theorized that the degree of penetration would have relatively little influence on the fatigue performance when the stress range is defined over the net section. Figure 6.24 shows the S-N curves predicted by the LEFM model, with the test data superimposed and coloured by the degree of penetration. When comparing the test results with the LEFM results, it is clear that there is essentially no influence from

the degree of penetration in the range of samples tested, as was expected. The variations between S-N curves fall well within the scatter of the test data.

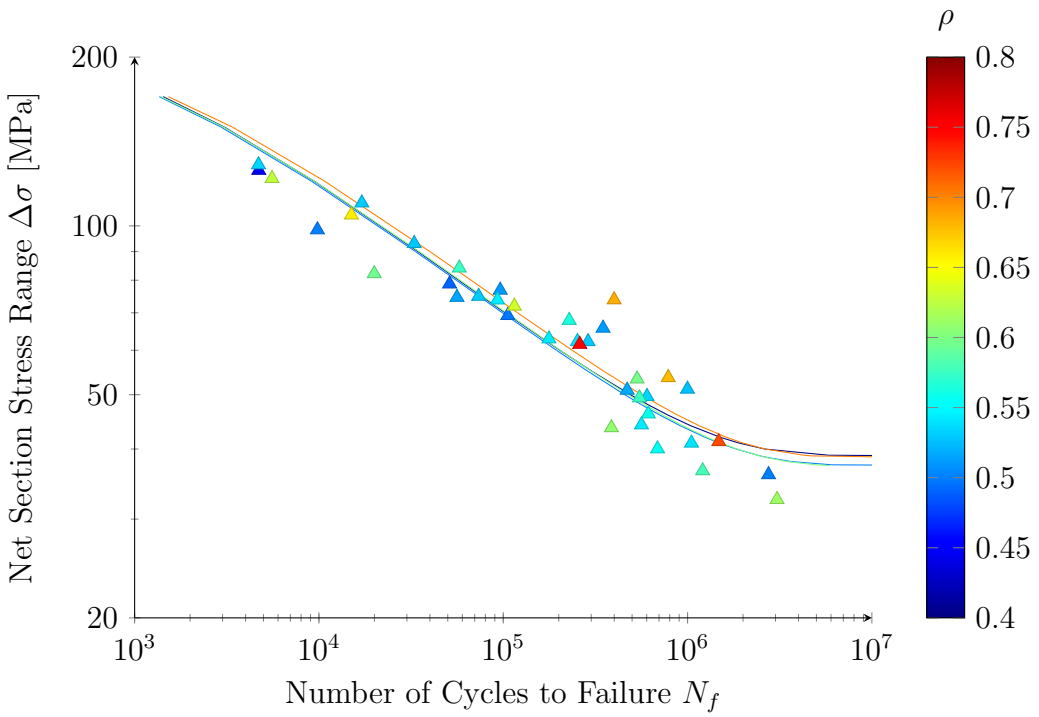

Figure 6.24: Stress-life data for all tested samples with $R = 0.1$, separated by degree of penetration. The lines (coloured using the same scale as the points) indicate the results from the LEFM model, which in this case was run with $t = 9.5\,\text{mm}$ and had a range of ρ between 0.4 and 0.7.

Effect of angular misalignment

The effect of angular misalignment were studied because it was expected that it would provoke asymmetric crack growth and accelerate failure. The asymmetry was considered by comparing results at various misalignment angles φ for a 9.5 mm thick sample with $\rho = 50\%$. It was clearly observed that, as predicted, angular misalignment severely affected fatigue performance by precipitating crack growth to one side of the joint. In Figure 6.25, it can be seen that the crack slowly skews more and more to one side, until a critical point

is reached after which essentially all crack growth occurs on the side nearest to the plate surface. It was observed that by the final cycle, the crack tip on the side near the surface was growing more than 100 times faster than the other side.

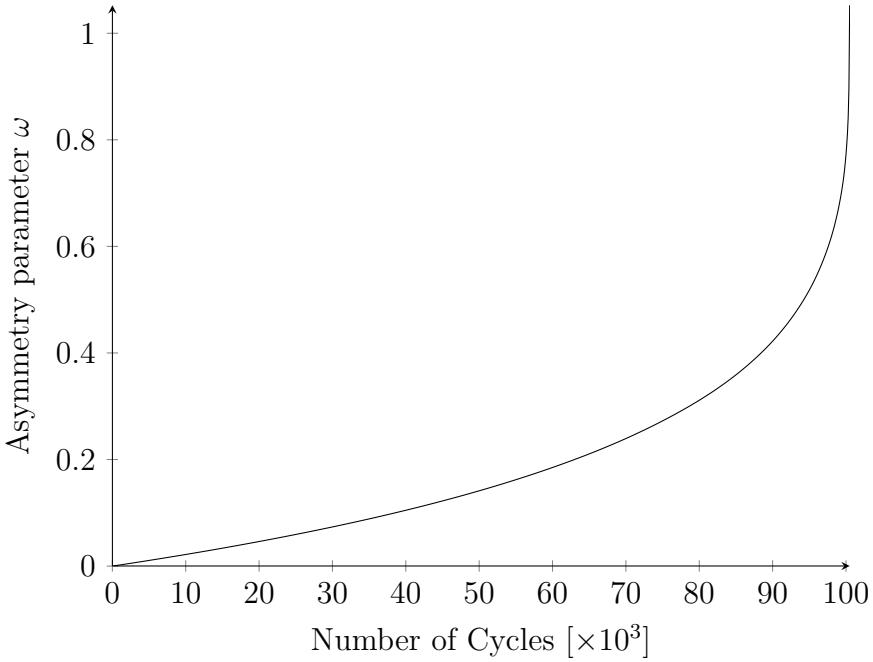

Figure 6.25: Evolution of the crack asymmetry in a sample with angular misalignment. In this case, $\varphi = 1°$, $\Delta\sigma = 60\,\text{MPa}$ and $t = 9.5\,\text{mm}$.

When considering the effects on fatigue life, the stress range at 500,000 cycles was directly compared for the different values of angular misalignment. This value was chosen as opposed to the 2,000,000 cycles used for comparison in other cases, because the model directly accounted for the threshold SIF range and values near that range were already somewhat in the "knee", and linearity was no longer reliable. From this, it can be observed that there is essentially a linear relationship between the angular misalignment and the fatigue performance. While the reduction in performance is relatively severe, it is also not catastrophic. At $\varphi = 1°$, the 400 mm long samples would already have been outside the weld acceptance criteria of most welding standards, with a performance reduction of only 20%. It should also be noted that the assumptions made in the model were very

conservative.

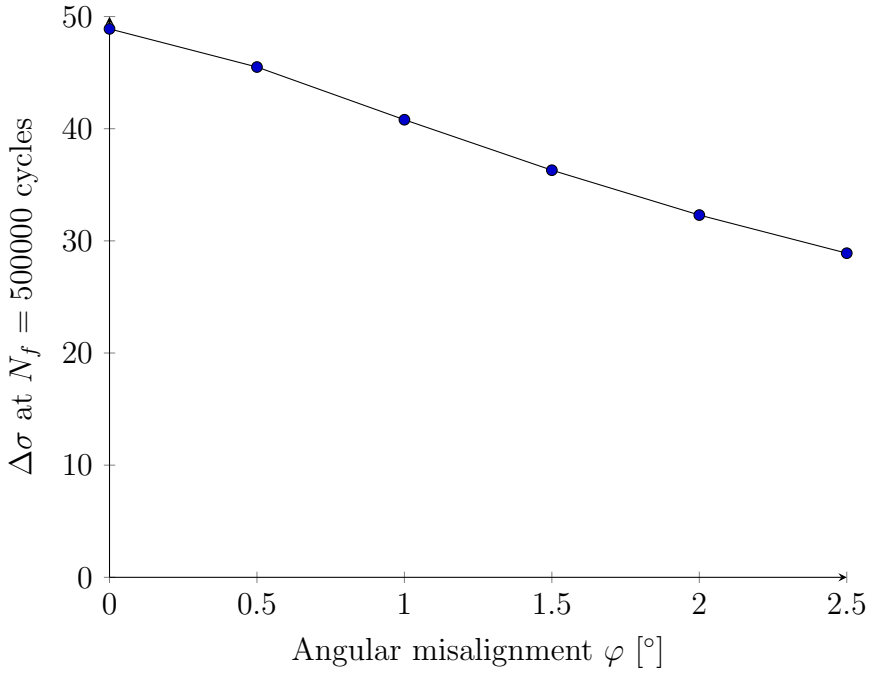

Figure 6.26: Fatigue performance as a function of the angular asymmetry. The sample had $t = 9.5\,\text{mm}$ and the stress range was applied at $R = 0.1$.

There was an initial attempt to correct the experimental data for the effects of misalignment using the techniques for consideration of the asymmetry. However, once the samples were inserted in the testing frame, they were effectively flattened by the grip mechanism. Therefore, the bending stress did not increase the stress range but rather the mean stress, which had little effect on fatigue performance when compared to increasing the alternating stress.

6.4.5 Influence of Weld Roughness on Fatigue Performance

The effect of the welds' roughness was also compared to their fatigue performance. The relative difference between individual sample results and the performance predicted by the

S-N curve based on all results was found as such:

$$\text{Relative Difference} = \frac{\Delta\sigma_{\text{Test}} - \Delta\sigma_{\text{Predicted}}}{\Delta\sigma_{\text{Predicted}}} \tag{6.15}$$

Where $\Delta\sigma_{\text{Predicted}}$ was calculated using mean S-N curves (Figure 6.18, Figure 6.19) for the number of cycles observed in the respective test results. This was then compared with the coefficient of variation (Equation 6.1), as shown in Figure 6.27.

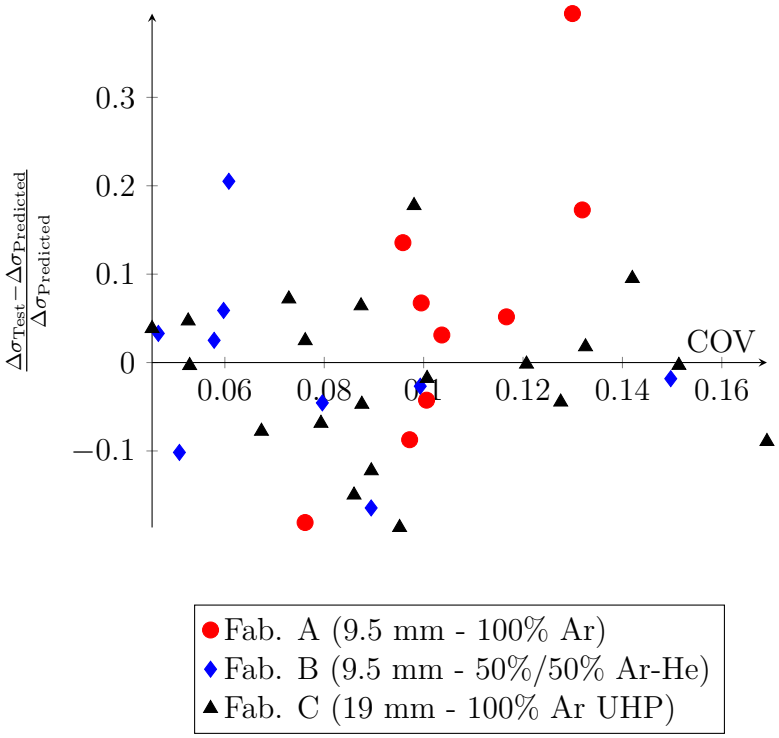

Figure 6.27: The relative fatigue performance of welds compared to their roughness.

It is clear that essentially no correlation exists between the fatigue performance and the COV. It was theorized that there was a shortcoming with using the COV as a definition of roughness. No account is taken of the "wavelength" of the roughness, which means that two samples with vastly different profiles may still have the same COV, as shown in Figure 6.28. It was theorized that the wavelength component of the roughness would have

an effect on the fatigue life of the sample. Small discontinuities (small wavelength) would have a small impact on fatigue life due to neighbouring metal providing reinforcement, while large discontinuities where the sample has a reduced effective throat may not benefit from reinforcement.

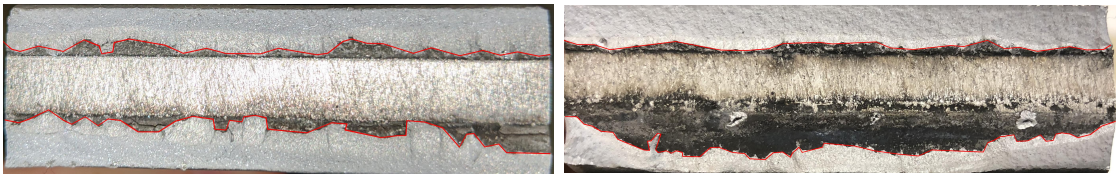

Figure 6.28: The two samples (left: 2060C10, right: 2070C15) both have a COV of ~ 0.17, but have very different shapes at the root, where the right sample roughness is dominated by a relatively smooth large curve at the bottom while the other sample has a more constant effective throat but more peaks/valleys.

More advanced methods were tried to define the roughness, such as using a low-pass filter to only consider large wavelengths or directly comparing the wavelength spectra of samples using the Fourier transform (Figure 6.29). In all cases however, no significant correlation could be found between the weld roughness and the fatigue performance. It is suspected that because the lack of penetration is such a significant crack-like defect, essentially all crack growth is driven by it, and any effects from roughness are negligible. This suggests that simply considering the net weld area is enough to account for the roughness in fatigue.

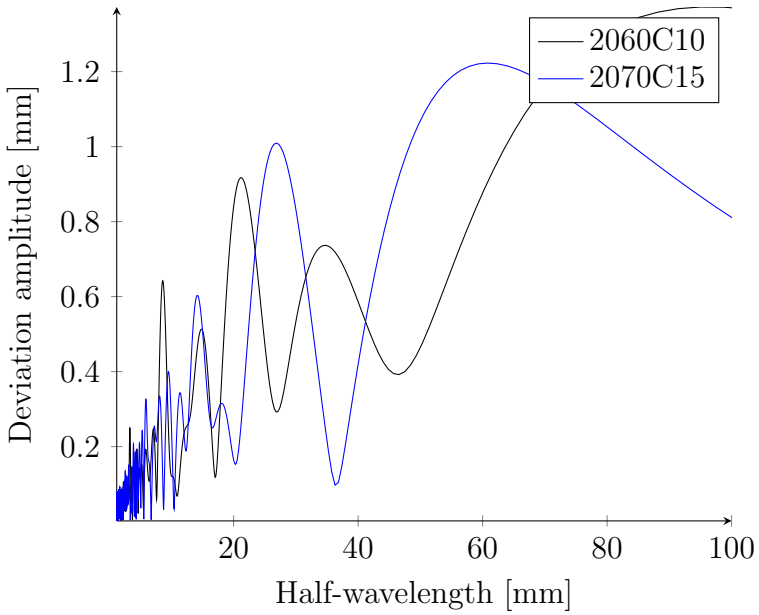

Figure 6.29: Fourier transform of the weld root profiles of the 2060C10 and 2070C15 samples. It is difficult to establish a pattern between the roughness and the profiles. The half-wavelength was used as it more intuitively considers only one side of concavity on a typical sine wave.

Chapter 7

Flare-Bevel PJP Welds

A comprehensive study on the strength and fatigue performance of flare bevel PJP welds (FB welds) was also undertaken as part of this project, but was ultimately delayed due to the measures taken in response to the global COVID-19 pandemic. Flare bevel welds, as briefly described in the literature review, are welds joining a curved surface, such as a rod or the rounded corner of a tube, to a flat surface. This chapter consists of a short summary of the work performed in this subject area at the time of the thesis writing. A typical cross-section of a flare-bevel weld, along with its defining parameters is shown in Figure 7.1.

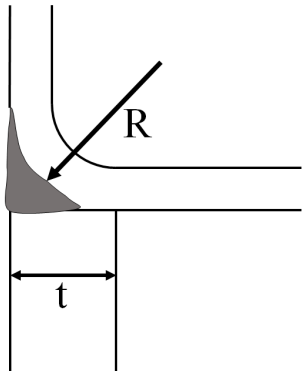

Figure 7.1: Cross-section of a flare-bevel weld joining two tubes with rounded corners. R is the tube's corner radius and t is the wall thickness of the connecting tube.

7.1 Effective Throat of Flare Bevel Welds

Similarly to butt-welded joints with partial penetration, the effective throat of the weld is a critical variable in the performance of flare bevel welds. This value is, however, much harder to define because in most cases, the weld filler metal does not penetrate completely in the radius – leaving a gap and a reduced effective throat, as shown in Figure 7.2.

The AISC 360-16 code, the governing design code for steel in the United States, specifies that the effective throat should be taken as either $\frac{5}{16}$ or $\frac{5}{8}$ of the radius, depending on the welding process. This is based on research by Packer and Frater [50] who studied various configurations of HSS connections. There is essentially no reference for the value of the design throat to use in aluminum members, with structural codes usually resorting to requiring assessment by testing.

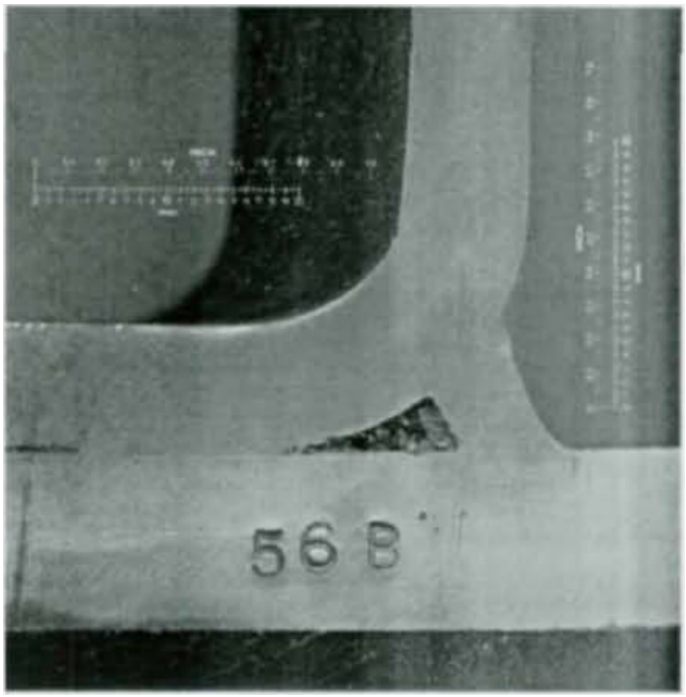

Figure 7.2: A cross-section of a flare bevel weld showing incomplete penetration at the root. *Image from [50].*

7.2 Experimental Program

Samples of FB welds were fabricated to be tested in static and fatigue loading. These were all of the same general geometry, consisting of a T-type tubular connection, as shown in Figure 7.3. These are often seen in aluminum trusses.

In total, 32 samples were fabricated, with the main varying parameter being the corner radius. Four different corner radii were tested. Wall thicknesses and tube dimensions varied according to the availability of tubes with the desired corner radii. One set of samples had a corner radius hand ground (HG). In all but one set of samples, the wall thickness was selected to be larger than the corner radius ($t > R$). The samples which had $t < R$ were the R11.1 batch, due to an error in fabrication. As shown in Figure 7.1, the gap left by the corner radius was filled by weld metal and ground to be flush with the tube walls. All samples were made of 6061-T6 alloy base metal, and welded with the 5356 alloy. The

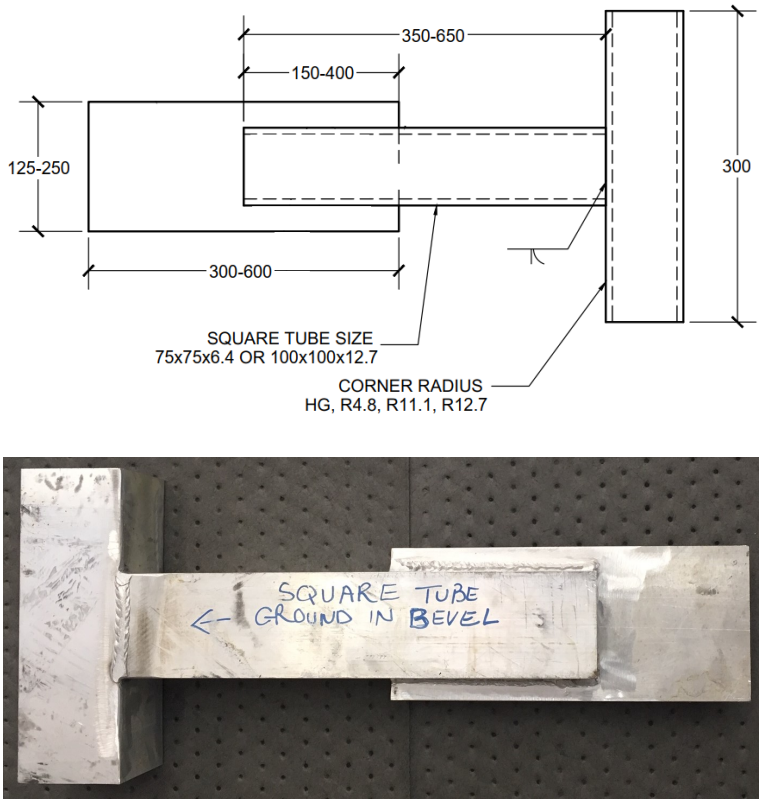

Figure 7.3: Drawing for the tubular samples (top) and typical tested sample (bottom) as part of the flare-bevel weld experimental program. All dimensions are in millimetres.

sample types are summarized in Table 7.1.

Two samples of each type were tested in static loading for strength and ductility, with the remainder intended for fatigue testing and macro-etching. The tests were performed in a MTS servo-hydraulic loading frame with a capacity of 600 kN. A special steel attachment was designed and fabricated to attach the tubular connection to the grips of the loading frame, shown in Figure 7.4. The attachment, consisting of a 64 mm square bar going through the loaded tube and connected to a 102 mm square bar on the outside, was much stiffer than the aluminum tubes, allowing an essentially uniform loading over the square tube.

Table 7.1: Fabricated tubular samples

Sample type	Number of Samples	Corner radius R (mm)	Wall thickness t
HG	8	HG	12.7
R4.8	8	4.8	6.4
R11.1	8	11.1	6.4
R12.7	8	12.7	12.7

Similarly to the method described in Section 3.3.1, DIC measurements were taken to analyze the strain field as the samples were loaded.

7.2.1 Determining the Effective Throat of Flare Bevel Welds

Using a similar method to the one described in Section 3.5, image processing was employed to determine the true size of the welds. This consisted of measuring the total area of weld material in a scaled image. The weld area measured in this way is more susceptible to being changed by plastic deformations, but it was deemed the most accurate method. A typical image-processed result is shown in Figure 7.5.

Figure 7.4: A tubular sample ready to be loaded in the MTS 600 kN frame, attached by the stiff steel connector to the grips.

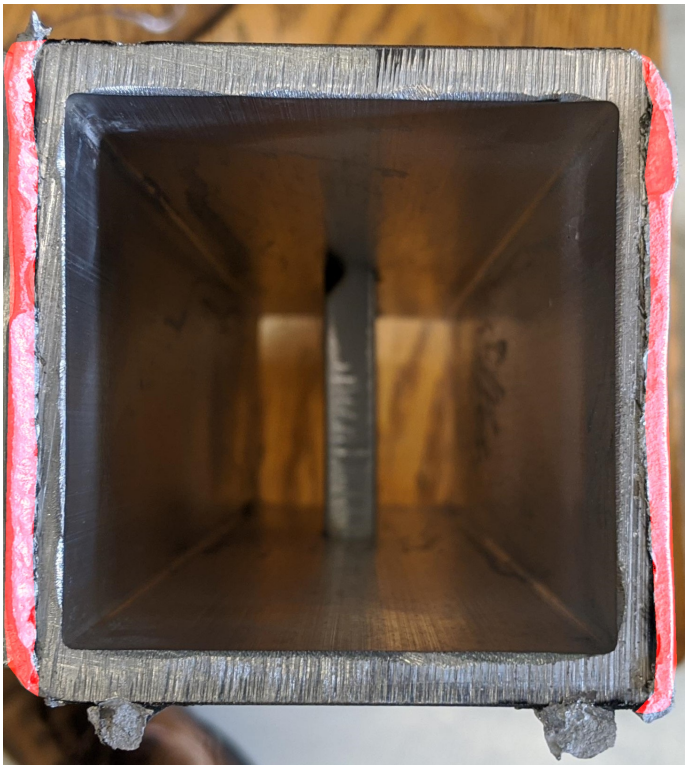

Figure 7.5: A failed tubular sample with the weld area highlighted in red, which was measured to find the true weld size. The two tack-welds at the bottom were not considered in the area calculation.

7.3 Experiment Results

7.3.1 Effective Throat

As described previously, image processing was used to determine the effective throat of the welds. The total weld area was calculated, and divided by the weld length to find the average weld throat on the failure surface. The effective throat per sample is summarized in Table 7.2 and shown graphically in Figure 7.6. Note that because of plastic deformation and inherent errors in the image processing method, there is a somewhat large variation and the results can only be deemed approximate.

Table 7.2: Measured effective throat in tubular samples

Sample ID	Effective Throat E (mm)	E/R
HG-01	3.20	N/A
HG-02	3.03	N/A
R4.8-01	3.79	0.79
R4.8-02	3.55	0.74
R11.1-01	4.47	0.40
R11.1-02	4.35	0.39
R12.7-01	6.39	0.50
R12.7-02	5.99	0.47

Because the hand-ground samples did not have a constant corner radius, it was futile to calculate the ratio of effective throat to corner radius on these samples. For the R11.1 samples, because the wall thickness was less than the corner radius, some "leakage" of the weld prevented the throat to be fully developed over the radius. A relationship can nevertheless be seen whereby the ratio E/R decreases as the corner radius increases. It is suspected that this occurs because, in the smaller radius (R4.8) samples, the heat of welding is distributed over a smaller area, thus allowing deeper fusion and penetration. In the large radius (R12.7) samples, the area exposed to weld is much larger and deeper penetration is harder to achieve. It is suspected that this size effect may only apply at smaller radii and that the effect tapers off at larger radii, which was also observed in the study by Packer and Frater [50]. This is however difficult to show with only two effective

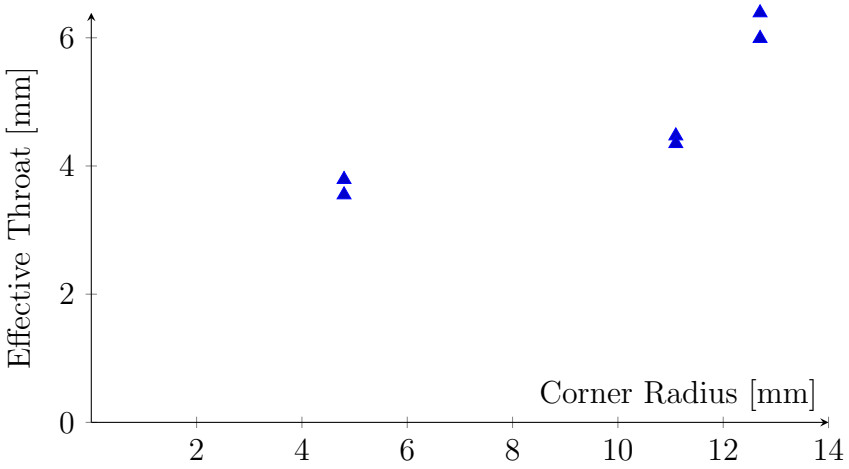

Figure 7.6: The measured effective throat of the tubular samples at the specified corner radii.

radii to serve as data points. Overall, these results suggest that the assumption used for steel of $E = 0.64R$ is unconservative in aluminum, with the R12.7 samples having effective throats much below this ratio.

7.3.2 Strength and Ductility

The strength of the flare bevel welds is probably their most critical property; it was analyzed both in terms of unitary strength per weld length and of the ultimate failure stress. Figure 7.7 shows a typical sample after testing to failure.

Strength per unit of weld length

The final strengths were first calculated by comparing the unit strength of weld. This allowed direct comparison of the strength to the corner radius without consideration for the effective throat of the welds. These results are shown in Figure 7.8,

As the radius of the hand ground samples did not have a constant value, it was not considered in this analysis. Overall, it can be seen that as the corner radius goes up, so

Figure 7.7: A typical failed tubular sample, showing the fracture at the interface of the HAZ and the weld metal. The two tack welds were broken before loading began.

does the failure load. It appears however that the relationship between corner radius and strength is not linear as may be expected (connecting the points between the samples clearly shows that the predicted strength would not go to zero with $R = 0$). This is likely related to the theorized size effect on the effective weld throat discussed previously. It is, however, difficult to determine conclusions on the nature of the relationship between strength and corner radius for two reasons. First, because the R11.1 specimen had a wall thickness t less than the corner radius R, it is doubtful that the fully achievable weld throat was reached, as it was evident from visual observations that the weld filler metal had "leaked" through to the inside of the tube. Second, the small number of data points makes it difficult to infer a trend, especially since the R11.1 samples are of dubious importance, which leaves

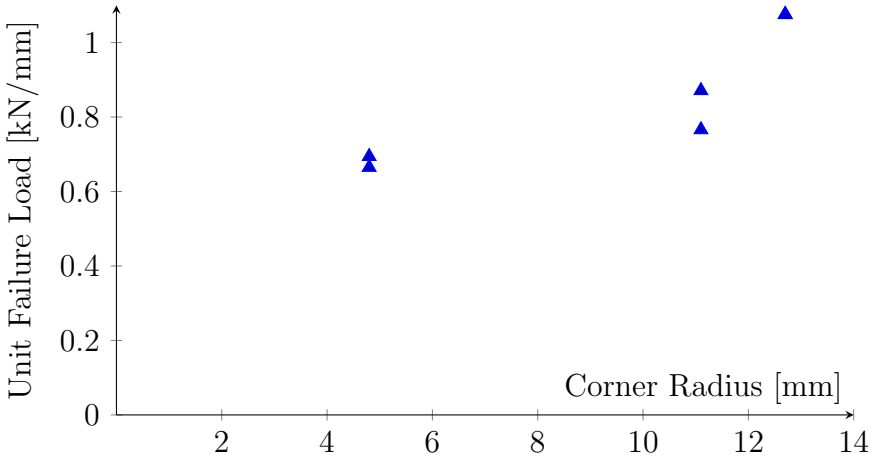

Figure 7.8: The strength per unit length of weld as a function of corner radius. Note that the hand ground (HG) samples were not considered here, and that the two points for the R12.7 samples had exactly the same failure load, thus appearing as only one point on the chart.

a total of only 4 data points at 2 different corner radii.

Ultimate stress

By dividing the linear strength by the effective throat, the failure stress over the welds could be calculated. Since the corner radius was not needed here, this allowed direct comparison of all four sample types, including the hand-ground samples. These results are shown in Table 7.3.

The samples have an average failure stress of 181 MPa with relatively low variance. This is lower than what was observed in the PJP butt welds shown in Figure 6.11, despite the same base and weld filler metal being used in the both types of samples. In fact, analysis of some mill test reports shows that the tubular samples were of stronger base metal than the plates used for the PJP butt welds (Appendix B). It is possible that the weld metal used in the tubular joints was weaker; however, this is unlikely given that three different fabricators provided samples. In fact, one fabricator provided both plate and tubular samples, presumably using the same procedures and filler metal. A likely explanation is

Table 7.3: Ultimate failure stress of tested tubular samples

Sample ID	Failure Stress (MPa)
HG-01	179
HG-02	176
R4.8-01	183
R4.8-02	187
R11.1-01	195
R11.1-02	176
R12.7-01	168
R12.7-02	180

that the high degree of lateral restraint seen in the butt welds (Section 6.3.2) does not develop in the flare bevel welds. The connecting tubes do not have nearly as much stiffness relative to the solid plates used in the butt welded samples. It should be noted that the values here remain comfortably above the S157 and ADM standards' specified heat affected zone strength of 165 MPa.

Digital Image Correlation Results

The DIC results were analyzed and provided two important pieces of information by allowing the creation of a stress-strain curve and by visualizing the strain field during loading. The welds in the samples did not fail on both sides simultaneously – one side failed, and the sample re-adjusted itself, thus allowing the remaining side to be loaded further, though never exceeding the failure load of the first weld. The side which failed first was seemingly random, and, unluckily, only two samples had their failure on the side analyzed for DIC, which somewhat limited the available data. This limited data is however a very insightful look into the behaviour of flare bevel groove welds.

First, a virtual extensometer with a gauge length of 50 mm (Figure 7.10) was used to evaluate the weld ductility, as was done with the plate PJP butt weld samples. The gauge length of 50 mm, which was the gauge length of extensometers in the plate tests, allowed a more or less direct comparison of ductility. A typical resultant stress-strain curve is shown

in Figure 7.9. The stress-strain curve from PJP butt welds (Figure 6.9) was superimposed for comparison.

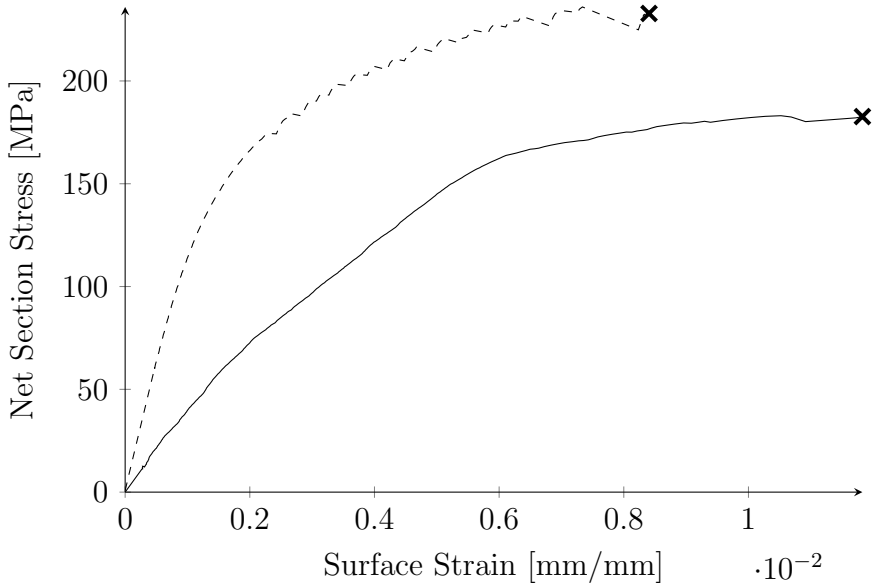

Figure 7.9: Stress-strain curve for the R4.8-01 sample. The stress-strain curve for the 1060A2 plate sample is superimposed in dashed line for comparison.

Compared with the PJP butt welds, there appears to be slightly higher ductility and lower overall strength in the FB welds. Some sources of discrepancies would include that the heat affected zone has a different size than in the plate samples, and that the surface strain on the flare bevel welds, observed by DIC may not be representative of the overall strain in the sample. This may also be explained by the reduced lateral restraint effect in FB welds, theorized to significantly reduce ductility in PJP welds. With reduced lateral restraint in the tubular samples, ductility would be expected to increase at the expense of strength. The Portevin-Le Chatelier (PLC) effect, which appears in the form of a saw tooth pattern in the stress-strain curve after yielding, is not visible in the curve for the plate sample. It is uncertain whether this is a consequence of inaccuracies in the DIC measurements or because of a separate phenomenon.

The DIC results were also used to qualitatively observe the behaviour of the flare bevel welds, as shown in Figure 7.10. From the strain analysis, it is clear that yielding occurs

at the interface between the weld filler and the HAZ. No yielding is apparent at any other location, explaining the low ductility of the joints.

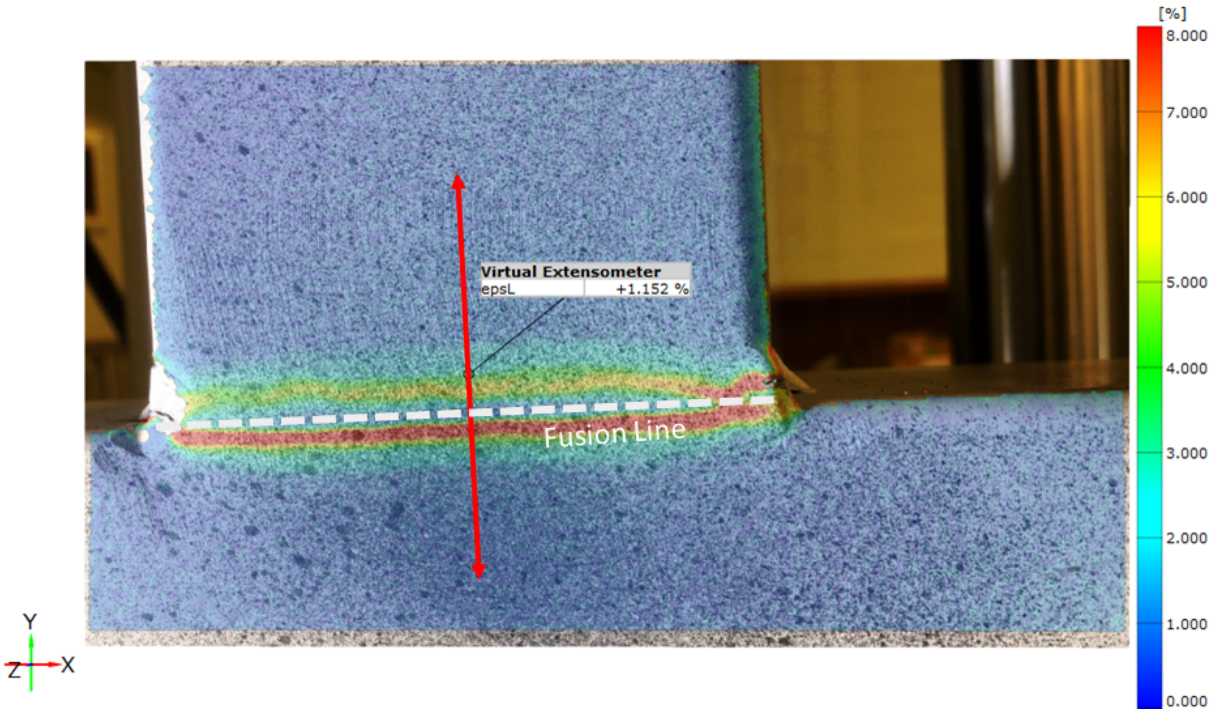

Figure 7.10: Results of the DIC analysis showing the von Mises equivalent strain just before failure. The analysis was performed using the GOM Correlate software. The red arrow indicates the location of the virtual extensometer.

Chapter 8

Conclusions and Future Work

A research project on the performance of aluminum partial joint penetration (PJP) groove welds was undertaken. The project was conceived in response to restrictions and a lack of guidance on their use in Canadian aluminum structures. First, properties of aluminum PJP butt welds such as effective weld throat and the extent of the heat affected zone were examined. The strength of these welds was studied through a comprehensive testing program making use of advanced measurement technologies and accurate finite element models. The samples had different degrees of penetration and plate thicknesses and were made with products from three different fabricators. The weld performance in fatigue was examined by performing 56 fatigue life tests and developing a linear-elastic fracture mechanics model, which, aided by the use of finite element analysis, accounted for asymmetrical crack growth from the weld root. Finally, an extension of this research program was introduced: applying the models and testing methods to flare bevel welds, a different kind of partial penetration weld. Overall, the results indicate that although some concerns arise with their use, PJP welds can provide strong and reliable connections in aluminum structures. Specific findings are discussed in the following sections of this chapter. Although Canada is a leading producer of aluminum in the world, it remains mostly an exporter of raw aluminum. Reducing barriers to design, like confusing or inadequate rules, would be a large step in increasing the acceptance of aluminum by structural engineers in

Canada.

8.1 Conclusions

The findings reached as an outcome of this research program may be separated into four principal categories, as detailed in the following sections.

8.1.1 Properties of PJP Welds

- The effective throats in samples with the highest specified degrees of penetration were far below the specified value. This suggests that code limits for groove angle may not be adequate to ensure proper penetration. A major safety concern occurs here on the reliability of the welds. Until more information is found on the effective throat of PJP welds, rigorous ultrasonic testing of the welds may provide confidence that the adequate effective throat has been reached.

- Although the heat input associated with PJP welds is lower than traditional welds, the heat affected zone in the base metal spans the entire thickness of the plate and thus the full HAZ effects must be considered through the thickness.

- Overall, the weld quality varied relatively little by fabricator, regardless of the shielding gas employed or the specific source of materials. The performance of these welds is relatively insensitive to the procedure used or the individual welder.

8.1.2 Strength of PJP Welds

- The strength of PJP butt welds is entirely determined by the strength of the heat affected zone. This does not vary according to the groove preparation and with typical structural alloys, does not depend on the weld filler metal strength.

- The unwelded area between welds provides significant lateral restraint, which increases the effective strength of the welds. This was confirmed using advanced measurement techniques on laboratory samples and using finite element analysis.
- PJP welds exhibit extremely low ductility when compared to other aluminum weld types, which renders them unattractive for primary load carrying members.

8.1.3 Fatigue Performance of PJP Welds

- The degree of penetration has relatively little influence over the fatigue performance of PJP welds when the applied stress is defined over the net weld cross-section, which confirms that a typical S-N curve design approach is appropriate for these welds.
- According to a statistical analysis, the Category D S-N curve in CSA S157 and the Aluminum Design Manual could serve as an adequate design curve for PJP welds. However, for increased safety, it may be advisable to use Category E in more critical applications. Such an approach would also coincide with the Eurocode 9 detail category for PJP welds.
- The magnitude of residual stresses in the welds is somewhat unknown. The tests indicate that only minimal residual stresses are present in the welds; however, this may be because only small scale samples were used.
- Accidental eccentricities from warping during welding and unequal crack length were found to have a detrimental effect on the fatigue life as the crack growth is precipitated to one side.
- The weld roughness at the root did not seem to have a significant effect on fatigue performance, probably because the lack of penetration creates a far larger global effect on stress concentration than does localized roughness.

8.1.4 Flare Bevel Welds

- It is unconservative to simply assume the effective throat of flare bevel welds as equal to the corner radius. Assuming an effective throat of 5/16 of the corner radius, as is sometimes done in steel structures, would appear to be conservative.
- Compared to PJP butt welds, the strength of flare bevel welds is expected to be slightly lower per unit weld area, but with greater ductility. This is likely due to reduced lateral restraint in the weld.

8.2 Future Work

Many areas requiring further investigation were identified over the course of this research project. The subjects deemed most important are as follows:

- Expansion of both static and fatigue tests to a wider range of degrees of penetration. This would allow the confirmation of the adequacy of models on lateral restraint and on the relative sensitivity of fatigue life to the degree of penetration.
- Investigation into the required groove angle and appropriate welding parameters to consistently ensure adequate welds.
- Performance of additional fatigue tests on a larger variety of thicknesses. The contradiction between the fracture-mechanics-based model and the test results, where the model predicted a high sensitivity to plate thickness that was not seen in the tests results, is perplexing The presence and magnitude of residual stresses and their effects also require further investigation.
- Expansion of the testing program to different aluminum alloys. Given the large variety of alloys used in practice, it would be sensible to obtain more certainty about the independence of alloy selection vis-à-vis the phenomena and mechanisms presented in this thesis.

References

[1] J. M. Runge, *A Brief History of Aluminum and Its Alloys*. 2018.

[2] R. Gitter, "Aluminium Materials for Structural Engineering – Essential Properties and Selection of Materials," 2006.

[3] The Aluminum Association, "The Environmental Footprint of Semi- Finished Aluminum Products in North America," Tech. Rep. December, 2013.

[4] S. K. Das and J. G. Kaufman, "Aluminum Alloys for Bridges and Bridge Decks," pp. 61–72, 2007.

[5] Deloitte, "Life Cycle Analysis Aluminium vs. Steel," tech. rep., 2012.

[6] V. Malin, "Study of metallurgical phenomena in the HAZ of 6061-T6 aluminum welded joints," *Welding Journal (Miami, Fla)*, vol. 74, no. 9, 1995.

[7] B. T. Gibson, D. H. Lammlein, T. J. Prater, W. R. Longhurst, C. D. Cox, M. C. Ballun, K. J. Dharmaraj, G. E. Cook, and A. M. Strauss, "Friction stir welding: Process, automation, and control," *Journal of Manufacturing Processes*, vol. 16, no. 1, pp. 56–73, 2014.

[8] Florida Department of Transportation, "Aluminum lightweight orthotropic deck evaluation project," tech. rep., 2017.

[9] CSA, *Strength design in aluminum / Commentary on CSA S157-17 , Strength design in aluminum*. 2018.

[10] The Aluminum Association, *Aluminum Design Manual*. 2015.

[11] European Committee for Standardization, *Eurocode 9: Design of aluminium structures - Part 1-1: General structural rules*. 2007.

[12] Q. Y. Wang, N. Kawagoishi, and Q. Chen, "Fatigue and fracture behaviour of structural Al-alloys up to very long life regimes," *International Journal of Fatigue*, vol. 28, no. 11, pp. 1572–1576, 2006.

[13] Y. Takahashi, H. Yoshitake, R. Nakamichi, T. Wada, M. Takuma, T. Shikama, and H. Noguchi, "Fatigue limit investigation of 6061-T6 aluminum alloy in giga-cycle regime," *Materials Science and Engineering A*, vol. 614, pp. 243–249, 2014.

[14] J. W. Fisher, G. L. Kulak, and I. F. C. Smith, "A Fatigue Primer for Structural Engineers," tech. rep., National Steel Bridge Alliance, 1998.

[15] K. Ghahremani and S. Walbridge, "Fatigue testing and analysis of peened highway bridge welds under in-service variable amplitude loading conditions," *International Journal of Fatigue*, vol. 33, no. 3, pp. 300–312, 2011.

[16] C. C. Menzemer and J. W. Fisher, "Fatigue design of welded aluminum structures," *Transportation Research Record*, no. 1393, pp. 79–88, 1993.

[17] R. Ranjan, A. C. de Oliveira Miranda, S. Hui Guo, S. Walbridge, and A. Gerlich, "Fatigue analysis of friction stir welded butt joints under bending and tension load," *Engineering Fracture Mechanics*, vol. 206, pp. 34–45, 2 2019.

[18] A. F. Hobbacher, *Recommendations for Fatigue Design of Welded Joints and Components*. International Institute of Welding, 2014.

[19] T. L. Anderson, *Fracture Mechanics: Fundamentals and Applications, Fourth Edition*. 2017.

[20] P. Paris and F. Erdogan, "A critical analysis of crack propagation laws," *Journal of Fluids Engineering, Transactions of the ASME*, vol. 85, no. 4, pp. 528–533, 1963.

[21] E. M. Honig and K. W. Carlson, "Tensile Properties of A514 Steel Butt Joints Containing Cluster Porosity.," *Welding Journal (Miami, Fla)*, vol. 55, no. 4, pp. 103–107, 1976.

[22] F. V. Lawrence and E. P. Cox, "Influence of Inadequate Joint Penetration on Tensile Behavior of A514 Steel Welds," *Welding Journal (Miami, Fla)*, vol. 55, no. 5, pp. 113–120, 1976.

[23] E. P. Popov and R. M. Stephen, "Tensile Capacity of Partial Penetration Groove Welds," *ASCE J Struct Div*, vol. 103, no. 9, pp. 1721–1729, 1977.

[24] D. P. Gagnon and D. J. Kennedy, "Behaviour and ultimate tensile strength of partial joint penetration groove welds," *Canadian Journal of Civil Engineering*, vol. 16, no. 3, pp. 384–399, 1989.

[25] M. Reynolds, Q. Huynh, B. Rafezy, and C. M. Uang, "Strength of Partial-Joint-Penetration Groove Welds as Affected by Root Opening, Reinforcing, and Loading Direction," *Journal of Structural Engineering (United States)*, vol. 146, no. 8, pp. 1–11, 2020.

[26] F. V. Lawrence and W. H. Munse, "Fatigue Crack Propagation in Butt Welds Containing Joint Penetration Defects," *Welding Journal (Miami, Fla)*, vol. 52, no. 5, pp. 221–225, 1973.

[27] S. Kim, K. Jin, W. Sung, and S. Nam, "Effect of Lack of Penetration on the fatigue strength of high strength steel butt weld," *KSME Journal*, vol. 8, no. 2, pp. 191–197, 1994.

[28] N. Hiroshi, M. Eto, K. Tachibana, and M. Nakahira, "Fatigue strength reduction factor of partial penetration weldments for ITER vacuum vessel," in *SMiRT 16: Selected and Updated Papers from the 16th International Conference on Structural Mechanics in Reactor Technology, Washington, DC*, no. August, 2001.

[29] W. M. Wilson, W. H. Munse, and I. S. Snyder, "Fatigue Strength of Various Types of Butt Welds Connecting Steel Plates," tech. rep., 1950.

[30] J. Burk and F. V. Lawrence, "Effects of Lack-of-Penetration and Lack-of-Fusion on the Fatigue Properties of 5083 Aluminum Alloy Welds," tech. rep., University of Illinois at Urbana-Champaign, 1976.

[31] U. Brandt, F. V. Lawrence, and C. M. Sonsino, "Fatigue crack initiation and growth in AlMg4.5Mn butt weldments," *Fatigue and Fracture of Engineering Materials and Structures*, vol. 24, no. 2, pp. 117–126, 2001.

[32] C. M. Sonsino, D. Radaj, U. Brandt, and H. P. Lehrke, "Fatigue assessment of welded joints in AlMg 4.5Mn aluminum alloy (AA 5083) by local approaches," *International Journal of Fatigue*, vol. 21, no. 9, pp. 985–999, 1999.

[33] European Committee for Standardization, *Eurocode 9: Design of aluminium structures - Part 1-3: Structures susceptible to fatigue*. 2007.

[34] ASTM International, *ASTM E3-11, Standard Guide for Preparation of Metallographic Specimens*. 2017.

[35] ASTM International, *ASTM E340-15, Standard Practice for Macroetching Metals and Alloys*. 2015.

[36] ASTM International, *ASTM E384-17 Standard Test Method for Microindentation Hardness of Materials*. 2017.

[37] ASTM International, *ASTM E647-15 - Standard Test Method for Measurement of Fatigue Crack Growth Rates*, vol. 03. 2016.

[38] S. J. Maddox, "Review of fatigue assessment procedures for welded aluminium structures," *International Journal of Fatigue*, 2003.

[39] R. Ranjan, K. Ghahremani, S. Walbridge, and A. Ince, "Testing and fracture mechanics analysis of strength effects on the fatigue behavior of HFMI-treated welds," *Welding in the World*, vol. 60, no. 5, pp. 987–999, 2016.

[40] A. C. d. O. Miranda, A. Gerlich, and S. Walbridge, "Aluminum friction stir welds: Review of fatigue parameter data and probabilistic fracture mechanics analysis," *Engineering Fracture Mechanics*, 2015.

[41] R. Jaccard, "Fatigue crack propagation in aluminium," *IIW Doc XIII*, pp. 1377–1390, 1990.

[42] J. C. Newman, "A crack opening stress equation for fatigue crack growth," *International Journal of Fracture*, vol. 24, no. 4, pp. 131–135, 1984.

[43] R. C. McClung, "Finite Element Analysis of Specimen Geometry Effects on Fatigue Crack Closure," *Fatigue & Fracture of Engineering Materials & Structures*, vol. 17, no. 8, pp. 861–872, 1994.

[44] R. Coughlin and S. Walbridge, "Fatigue testing and analysis of aluminum welds under in-service highway bridge loading conditions," *Journal of Bridge Engineering*, vol. 17, no. 3, pp. 409–419, 2012.

[45] M. Sharp, "Static and Dynamic Behavior of Welded Aluminum Beams," pp. 49–56, 1973.

[46] J. Rice, "A Path Independent Integral and the Approximate Analysis of Strain Concentration by Notches and Cracks," *Journal of Applied Mechanics*, vol. 35, no. 2, p. 379, 1968.

[47] A. H. Baghdadi, A. Rajabi, N. F. M. Selamat, Z. Sajuri, and M. Z. Omar, "Effect of post-weld heat treatment on the mechanical behavior and dislocation density of friction stir welded Al6061," *Materials Science and Engineering A*, vol. 754, no. March, pp. 728–734, 2019.

[48] N. E. Dowling, C. A. Calhoun, and A. Arcari, "Mean stress effects in stress-life fatigue and the Walker equation," *Fatigue and Fracture of Engineering Materials and Structures*, vol. 32, no. 3, pp. 163–179, 2009.

[49] C. R. A. Schneider and S. J. Maddox, "Best Practice Guide on Statistical Analysis of Fatigue Data. IIW, XIII-WG1-114-03," Tech. Rep. February, International Institute of Welding, 2003.

[50] J. A. Packer and G. S. Frater, "Recommended Effective Throat Sizes for Flare Groove Welds to HSS," tech. rep., American Institute for Steel Construction, Chicago, 2005.

Appendices

Appendix A

Tabulated Shape Factor Values for Stress Intensity Factor Calculations

This appendix presents tabulated values used for calculating the stress intensity factor as explained in Section 5.2.3. These values were calculated using finite element analysis and a contour integral approach. As a reminder:

$$\omega = 1 - w_1/w_2, \qquad \rho = \frac{w_1 + w_2}{2t} \tag{A.1}$$

where w_1, w_2 and t are defined in Figure A.1.

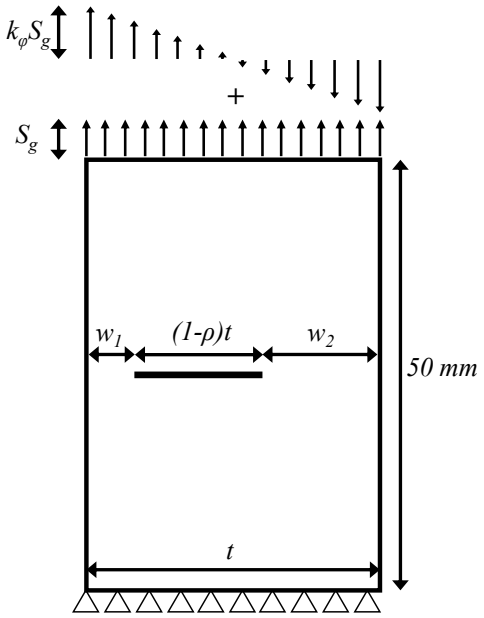

Figure A.1: Dimensions used in calculating the J-integral to find Y.

A.1 Purely Axial Loading with Uncentered Crack

Table A.1: Shape factor Y for crack tip nearer to plate edge (axial)

		ρ								
		0.1	0.2	0.3	0.4	0.5	0.6	0.7	0.8	0.9
ω	0	2.58	1.82	1.49	1.30	1.19	1.11	1.06	1.02	1.01
	0.1	2.64	1.85	1.51	1.32	1.20	1.11	1.06	1.03	1.01
	0.2	2.71	1.90	1.54	1.34	1.21	1.12	1.06	1.03	1.01
	0.3	2.81	1.95	1.58	1.36	1.23	1.13	1.07	1.03	1.01
	0.4	2.93	2.03	1.63	1.40	1.25	1.15	1.08	1.03	1.01
	0.5	3.10	2.13	1.71	1.45	1.29	1.17	1.09	1.04	1.01
	0.6	3.33	2.28	1.81	1.53	1.34	1.21	1.12	1.05	1.01
	0.7	3.70	2.52	1.98	1.66	1.44	1.27	1.15	1.07	1.02
	0.8	4.34	2.94	2.29	1.89	1.60	1.39	1.23	1.11	1.03
	0.9	5.87	3.95	3.03	2.44	2.00	1.67	1.41	1.21	1.06

Table A.2: Shape factor Y for crack tip farther from plate edge (axial)

		ρ								
		0.1	0.2	0.3	0.4	0.5	0.6	0.7	0.8	0.9
ω	0	2.58	1.82	1.49	1.30	1.19	1.11	1.06	1.02	1.01
	0.1	2.52	1.78	1.47	1.29	1.18	1.11	1.06	1.02	1.01
	0.2	2.47	1.75	1.45	1.28	1.17	1.10	1.06	1.02	1.01
	0.3	2.42	1.73	1.43	1.27	1.17	1.10	1.06	1.03	1.01
	0.4	2.36	1.70	1.42	1.27	1.17	1.11	1.06	1.03	1.01
	0.5	2.31	1.68	1.41	1.27	1.18	1.11	1.07	1.03	1.01
	0.6	2.26	1.66	1.41	1.28	1.19	1.13	1.08	1.04	1.01
	0.7	2.22	1.65	1.43	1.30	1.21	1.15	1.10	1.05	1.02
	0.8	2.19	1.67	1.46	1.35	1.26	1.20	1.13	1.07	1.02
	0.9	2.20	1.74	1.57	1.46	1.38	1.29	1.21	1.12	1.05

A.2 Purely Flexural Loading with Uncentered Crack

Table A.3: Shape factor Y for crack tip nearer to plate edge (bending)

		ρ								
		0.1	0.2	0.3	0.4	0.5	0.6	0.7	0.8	0.9
ω	0	0.78	0.52	0.40	0.32	0.26	0.20	0.15	0.10	0.05
	0.1	0.81	0.55	0.43	0.35	0.29	0.24	0.19	0.14	0.10
	0.2	0.85	0.58	0.46	0.38	0.33	0.28	0.23	0.19	0.15
	0.3	0.90	0.62	0.50	0.42	0.37	0.32	0.28	0.25	0.21
	0.4	0.95	0.67	0.55	0.47	0.42	0.38	0.34	0.31	0.28
	0.5	1.03	0.73	0.61	0.53	0.48	0.44	0.41	0.38	0.35
	0.6	1.14	0.82	0.69	0.61	0.56	0.52	0.49	0.46	0.44
	0.7	1.29	0.95	0.80	0.72	0.67	0.62	0.59	0.56	0.54
	0.8	1.56	1.16	0.99	0.90	0.83	0.77	0.73	0.69	0.67
	0.9	2.18	1.64	1.41	1.27	1.15	1.06	0.97	0.89	0.83

Table A.4: Shape factor Y for crack tip farther from plate edge (bending)

		ρ								
		0.1	0.2	0.3	0.4	0.5	0.6	0.7	0.8	0.9
ω	0	-0.78	-0.52	-0.40	-0.32	-0.26	-0.20	-0.15	-0.10	-0.05
	0.1	-0.75	-0.49	-0.37	-0.29	-0.23	-0.17	-0.11	-0.06	0.00
	0.2	-0.72	-0.46	-0.34	-0.26	-0.19	-0.13	-0.07	-0.01	0.05
	0.3	-0.68	-0.43	-0.31	-0.22	-0.15	-0.08	-0.02	0.04	0.11
	0.4	-0.65	-0.40	-0.27	-0.18	-0.11	-0.03	0.04	0.11	0.18
	0.5	-0.61	-0.36	-0.23	-0.14	-0.05	0.02	0.10	0.18	0.25
	0.6	-0.57	-0.32	-0.19	-0.08	0.01	0.09	0.17	0.26	0.34
	0.7	-0.52	-0.27	-0.13	-0.02	0.08	0.17	0.26	0.35	0.44
	0.8	-0.46	-0.21	-0.05	0.07	0.18	0.28	0.38	0.47	0.56
	0.9	-0.39	-0.12	0.06	0.20	0.33	0.44	0.55	0.64	0.72

Negative Y values were employed where bending loads placed the crack tip under compression.

Appendix B

Mill Test Reports

The following are mill test reports from one fabricator which provided both plate and tubular samples. The first is the report for the plates, with the batch from which the samples were taken highlighted in yellow. Second is the test report for the tube samples.

明泰铝业

ZHENGZHOU MINGTAI INDUSTRY CO., LTD

NO.6 CHANGCHUN ROAD, HIGH AND NEW TECHNOLOGY ZONE, ZHENGZHOU HENAN CHINA
TEL: 371-67898611 FAX: 371-67898612

INSPECTION CERTIFICATE

BUYER: RYERSON CANADA INC.
1219 Corporate Drive
Burlington, ON L7L 5V5,Canada

INVOICE NO.: Z-RYWP181201
CONTRACT NUMBER: 4500909902/4500909899
LOADING PORT: QINGDAO, CHINA
DESTINATION: MONTREAL, CANADA
SHIPPING MARKS: N/M
DATE: 12/07/18

DESCRIPTION OF GOODS:
ALUMINIUM SHEETS ALLOY 6061/T651 AND 6061/T6
P.O. NO.: 4500909902/4500909899
DAP MONTREAL, CANADA

ACTUAL MILL CHEMICAL UNIT:%

Alloy No.	Temper	Lot No.	Si	Fe	Cu	Mn	Mg	Cr	Zn	Ti	Others	Al
STANDARD			0.4-0.8	0.7	0.15-0.4	0.15	0.8-1.2	0.04-0.35	0.25	0.15	0.15	REMAIN
6061	T651	ZB-1811Y6052	0.621	0.403	0.235	0.078	1.029	0.188	0.046	0.027	0.15	REMAIN
6061	T651	ZB-1811Y6088	0.601	0.386	0.248	0.064	1.010	0.190	0.058	0.025	0.15	REMAIN
6061	T651	ZB-1811Y6086	0.607	0.431	0.251	0.060	1.005	0.190	0.061	0.026	0.15	REMAIN
6061	T651	GFG1810W60383	0.605	0.441	0.270	0.059	1.028	0.203	0.059	0.027	0.15	REMAIN
STANDARD			0.4-0.8	0.7	0.15-0.4	0.15	0.8-1.2	0.04-0.35	0.25	0.15	0.15	REMAIN
6061	T6	ZB-1811Y6091	0.687	0.371	0.231	0.067	1.010	0.186	0.041	0.025	0.15	REMAIN
6061	T6	ZB-1810Y6091	0.607	0.411	0.236	0.064	1.015	0.198	0.050	0.026	0.15	REMAIN
6061	T6	ZB-1811Y6091	0.587	0.371	0.231	0.067	1.010	0.186	0.041	0.025	0.15	REMAIN

MECHANICAL PROPERTY TEST REPORTS

Alloy No.	Temper	Lot No.	SIZE(MM)	SIZE(IN)	Tensile strength (MPa)	Yield strength (MPa)	Elongation (%)
STANDARD					min290	min242	min 8
6061	T651	ZB-1811Y6052	7.95*1232*3670	.313*48.5*144.5	294	246	19
6061	T651	ZB-1811Y6088	9.525*1232*2451	.375*48.5*96.5	293	273	18
6061	T651	ZB-1811Y6086	12.7*1537*3670	.500*60.5*144.5	291	271	19
6061	T651	GFG1810W60383	19.05*1232*2451	.750*48.5*96.5	300	270	14
STANDARD					min289	min242	min 10
6061	T6	ZB-1811Y6091	4.826*1219*3048	.190*48*120	325	273	18
6061	T6	ZB-1810Y6091	4.826*1219*2438	.190*48*96	314	294	14
6061	T6	ZB-1811Y6091	4.826*1219*2438	.190*48*96	326	273	18

We certify that 6061 T651 material complies with ASTM B209-14,AMS 4027N,AMS-QQA-250/11 standard.
We certify that 6061 T6 material complies with ASTM B209-14,AMS 4027N,AMS-QQA-250/11 standard.

MANUFACTURER: ZHENGZHOU MINGTAI INDUSTRY CO., LTD
POSITION: MANAGER OF OVERSEAS DEPARTMENT
NAME: ZHUOLA WEI

ZHENGZHOU MINGTAI INDUSTRY CO.,LTD.
郑州明泰实业有限公司
魏卓拉

POSITION: QC MANAGER
NAME: LONGFEI SUN

C147580

EXTRUDEX ALUMINUM CORP.

TEL: (416)745-4444 FAX:(416)745-0925 1-800-668-7210
411 CHRISLEA ROAD, WOODBRIDGE, ONTARIO, CANADA L4L 8N4
http://www.extrudex.com

MILL TEST

BILL TO	CERT CODE:	DIE NUMBER		DATE OF SHIPMENT
EXTRUDEX ALUMINUM (QUEBEC) INC.	1	H 13783		Feb/25/2016
SHIP TO S2783	CUSTOMER PO	ALLOY	TEMPER	SALESMAN
		6061	T6	HOUSE ACCOUNTS
SO DESCRIPTION	CUSTOMER PART NUMBER	PART DESCRIPTION		CERTIFICATION
3" X 3" X 0.250" TUBE	H13783	3" X 3" X 0.250" TUBE		MILL TEST ASTM B221-14

EXTRUDEX ORDER NO. 190104 — 4

MANIFEST NO. 344138

MADE IN CANADA

Mechanical Properties

Lot	Alloy	Test Date	Ultimate Tensile Strength (KSI)	Yield Strength (KSI)	Percent Elongation	Hardness Rockwell F	Conductivity
A.11	6061	Feb/16/2016	45.10	42.40	15.20	91.3, 91.7, 90.9	

Chemical Composition

Cast Number	Lot	Alloy	Si	Fe	Cu	Mn	Mg	Cr	Ni	Zn	Ti	Ga	V	B	Zr	Bi	Pb	Sn	Sr	Co	Al	Other
3B1662	A.11	6061	0.6	0.19	0.21	0.04	0.86	0.07	0	0.01	0.01	0	0	0	0	0	0	0	0	0	Remainder	0

We certify that the following extrusions have been quality inspected/tested and conforms to required dimensional and temper specifications.

David Natale
Quality Control Manager

1 - CUSTOMER COPY